ABSTRACT

Title of Document: AGE, COMPOSITION, AND ORIGIN OF THE LOWER CONTINENTAL CRUST, NORTHERN TANZANIA

Adam T. Mansur, M.S., 2008

Directed By: Professor Roberta L. Rudnick
Department of Geology

Granulite xenoliths from the East African rift in Tanzania sample the lower continental crust beneath both the stable Tanzanian craton and the adjacent, polymetamorphic Mozambique belt. Protoliths of surface rocks in both terranes formed 2.8 to 2.6 Ga ago, but only the Mozambique belt underwent significant post-Archean metamorphism. Most granulite xenoliths represent mafic magmas formed in a convergent margin at ca. 2660 Ma that were subsequently metamorphosed at lower crustal conditions. However, a small number of xenoliths are more similar to intraplate magmas, suggesting that at least two episodes of lower crustal growth occurred during the Archean. No post-Archean additions to the crust were detected beneath either terrane, but xenoliths from the Mozambique belt record high *P-T* conditions, suggesting equilibration at the base of orogenically thickened crust. By contrast, xenoliths from beneath the craton equilibrated under conditions typical of unthickened continental crust.

AGE, COMPOSITION, AND ORIGIN OF THE LOWER CONTINENTAL CRUST, NORTHERN TANZANIA

By

Adam T. Mansur

Thesis submitted to the Faculty of the Graduate School of the
University of Maryland, College Park, in partial fulfillment
of the requirements for the degree of
Master of Science
2008

Advisory Committee:
Professor Roberta L. Rudnick, Chair
Professor William F. McDonough
Professor Richard J. Walker

Acknowledgements

I would like to acknowledge the geology department of Colgate University, particularly Dr. William Peck, for introducing me to the field of geology; the graduate students of the geology department at the University of Maryland, for being pleasant company; Dr. Shukrani Manya, for publishing useful papers and being a tragically underutilized resource about Tanzanian geology; my thesis committee, including Drs. Roberta Rudnick, William McDonough, and Richard Walker, for their insight and patience; Dr. Madalyn Blondes, for her comments on a draft of this thesis; my family, for their encouragement; and Sarah Sillin, for putting up with me as I muddled slowly, very slowly, through this project.

This research was funded by NSF grant EAR0337255. Field work was funded by National Geographic grant #7835-05.

Table of Contents

List of Tables

List of Figures

Chapter 1: Introduction

Processes operating in the lower third of the continental crust, including partial melting, basaltic underplating, convective thinning, and density foundering, play a vital role in the large-scale differentiation of the crust, in regulating the transfer of material between the crust and mantle, and in providing heat during regional metamorphism (e.g., Rudnick and Gao, 2003). Understanding this part of the crust is therefore key to answering questions about the formation and evolution of the continents.

Granulite-facies xenoliths, fragments of the lower crust transported to the surface via magmatism, offer an opportunity to constrain the age and origin of the lower continental crust (Rudnick, 1992). A significant limitation to this approach is the rarity of crustal-xenolith-bearing lavas. These are rare in general, but are particularly uncommon in Archean terranes, where thick lithospheric keels prevent deformation and generally preclude basaltic volcanism. Kimberlites erupted through cratons have proven the most fertile sources of cratonic crustal xenoliths to date, but even so, reports of such xenoliths have until recently been rare. Xenolith studies have thus far been limited to only a handful of cratons, including the Kaapvaal Craton (Rogers, 1977; Rogers and Hawkesworth, 1982; Huang et al., 1995; Schmitz and Bowring, 2003); the Wyoming Craton (Leeman et al., 1985); the Baltic Shield (Kempton et al., 1995; Kempton et al., 2001; Downes et al., 2001); the Dharwar craton (Dessai et al., 2004); and the North and South China Cratons (Liu et al., 2001; Zheng et al., 2003; Yu et al., 2004; Dai et al., 2008).

Granulite xenoliths have been found in several rift volcanoes erupted through the

Archean crust of northern Tanzania (Jones et al., 1983; Cohen et al., 1984). This terrane includes the Tanzanian craton and the polymetamorphic Mozambique belt (Fig. 1). Lithosphere comprising both the craton and metamorphic belt formed during the late Archean, but the two terranes record very different post-Archean histories. Whereas the Tanzanian craton has not been significantly deformed since the Archean, the Mozambique belt has undergone at least two cycles of collision and metamorphism, during the Usagaran (ca. 2.0 Ga) and East African (ca. 640 Ma) orogenies (Fritz et al., 2005). Likewise, the large-scale structures of the terranes differ, with the craton being underlain by a thick mantle lithospheric keel that is absent beneath the metamorphic belt (e.g., Ritsema, 1998; Nyblade, 2002; Chesley et al., 1999).

Granulite xenoliths recovered from both the craton margin and Mozambique belt allow the crust underlying both terranes to be characterized and compared. The analysis of the xenoliths presented here was undertaken with two fundamental aims: first, to characterize, in detail, a segment of Archean lower crust, and second, to determine how lower crustal processes contributed to the evolution of the Tanzanian craton and Mozambique belt. To these ends, a broad array of geochemical techniques – including thermobarometry, whole-rock major, trace-element, and isotope geochemistry, and U-Pb zircon dating – have been applied to granulite xenoliths from Tanzania.

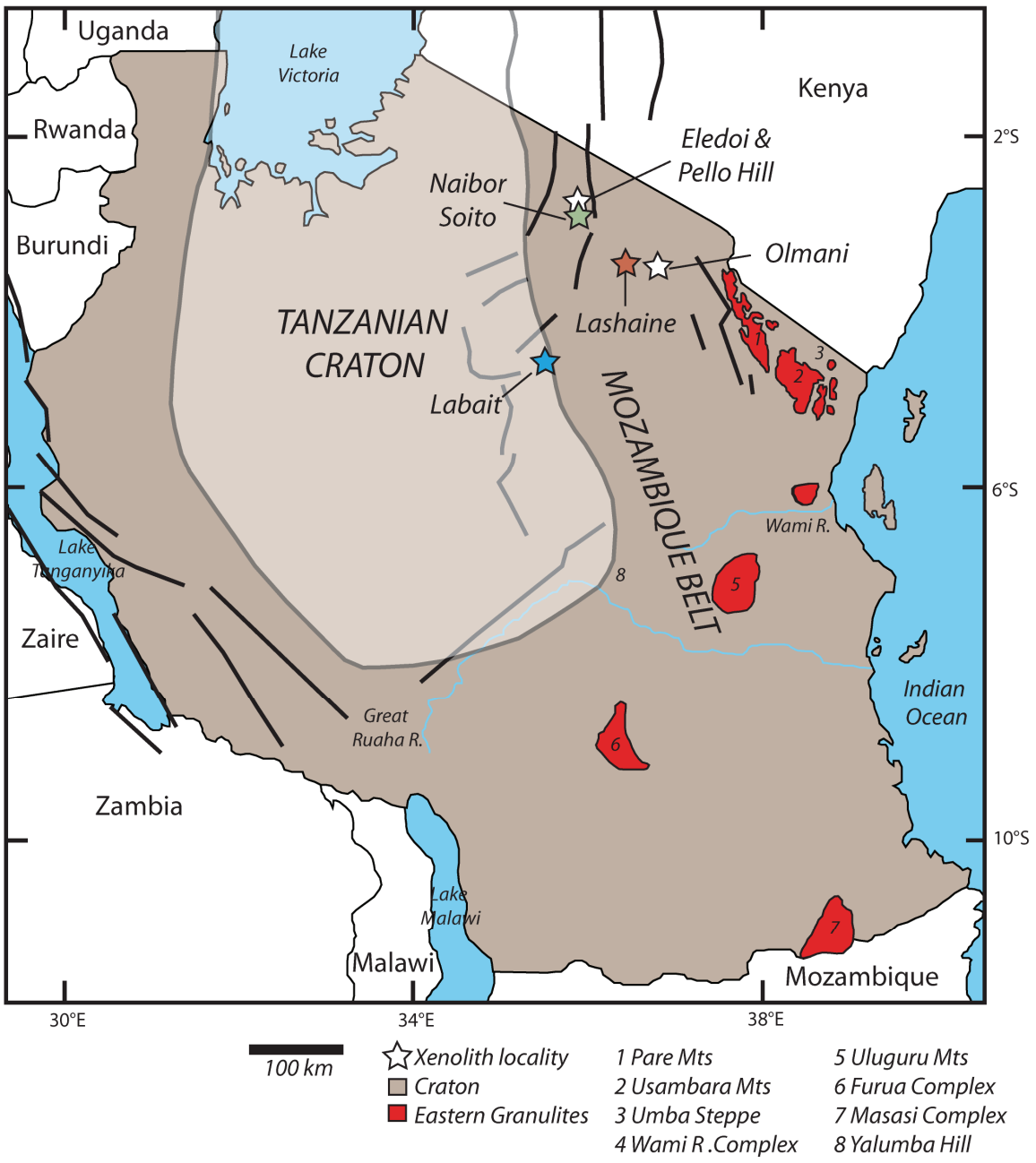

Figure 1. Simplified geological map of Tanzania. Heavy black lines represent faults that define the East African rift. Colored stars indicate xenolith localities described in this study. Modified after Nyblade (1997).

Chapter 2: Geological History

2.1 Formation and metamorphic history

The Tanzanian craton (Fig. 1) consists of amphibolite-grade granitoids associated with minor amphibolite, schist, marble, and quartzite. Migmatic gneisses are common, and high-grade basement is overlain by greenstone belts in the northern half of the craton (Schlüter, 1997). Volcanic rocks in these greenstone belts are geochemically similar to magmatic rocks from modern convergent margins and were emplaced in distinct intervals between 2820 and 2650 Ma ago. Granitic magmatism associated with the greenstone belts occurred somewhat later (2650-2500 Ma) and has been linked to the final stabilization of the Tanzanian craton at this time (Manya and Maboko, 2003; Manya et al., 2006; 2007; 2008).

The craton has not been deformed significantly since it stabilized, but some degree of thermal overprinting is evident in disturbed Rb-Sr whole-rock isochrons reported by Bell and Dodson (1980) and Proterozoic Rb-Sr biotite ages from the craton margin measured by Maboko (2000). Seismic data (Ritsema et al., 1998; Weeraratne et al., 2003), low heat flow (Nyblade et al., 1990), and mantle xenolith *P-T* estimates, compositions, and Re depletion ages (Chesley et al., 1999; Lee and Rudnick, 1999) show that a refractory lithospheric keel has persisted beneath the craton from ca. 2.8 Ga to the present. The current base of this keel extends to ~150 km depth, below which mantle xenoliths exhibit more fertile compositions. It is not clear whether the present thickness represents the original thickness of the craton or whether the keel was thinned during the Proterozoic or later (Chesley et al., 1999).

The Mozambique belt overthrusts and extends ~300 km east of the craton's eastern margin. Fritz et al. (2005) provide an excellent account of the history of deformation and metamorphism in this belt in central and southern Tanzania. The Mozambique belt is dominated by Archean crust that was reworked during two metamorphic episodes, the Usagaran (ca. 2.0 Ga) and East African (ca. 640 Ma) orogenies. Because the East African orogeny (described below) overprinted the Usagaran terrane, the extent of the older terrane is unclear and commonly can only be inferred through the existence of Paleoproterozoic zircons in high-grade rocks. In the area bordering the southeastern part of the craton and south of the Great Ruaha River (Fig. 1), Usagaran deformation has not been overprinted and is recognized by the presence of abundant, undeformed, post-orogenic intrusions from 1.8 to 2.0 Ga (Collins et al., 1999; Sommer et al., 2005; Fritz et al., 2005). In the Yalumba Hill area (#8 in Fig. 1), eclogite and associated rocks preserve a MORB-like REE pattern and evidence for mineral reactions consistent with a clockwise *P-T* path, leading Möller et al. (1995) to conclude that the Usagaran terrane formed in an ancient zone of crustal thickening and subduction. Zircons from Yalumba Hill date to 2000 Ma and are interpreted to reflect the peak of Usagaran metamorphism (Möller et al., 1995).

Metamorphic rocks comprising the majority of the Mozambique belt of Tanzania are part of the Neoproterozoic East African Orogen, a discontinuous, ~6000 km metamorphic belt representing a zone of continent-continent collision and a major suture in the Gondwana supercontinent (Stern, 1994; Meert, 2003; Fritz et al., 2005). Because the crustal xenoliths from the Mozambique belt considered in this study were recovered from northern Tanzania, north of the inferred extent of the Usagaran terrane, the East

African orogeny figures more prominently in the following discussion.

In Tanzania, the East African orogen has been divided on the basis of geochronology and *P-T* paths into the Western and Eastern Granulites. Metamorphic zircons from both domains cluster at ca. 640 Ma, which has been taken to date peak metamorphism (Maboko, 2000; Johnson et al., 2003; Sommer et al., 2003). The Western Granulites make up the majority of the belt and consist predominantly of Archean material (2.5-2.9 Ga; Möller et al., 1998; Johnson et al., 2003; Sommer et al., 2003) reworked at amphibolite- to granulite-facies conditions at ca. 640 Ma. *P-T* paths in these rocks are counterclockwise, consistent with crustal thickening (Sommer et al., 2003; Fritz et al., 2005), but syn-orogenic magmatism is absent. In contrast, the Eastern Granulites occur in extensive outcrops of granulites whose protoliths formed at 700-1000 Ma (Möller et al., 1998; Maboko, 2000; Maboko and Nakamura, 2002). These granulite bodies are confined to the eastern part of the Mozambique belt and are thought to represent pre-collision, mid-crustal intrusions formed in island arcs off the margin of the Tanzanian craton. The increase in peak metamorphic grade from the craton margin to the Eastern Granulites has been interpreted to represent westward propagation of thrust sheets onto the craton margin, accompanied by hinterland extension that allowed exhumation of the young, high-grade Eastern Granulites (Fritz et al., 2005).

High heat flow (40-90 mW m^{-2} away from the rift) and relatively low mantle seismic wave velocities imply that no lithospheric keel presently underlies the Mozambique belt (Nyblade et al., 1990; Nyblade, 1997; Nyblade, 2002). However, peridotite xenoliths recovered from volcanoes in northern Tanzania nevertheless have refractory compositions (Rudnick et al., 1994) and Archean Re-depletion ages (Burton et

al., 2000; J. Chesley, unpublished data), implying that the continental mantle, while relatively thin (~100 km), is compositionally similar to the keel beneath the Tanzanian craton. Shear wave velocities indicate that the structure of the crust in both the Tanzanian craton and metamorphic belt is similar, consisting of a 10 to 15 km thick upper crust and a mafic lower crust that grades into the mantle at approximately 40 km depth (Julià et al., 2005).

2.2 Rift volcanism and xenolith localities

The East African Rift propagated into contact with the northern margin of the Tanzanian Craton by ca. 12 Ma and split into two branches that follow its eastern and western margins (Nyblade and Brazier, 2002). Extension, sedimentary basin formation, and volcanism are concentrated in the relatively weak crust of the metamorphic belts bordering the craton, though the rift has also propagated into the eastern part of the craton (Ritsema et al., 1998; Nyblade and Brazier, 2002).

Initial rift volcanism (ca. 1-8 Ma) produced large shield volcanoes composed primarily of alkaline basalt (Dawson, 1992). The opening of the modern, N-S trending rift at ca. 1.2 Ma was accompanied by a change in eruption type and lava composition. Recent volcanic activity is characterized by eruptions of alkali-rich lava from small tuff cones and craters (Dawson, 1992). The lower crustal xenoliths discussed here were collected from three morphologically young (<1 Ma) tuff cones from the eastern branch of the rift, including Labait on the craton margin and Lashaine and Naibor Soito within the Mozambique belt (Fig. 1).

Chapter 3: Analytical Methods

3.1 Petrography and thermobarometry

Xenoliths from each locality were examined in hand sample and thin section (Table 1). Approximately 10 samples from each locality were selected for geochemical analysis. Compositions of major phases, including plagioclase, orthoclase, clinopyroxene, orthopyroxene, garnet, biotite, and hornblende, were measured by S. Timpa using the JXA-8900 SuperProbe with WD/ED Combined Electron Probe Microanalyzer (EPMA) at the University of Maryland, College Park (UMCP). Reported compositions are averaged from 3-5 separate analyses from the same crystal domain. Phase chemistry for eight Lashaine xenoliths (89-726, 89-729, 89-730, 89-731, 89-733, 89-734, 89-741, 89-744) are from unpublished EDS analyses performed by R.A. Sproule at the Australian National University and provided by R.L. Rudnick. Minerals from samples 89-727 and 89-739 were analyzed using both techniques and give comparable results. The newer data are reported.

Where appropriate assemblages were present (e.g., garnet-clinopyroxene, garnet-orthopyroxene), phase compositions were used to calculate equilibration pressures and temperatures (*P*-*T*). Details of these calculations are provided in the Results section.

TABLE 1: Sample classification, mineralogy, and microstructure

Sample	Major phases	Accessory phases	Notes
Labait (S 4°34.028' E 35°25.876')			
			Two-pyroxene granulites
LB04-04	pl-cpx-opx-ilm	ap, zrn	equigranular
LB04-09	pl-opx-cpx	ap, ilm	medium-grained pl and bimodal px, moderately altered along grain boundaries
LB04-12	pl-opx-cpx	bt, ilm	medium-grained pl and bimodal px, moderately altered along grain boundaries
LB04-16	anti-cpx-opx	ap, bt, ilm, zrn	medium-grained pl and bimodal px, moderately altered along grain boundaries
LB04-19	anti-opx-cpx	ap, ilm, mz,	medium-grained pl and bimodal px, moderately altered along grain boundaries
LB04-34	anti-opx-cpx	ap, ilm, zrn	medium-grained pl and bimodal px, moderately altered along grain boundaries
LB04-36	pl-opx-cpx-qtz	ap, zrn	mottled medium-grained pl and bimodal px, moderately altered along grain boundaries
LB04-38	pl-opx-cpx	ap, ilm, mz	equigranular
LB04-41	anti-opx-cpx	ap, bt, ilm	medium-grained pl and bimodal px, moderately altered along grain boundaries
LB04-46	anti-opx-cpx	ap, ilm, zrn	mottled medium-grained pl and bimodal px, extensively altered along grain boundaries
LB04-50	anti-cpx-opx	ap, ilm	medium-grained pl and bimodal px, weakly foliated
LB04-52	anti-opx-cpx	ap, ilm, zrn	medium-grained pl and bimodal px, weakly foliated
LB04-53	anti-opx-cpx	ap, ilm, zrn	medium-grained pl and bimodal px, weakly foliated
LB04-65	anti-opx-cpx	ap, zrn	compositionally banded polygonal aggregate with medium-grained pl, bimodal px, and qtz, heavily altered along grain boundaries
LB04-93	anti-opx-cpx	ap, ilm	medium-grained pl and bimodal px, moderately foliated
LB-48	anti-opx-cpx	ap, mz, zrn	medium-grained pl and bimodal px
			Hornblende-two-pyroxene granulites
LB04-07	pl-hbl-cpx-opx	ap, ilm	equigranular, with mm-scale compositional bands defined by hbl
LB04-48	pl-opx-cpx-hbl	ap, bt, ilm, mz	equigranular, with mm-scale compositional bands defined by hbl
LB04-82	pl-hbl-cpx-opx	ap, bt, ilm, zrn	equigranular, with mm-scale compositional bands defined by hbl

Note: Major phases listed in order of abundance. Accessory phases listed alphabetically. Mineral abbreviations are as follows: anti, antiperthite; al; allanite; ap, apatite; bt, biotite; cpx, clinopyroxene; ilm, ilmenite; gt, garnet; hbl, hornblende; ky, kyanite; mz,monazite; pl, plagioclase; opx, orthopyroxene; qtz, quartz; rt, rutile; ttn, titanite; and zrn, zircon

TABLE 1: Sample classification, mineralogy, and microstructure

Sample	Major phases	Accessory phases	Notes
Labait (cont.)			
			Garnet-orthopyroxene granulites
LB04-39	pl-gt-qtz-opx	ap, rt, zrn	gt porphyroblasts in polygonal matrix of pl, opx, and qtz, extensively altered along grain boundaries
LB04-91	anti-gt-qtz-opx	ap, rt, zrn	cut by irregular, discontinuous bands of qtz and gt
			Anorthosite
LB04-27	pl-gt-opx	cor, mt, spl	polygonal plagioclase cut by veins of secondary mineralization replacing mafic phases
Lashaine (S 3°22.052' E 36°25.457')			
			Garnet-clinopyroxene granulites
89-726	pl-cpx-gt	ky, rt	cpx atolls with gt coronae in plagioclase matrix
89-727	pl-cpx-gt	ap, ky	elongated cpx atolls with gt coronae in plagioclase matrix
89-729	pl-cpx-gt	rt, ttn	mafic atolls and cpx megacrysts in pl-rich matrix
89-730	cpx-gt-pl-opx	ilm, rt	equigranular mosaic of pl, px, and gt
89-731	pl-cpx-gt	rt, ttn	mafic atolls and cpx megacrysts in pl-rich matrix
89-732	pl-cpx-gt	ky, rt	cpx atolls with gt coronae in plagioclase matrix
89-734	cpx-gt-pl-opx	ap, rt	equigranular mosaic of pl, px, and gt
89-735	pl-cpx-gt	ky	mafic atolls and cpx megacrysts in pl-rich matrix
89-739	pl-cpx-gt-opx	ky	cpx atolls with gt coronae in plagioclase matrix
89-741	pl-cpx-gt-opx	ky	cpx atolls with gt coronae in plagioclase matrix
89-742	pl-cpx-gt-opx	ky, rt	cpx atolls with gt coronae in plagioclase matrix
89-744	pl-cpx-gt-opx	ap	cpx atolls with gt coronae in plagioclase matrix
			Biotite granulites
89-733	pl-bt-cpx-opx-gt	ap, ilm, zrn	fine-grained, with a foliation defined by alignment of the biotite crystals
89-745	pl-bt-cpx-opx-gt	ilm, zrn	fine-grained, with radiating clusters of opaque biotite

TABLE 1: Sample classification, mineralogy, and microstructure

Sample	Major phases	Accessory phases	Notes
Naibor Soito (S 2°46.884' E 36°0.831')			
			Quartz granulites
NS04-01	pl-qtz-opx	anti, ilm, zrn	irregular clusters of coarse qtz+pl and fine, embayed px in pl-qtz-opx groundmass
NS04-05	pl-opx-qtz-gt	ap, bt, ilm, hbl, zrn	irregular clusters of coarse qtz+pl and embayed px in pl+qtz-opx groundmass
NS04-104	pl-qtz-opx-cpx	ap, ilm, zrn	equigranular, with scattered, embayed px
NS04-13	(A) pl-qtz-opx cpx (B) pl-opx-cpx	ap, ilm	composite xenolith comprised of felsic (A) and mafic (B) layers
NS04-53	qtz-pl-gt-opx	ap, ilm	granoblastic, with abundant felsic minerals
NS04-73	pl-cpx-qtz-opx	ilm	compositionally banded into mafic- and felsic-rich layers, with irregular clusters of qtz+pl and fine-to-course px in pl-qtz-px groundmass
NS04-83	pl-qtz-cpx-opx	ap, ilm	equigranular, with scattered, embayed px
NS04-91	pl-qtz-opx-cpx-gt	al, ap, bt, ilm, hbl, zrn	irregular clusters of coarse qtz+pl and embayed px in pl-qtz-opx groundmass
NS04-93	pl-cpx-gt-opx	ap, zrn	compositionally banded into mafic- and felsic-rich layers, with irregular clusters of qtz+pl and fine-to-course px in pl-qtz-px groundmass
NS04-96	pl-qtz-opx-cpx	ap, ilm	equigranular, with scattered, embayed px
NS04-98	pl-qtz-opx-cpx	bt, ilm	equigranular, with scattered, embayed px
W3S-2	pl-qtz-opx-cpx	ap, ilm, zrn	equigranular, with scattered, embayed px
			Quartz-free granulites
NS04-61	pl-cpx-opx-gt	bt, ilm	coarse pl and px rimmed by gt coronae
NS04-80	pl-cpx-gt-opx	ap, ilm, rt	coarse pl and px rimmed by gt coronae
NS04-150	pl-hbl-opx-bt-cpx	ap, ilm	contains abundant hbl

3.2 Major, trace element, and isotope measurements

Samples were chipped using a rock hammer. Minimally altered chips from each sample were powdered in an agate ring mill to produce whole-rock powders suitable for geochemical analysis. Powders were sent to Washington State University, Pullman, or Franklin & Marshall College for analysis of major and selected trace elements via x-ray fluorescence (XRF). Precision for XRF analyses at the Washington State lab is reported in Johnson et al. (1999) and on the laboratory website (http://www.sees.wsu.edu/Geolab/note/xrfprecision.html). Relative precision of replicate analyses of GSP-1 are <5% for Ba, Rb, Sr, Zr, Nb, Zn, Ce, Th; <10% for Y, Ga, and Pb; and >10% for Ni, Cr, Sc, Cu, and La (2σ standard deviation, n=98). However, absolute errors are similar across a wide range of element concentrations. For example, Rb concentrations in standards reported in Johnson et al. (1999) range from 45 to 253 ppm, but the reported standard deviation is constant at 2 ppm (2σ). Similar behavior is observed for most elements. The Washington State XRF lab therefore reports uncertainty in terms of the weighted, absolute deviation of more than 200 pairs of replicate analyses spanning a wide range of concentrations. Uncertainties at the 2σ-level are <3 ppm for Cr, Sc, Rb, Y, Nb, Ga, Th, U, and Bi; <5ppm for Ni, V, Sr, Zr, Zn, and Nd; <8 ppm for Cu, La, Ce, Cs; and <12 ppm for Ba.

The Franklin and Marshall XRF laboratory provides less detailed information about the precision and accuracy of its procedure, reporting only three replicate analyses of in-house standard 98-54. Because of the small number of analyses being considered, I have for each element used the range of measured concentrations divided by their mean concentration to estimate the relative precision of the data. Relative precision for trace

elements in 98-54 is <5% for Rb, Sr, Y, Zr, Nb, Ga, Cu, Zn, Ba, Co, Ce, and Sc; <10% for Ni and V; <25% for Cr, La, and Pb; and >50% for Th and U. The accuracy of this method, based on comparison of measured and nominal concentrations for reference standards BHVO-1 and QLO-1, is typically better than 5% for elements present in concentrations greater than 10 ppm. At lower concentrations, accuracy declines markedly and measured values may be offset by 10-100% from accepted values.

Two samples were sent to both laboratories in order to make interlaboratory comparisons. These replicate analyses give broadly comparable results for the major elements (<4% for all oxides except MnO and Fe_2O_3 [3-10%] and P_2O_5 [10-40%]) and trace elements reported here (<15% difference for most elements). However, Rb, Y, and Zn concentrations differ by >20% between the two laboratories in one or both samples. ICP-MS trace-element data, described below, compare more favorably to data from the Washington State XRF lab.

Whole-rock powders were dissolved for solution analyses of trace elements and radiogenic isotopes at UMCP. All acids used during sample processing were quartz- or Teflon-distilled to minimize contamination. Unspiked powders were dissolved once, with the resulting solution split by weight into aliquots for trace element and isotopic analysis. For spiked samples, separate solutions were prepared for each procedure, with the isotopic split being mixed with known quantities of Rb (enriched to 98.0 percent ^{87}Rb), Sr (enriched to 80.6 percent ^{84}Sr), and rare-earth element (enriched to 97.6 percent ^{150}Nd and 97.7 percent ^{149}Sm) spike solution prior to dissolution.

Approximately 20 to 40 mg of powder were dissolved per sample. To attain dissolution of resistant phases, notably zircon, powders were dissolved in steel-jacketed

Teflon Parr bombs in 3 ml of a 5:1 mixture of concentrated hydrofluoric and nitric acid at >160°C for at least 2 days. Sample solutions were then dried in 3 ml nitric acid, then 3 ml hydrochloric acid to eliminate fluoride compounds. The drying process was repeated as necessary until no solids were observed. Zr concentrations measured in standard GSP-1 suggest that this procedure is sufficient to dissolve zircon, but comparison between XRF and ICP-MS trace-element data indicates that complete dissolution was rarely achieved for samples containing >100 ppm Zr (Fig. A1h).

Trace-element concentrations were determined using the low resolution mode of the ThermoFinnigan Element 2 single-collector ICP-MS at UMCP. The instrument was tuned each session to maximize sensitivity and minimize oxide formation (3-5%, based on UO/U). Solutions were diluted by a factor of 50-1000 prior to analysis and mixed with a known quantity of 3 ppb In solution, allowing measured counts to be corrected for instrumental drift. Because of the wide range of trace-element concentrations in some samples, solutions were typically run twice, at different dilutions. Rock reference materials ranging from basalt to granite (BHVO-1, GSP-1, and AGV-1) were prepared and analyzed at the same time as sample solutions.

To minimize memory effects, the sipper tube and nebulizer were washed for 2 minutes each in 5% and 2% nitric acid between samples. Concentrations were determined based on bracketing analyses of BHVO-1 by comparing the drift-, blank-, and oxide-corrected counts to the known concentrations of each element in this standard. Analyses of secondary standards suggest that the oxide contributions to measured counts were minor and did not require correction. One exception is BaO interference on Eu. As Ba concentrations in some samples are very high (>5000 ppm in the two-pyroxene granulites

from Labait), interferences between ^{135}BaO and ^{151}Eu and between ^{137}BaO and ^{153}Eu were of particular concern. Because ^{137}Ba is more abundant than ^{135}Ba, interference of BaO on Eu should decrease the measured ^{151}Eu/^{153}Eu ratio. Indeed, ^{151}Eu/^{153}Eu ratio was low by ~10% relative to its accepted value in the most Ba-rich samples. Counts for both isotopes of Eu were corrected to the natural ratio to account for this effect, producing concentrations up to 0.5 ppm (10-20%) lower than those calculated using the uncorrected counts. This difference, while dramatic, applies only to samples with extreme Ba concentrations, including all Labait samples except LB04-07. The correction is much smaller in all other samples (<5%).

Analytical uncertainties, calculated based on replicate analyses of standards, are provided in Table 2. The standard-bracketing method typically produces concentrations that agree well with measurements of the same samples made via XRF and with the nominal values for secondary standards AGV-1 and GSP-1. However, several problems may compromise the precision and accuracy of this technique, including uncertainty in the nominal element concentrations in BHVO-1 (up to 10% at 1σ, according to GEOREM), matrix effects, and disparities in element concentrations between standard and sample materials. Nevertheless, concentrations measured in secondary standards agree well with published values (<10% difference for most elements), suggesting that the accuracy of this technique is acceptable (Table 2).

Trace-element concentrations reported here include data measured using both XRF and ICP-MS. As a rule, XRF data were preferred for elements present in tens of ppm or greater, whereas ICP-MS data were preferred for less abundant elements. Among elements measured by both methods, agreement between the two for a given element is

never better than 20% across the entire sample set, but V, Rb, Sr, Y, La, Ce, and Nd generally yield similar concentrations (Fig. A1). Agreement for these elements is commonly better than 10%, with larger disparities usually related to low concentrations (<10 ppm) of an element. Other elements, including Sc, Cr, Cu, Zr, Nb, Ba, Pb, and Th, differ dramatically. Common problems that may contribute to differences between the methods include: (1) high blank concentrations in solution analysis (Sc, Cu, Ba, Pb); (2) concentrations near or below the limit of determination for XRF (Cs, Nb, Th); and (3) incomplete dissolution of zircon (Zr, notably in many Labait and most Naibor Soito xenoliths). Concentrations measured via XRF are preferred for the following elements: Sc, V, Cr, Ni, Cu, Zn, Ga, Rb, Sr, Y (except 89-729 and 89-735, which contained ~1 ppm Y), Zr, and Pb. Concentrations measured via ICP-MS are preferred for the following elements: Nb, the REE, Th, and U. Precision and accuracy of ICP-MS determinations are presented in Table 2.

Solutions intended for isotopic analysis were purified chromatographically. Solutions were first eluted through columns containing AG50W-X12 (200-400 mesh) resin to produce rough cuts of Rb, Sr, and Sm-Nd, which were then purified using element-specific resins.

Sr cuts were purified to remove Rb, Ca, and Ba using Sr-SPEC resin. Purified cuts were evaporated along with Ta oxide onto degassed Re filaments and measured in positive ion mode on the VG Sector 54 thermal ionization mass spectrometer (TIMS) at UMCP. Peak shape and coincidence were assessed and adjusted as necessary prior to each analytical session. For each measurement, filaments were gradually heated to 1450 to 1600 °C using a current of 2.3 to 2.8 amps, producing a stable, 0.5 to 3 V signal on

mass 88. Ion beams corresponding to ^{84}Sr, ^{86}Sr, ^{87}Sr, ^{88}Sr, and ^{85}Rb were then measured across three Faraday cups. At least 100 Sr isotope ratios were measured per sample, with the final ratios being fractionation-corrected to $^{86}Sr/^{88}Sr=0.1194$. Rb concentrations in the purified cuts were typically very low (<1000 cps), and the effect of ^{87}Rb on the measured $^{87}Sr/^{86}Sr$ is minimal. Standard SRM987 was measured at least once during each day of analysis, yielding a mean $^{87}Sr/^{86}Sr=0.710243\pm28$ (2σ, n=18, unnormalized) over 14 days of analysis. $^{87}Sr/^{86}Sr$ ratios were normalized based on the values measured for SRM987 during each analytical session assuming a nominal $^{87}Sr/^{86}Sr$ ratio of 0.71025.

Sm-Nd cuts were purified via elution through columns containing LN-SPEC resin. Pure cuts of both elements were measured using the Nu Plasma MC-ICP-MS at UMCP. Both Aridus and Apex desolvating nebulizers were used over the course of this project. The MC-ICP-MS was tuned prior to analysis using a 50 or 100 ppb solution of the element of interest. Peak shape and coincidence were adjusted each day to produce broad, flat-topped peaks. During analysis, each set of peaks was integrated for 10 seconds to produce one set of ratios. At least 60 sets of ratios were measured for Nd, compared to 40 sets for Sm. For analyses of Nd, mass 144 was placed in the axial cup and ion beams corresponding to all isotopes of Nd and ^{147}Sm were measured. For analyses of Sm, mass 146 was placed in the axial cup and all isotopes of Sm and ^{145}Nd, ^{146}Nd, and ^{148}Nd were measured. The sipper tube was rinsed for 2 minutes each in 5%, then 2% nitric acid between samples to prevent cross-contamination, and each set of five samples was bracketed by multiple analyses of the AMES Nd standard. Raw $^{143}Nd/^{144}Nd$ ratios were normalized to $^{146}Nd/^{144}Nd=0.7219$, then corrected to the average value for AMES for a given analytical session, assuming a nominal value for AMES of 0.512165. AMES

yielded a mean $^{143}Nd/^{144}Nd$ of 0.512194 ± 52 (2σ, n=94, unnormalized) over 9 analytical sessions.

The discussion of isotope geochemistry below utilizes epsilon notation, which is calculated as follows:

$$\varepsilon_{Nd} = 10^4([^{143}Nd/^{144}Nd_{measured}]/[^{143}Nd/^{144}Nd_{CHUR}]-1)$$

where CHUR is the chondritic uniform reservoir ($^{143}Nd/^{144}Nd_{CHUR}$ = 0.512638, $^{147}Sm/^{144}Nd$ = 0.1967). This notation has the advantage of giving the same values regardless of the normalization scheme employed. The following section also includes calculations of the Nd depleted mantle model age (T_{DM}), which estimates, based on the present-day $^{143}Nd/^{144}Nd$ and $^{147}Sm/^{144}Nd$ ratios, the time at which a given rock had the same isotopic ratio as the depleted mantle. Parameters for the T_{DM} calculation follow DePaolo (1981). A viable model age calculation requires that neither the $^{143}Nd/^{144}Nd$ nor the $^{147}Sm/^{144}Nd$ ratio of a sample have been disrupted since extraction.

TABLE 2: ICP-MS standard data

		BHVO-1			BHVO-1			AGV-1				
	Dilution		1:100			1:1000				1:100		
			n=14			n=8				n=6-8		
Element	Mass	Nominal	Mean	RSD (2σ)	Mean	RSD (2σ)	Range	Nominal	Mean	RSD (2σ)	Range	Accuracy
Sc	45	31.0	-	-	31.2	2.6%	3.1%	12.3	11.7	31%	36%	5.0%
V	51	318	-	-	321	2.9%	4.3%	119	131	19%	20%	9.9%
Cr	53	287	-	-	289	2.1%	3.1%	9.4	18.5	47%	49%	97%
Co	59	45.0	-	-	45.2	4.4%	6.2%	15.2	17.0	86%	98%	12%
Cu	63	137	-	-	133	7.5%	10%	58.0	47.0	13%	17%	19%
Rb	85	9.2	-	-	9.4	7.7%	11%	66.6	62.5	13%	15%	6.2%
Sr	86	396	-	-	415	3.6%	4.9%	660	687	7.7%	8.7%	4.2%
Y	89	26.0	-	-	26.0	7.0%	9.5%	19.0	17.0	22%	24%	10.8%
Zr	91	174	173	4.7%	174	0.7%	1.1%	231	235	0.6%	1.0%	1.7%
Nb	93	1.05	1.05	4.6%	-	-	-	14.6	13.8	19%	22%	5.5%
Cs	133	0.10	0.1	2.4%	0.10	14%	21%	1.3	1.3	2.1%	3.0%	6.3%
Ba	135	133	-	-	114	17%	23%	1200	1838	36%	51%	53%
Ba	137	133	-	-	112	11%	14%	1200	1660	42%	57%	38%
La	139	15.5	15.3	3.5%	15.3	5.0%	7.2%	38.2	39.3	2.4%	3.8%	2.9%
Ce	140	38.1	36.4	16%	37.8	5.4%	7.8%	67.6	68.5	5.6%	7.0%	1.4%
Pr	141	5.4	5.4	2.6%	-	-	-	8.3	8.4	1.7%	2.5%	1.1%
Nd	145	24.7	25.2	2.7%	24.4	5.5%	6.9%	31.7	31.8	2.5%	3.5%	0.4%
Sm	147	6.1	6.2	2.7%	6.1	6.3%	8.3%					
Eu	151	2.1	2.1	4.1%	2.1	6.1%	9.0%	1.6	1.6	5.9%	7.0%	1.7%
Eu	153	2.1	2.1	4.1%	2.1	7.4%	10.2%	1.6	1.6	5.9%	7.0%	1.7%
Gd	157	6.3	6.5	2.3%	-	-	-	4.7	5.0	7.6%	12%	7.0%
Tb	159	0.96	0.98	2.5%	0.95	5.1%	7.0%	0.69	0.68	1.6%	2.3%	1.6%
Dy	163	5.3	5.4	2.5%	-	-	-	3.6	3.6	3.1%	4.4%	0.7%
Ho	165	0.98	0.98	3.6%	0.98	7.2%	10.3%	0.68	0.67	3.7%	5.7%	2.0%
Er	166	2.6	2.6	2.6%	-	-	-	1.8	1.9	5.4%	6.9%	5.5%
Tm	169	0.33	0.34	2.5%	0.32	15%	21%					
Yb	172	2.0	2.0	3.1%	-	-	-	1.6	1.7	4.6%	7.0%	1.5%
Lu	175	0.27	0.27	3.1%	0.27	7.5%	9.6%	0.24	0.2	4.0%	5.8%	3.3%
Hf	178	4.5	4.5	2.7%	-	-	-	5.1	5.3	3.9%	5.9%	3.1%
Pb	208	2.4	2.4	2.7%	2.2	14%	19%	37.4	44.0	20%	24%	18%
Th	232	1.2	1.2	3.8%	-	-	-	6.4	6.3	4.2%	6.8%	0.8%
U	238	0.41	0.41	3.4%	-	-	-	1.9	1.8	3.9%	5.2%	4.2%

Notes: In-run uncertainty estimated from counting statistics is 5-10% for most elements (2σ). Range is calculated by dividing measured range of concentrations by the mean concentration. Because *n* is small, it may give a more accurate view of the true variability in the ICP-MS measurements. Underlined elements either (a) for BHVO-1, do not reproduce within 10% at both dilutions or (b) for AGV-1, differ from the nominal value by >10%. Sm and Tm in AGV-1 were spiked prior to analysis and are no shown. Nominal values retrieved from GEOREM (August, 2008).

3.3 Laser ablation ICP-MS U-Pb dating of zircon

Zircons were separated from six xenoliths at the Massachusetts Institute of Technology or the Australian National University using conventional magnetic and heavy liquid techniques. Approximately 40 crystals handpicked from each separate were then mounted in epoxy, hand-polished, and imaged using backscattered electrons (BSE) and cathodoluminescence (CL) to reveal internal zoning. BSE and CL images were made using a JEOL JXA-8900 SuperProbe.

The laser ablation procedure used in this study is based on the external standard method described by Chang et al. (2006), which corrects for both time-integrated and instrumental fractionation of Pb and U during analysis. Polished zircon mounts were analyzed using the New Wave 213-nm Nd:YAG laser coupled to the ThermoFinnigan Element 2 single-collector ICP-MS at UMCP. The laser produces a Gaussian beam profile and minimal thermal ablation. He gas was employed to ensure efficient transport of material from the ablation chamber to the mass spectrometer.

Zircon mounts were rinsed with ethanol and deionized water before being loaded into the ablation chamber. Prior to each measurement, the selected spot was pre-ablated via a small number ($\leq$5) of flashes from the laser. The system was then allowed at least two minutes to clear the ablated material before a gas blank was measured. For each spot and blank analysis, eight isotopes were measured: ^{202}Hg, ^{204}(Pb+Hg), ^{206}Pb, ^{207}Pb, ^{208}Pb, ^{232}Th, ^{235}U, and ^{238}U. (^{235}U, while monitored, is not used during data reduction. ^{207}Pb/^{235}U is calculated on the basis of counts of ^{238}U.) Each isotope was measured a total of 300 times over a period of 32 seconds, with individual integration times of 40 ms. Background counts on ^{206}Pb, ^{207}Pb, and ^{208}Pb are <30 cps. Counts on mass 204 are

dominated by ^{204}Hg, making it difficult to estimate the contribution of ^{204}Pb in either the gas blank or during ablation, but for a typical analysis ^{204}Pb probably contributes <50 cps to the 204 signal. Because this value is both small and uncertain, no common Pb correction was applied here. A typical analysis used a beam with a 45% energy flux repeating at 10 Hz to produce a pit 40 μm in diameter. Spot diameters ranged from 30-200 μm, depending on the size of zircon crystals and scale of internal zoning. As per the method of Chang et al. (2006), batches of approximately five analyses of unknown zircons were bracketed by two analyses each of primary zircon standard 91500 (ca. 1060 Ma; Wiedenbeck et al., 1995) and a secondary standard. Both the MCC-12-515E (ca.1778 Ma; Premo, 1991) and Temora 1 (416.8±0.2 Ma; Black et al., 2003) zircons were employed as secondary standards.

Measured ratios were corrected for time-integrated and instrumental fractionation using the Excel macro by Chang et al. (2006). Time-integrated fractionation results from the higher volatility of Pb relative to U and becomes pronounced as ablation proceeds, the ablation crater deepens, and increasing proportions of U condense along the crater walls. As a result of preferential condensation of U, the measured ^{206}Pb/^{238}U and ^{207}Pb/^{235}U ratios increase over time. This effect can be reduced by using ablation pits with an aspect ratio (diameter/depth) close to one (Eggins et al., 1998). Chang et al. (2006) use a slope-intercept method to correct for time-integrated fractionation. In this method, a line is regressed through a plot of the individual measurements of ^{206}Pb/^{238}U, ^{207}Pb/^{235}U, or ^{207}Pb/^{206}Pb that comprise the analysis of one spot. The intercept of this line with the zeroth analysis (that is, the beginning of the measurement) is taken to represent the initial Pb/U ratio. This ratio represents the true isotope ratio minus a correction for

instrumental fractionation, which results primarily from differences in the efficiency of transport for different ions through the mass spectrometer. To correct for instrument bias, each set of sample analyses (~5) was bracketed by analyses of homogenous standards whose isotope ratios have been established precisely via TIMS. Comparison of the accepted and measured values for $^{206}Pb/^{238}U$, $^{207}Pb/^{235}U$, and $^{206}Pb/^{207}Pb$ in the standard zircons allows a fractionation correction to be calculated and applied to unknown zircons. Static fractionation generally skews Pb/U ratios to values 10-20% lower than their true values, but typically has only a small effect (<1%) on $^{207}Pb/^{206}Pb$ ratios.

Individual analyses were inspected to ensure data quality. Analyses for which fewer than 200 sets of ratios were collected (that is, where the laser burned through the zircon prior to the completion of the analysis) were rejected outright. Because a linear trend between Pb/U and ablation time is required to correct time-integrated fractionation, the Pb/U ratios in samples in which this trend is absent or disturbed cannot be used. (This problem could, in principle, also affect the $^{207}Pb/^{206}Pb$ ratio, which is corrected in the same way, but in practice this ratio remains stable even when the Pb/U ratios are disrupted.) Zoning of Pb and U can also be problematic if the Pb/U ratios vary between different domains, though many crystals zoned with respect to Pb-U concentrations or Th/U ratios nevertheless maintain a good correlation between Pb/U and time.

All ratios from the Tanzanian zircons that are presented here were calculated based on fractionation factors from primary standard 91500. Ratios and ages for individual zircon spots were corrected using the four analyses of 91500 bracketing them. In general, the degree of static fractionation did not vary beyond the 1σ uncertainty on the fractionation factor (typically 0.5 to 3%) during a given analytical session, excepting two

days. On 18 April 2007, the calculated fractionation factor increased by ~7% (although this change fell within the 2σ uncertainty of the calculation, which on that day ranged from 2-5%). On 27 September 2007, the fractionation factor increased by ~13%, a change that falls outside error (2-4%) on that day. The reason for this variability is unknown, but these episodes highlight the usefulness of using only the immediately bracketing standards to calculate zircon ages.

Ratios for secondary zircon standards Temora 1 and MCC12-515E are presented in Table 3. MCC12-515E was only employed during one analytical session, for which it yielded an average $^{207}Pb/^{206}Pb$ age of 1779±19 Ma (2σ, n = 8). Temora 1 was used for the other sessions. Concordant ages calculated for this standard during each session range from 406 to 428 Ma, with uncertainties of <15 Ma for all days (2σ). The average $^{206}Pb/^{238}U$ age for all six sessions was 414±31 Ma (2σ, n =34). These data are in good agreement with (albeit with larger errors than) previously reported TIMS analyses for MCC12-515E (ca. 1778 Ma; Premo, 1991) and Temora-1 (416.8 ± 0.2 Ma; Black et al., 2003). Typical analytical precision attained on ratios for 91500 are as follows (all 2σ): 4% for $^{207}Pb/^{235}U$ (range: 2-5%), 5% for $^{206}Pb/^{238}U$ (range: 3-7%), and 7% for $^{207}Pb/^{206}Pb$ (range: 4-10%). Precision on $^{207}Pb/^{206}Pb$ ages for the Tanzanian zircons is typically somewhat better, averaging 2% and ranging from 1-5%. The primary contribution to error is the application of the instrumental fractionation correction.

TABLE 3: Laser ablation U-Pb zircon analyses of secondary standards

Analysis	$\frac{^{207}Pb}{^{235}U}$	$\frac{^{206}Pb}{^{238}U}$	$\frac{^{207}Pb}{^{206}Pb}$	Ages (Ma) $\frac{^{207}Pb}{^{235}U}$	Ages (Ma) $\frac{^{206}Pb}{^{238}U}$	Ages (Ma) $\frac{^{207}Pb}{^{206}Pb}$
Temora 1						
Ap23a08	0.497 ± 0.023	0.0650 ± 0.0018	0.0554 ± 0.0020	410 ± 15	406 ± 11	429 ± 79
Ap23a10	0.527 ± 0.024	0.0684 ± 0.0019	0.0558 ± 0.0020	430 ± 16	427 ± 12	445 ± 78
Ap23a22	0.502 ± 0.024	0.0668 ± 0.0019	0.0545 ± 0.0021	413 ± 16	417 ± 11	394 ± 87
Ap23a54	0.517 ± 0.024	0.0674 ± 0.0028	0.0557 ± 0.0013	423 ± 16	420 ± 17	441 ± 53
Ap23a70	0.490 ± 0.023	0.0653 ± 0.0027	0.0544 ± 0.0013	405 ± 16	408 ± 16	387 ± 53
Ap23a72	0.511 ± 0.024	0.0676 ± 0.0028	0.0548 ± 0.0013	419 ± 16	422 ± 17	404 ± 53
				Pooled U-Pb concordant age (n=6):		*416 ± 5*
My09a17	0.514 ± 0.024	0.0665 ± 0.0016	0.0560 ± 0.0019	421 ± 16	415 ± 9	454 ± 76
My09a19	0.491 ± 0.024	0.0673 ± 0.0016	0.0529 ± 0.0021	406 ± 16	420 ± 9	324 ± 88
My09a37	0.514 ± 0.030	0.0680 ± 0.0019	0.0548 ± 0.0028	421 ± 20	424 ± 12	405 ± 112
My09a39	0.479 ± 0.030	0.0651 ± 0.0021	0.0534 ± 0.0028	397 ± 20	407 ± 13	344 ± 117
My09a57	0.493 ± 0.038	0.0638 ± 0.0019	0.0561 ± 0.0034	407 ± 26	399 ± 11	455 ± 133
My09a59	0.498 ± 0.036	0.0672 ± 0.0017	0.0538 ± 0.0029	411 ± 24	419 ± 10	363 ± 121
				Pooled U-Pb concordant age (n=6):		*415 ± 7*
My10a12	0.589 ± 0.066	0.0635 ± 0.0052	0.0673 ± 0.0048	470 ± 41	397 ± 32	846 ± 144
My10a28	0.466 ± 0.044	0.0633 ± 0.0049	0.0533 ± 0.0025	388 ± 31	395 ± 30	343 ± 105
My10a30	0.537 ± 0.054	0.0627 ± 0.0049	0.0622 ± 0.0034	437 ± 35	392 ± 30	680 ± 113
My10a56	0.531 ± 0.024	0.0671 ± 0.0016	0.0574 ± 0.0023	433 ± 16	419 ± 9	507 ± 86
My10a58	0.521 ± 0.021	0.0662 ± 0.0017	0.0570 ± 0.0018	426 ± 14	413 ± 10	492 ± 71
My10a71	0.494 ± 0.021	0.0673 ± 0.0018	0.0533 ± 0.0019	408 ± 14	420 ± 11	340 ± 78
My10a73	0.549 ± 0.036	0.0687 ± 0.0032	0.0579 ± 0.0029	444 ± 24	428 ± 19	525 ± 107
My10b115	0.548 ± 0.037	0.0682 ± 0.0028	0.0583 ± 0.0028	444 ± 24	425 ± 17	541 ± 104
My10b117	0.515 ± 0.033	0.0665 ± 0.0028	0.0562 ± 0.0024	422 ± 22	415 ± 17	459 ± 94
				Pooled U-Pb concordant age (n=9):		*418 ± 8*
Sp17a14	0.536 ± 0.038	0.0711 ± 0.0045	0.0547 ± 0.0018	436 ± 25	443 ± 27	400 ± 72
Sp17a16	0.541 ± 0.036	0.0713 ± 0.0041	0.0550 ± 0.0019	439 ± 23	444 ± 25	412 ± 77
Sp17a28	0.535 ± 0.037	0.0691 ± 0.0044	0.0561 ± 0.0016	435 ± 25	431 ± 27	458 ± 64
Sp17a30	0.554 ± 0.040	0.0704 ± 0.0046	0.0571 ± 0.0019	448 ± 26	439 ± 28	494 ± 72
Sp17a50	0.520 ± 0.036	0.0686 ± 0.0039	0.0550 ± 0.0024	425 ± 24	427 ± 23	414 ± 98
Sp17a52	0.444 ± 0.030	0.0589 ± 0.0034	0.0547 ± 0.0019	373 ± 21	369 ± 21	401 ± 75
Sp17a54	0.477 ± 0.031	0.0644 ± 0.0033	0.0536 ± 0.0022	396 ± 21	403 ± 20	356 ± 91
				Pooled U-Pb concordant age (n=7):		*428 ± 10*
Sp26a12	0.517 ± 0.042	0.0682 ± 0.0043	0.0550 ± 0.0032	423 ± 28	425 ± 26	410 ± 129
Sp26a14	0.525 ± 0.045	0.0649 ± 0.0043	0.0587 ± 0.0035	429 ± 30	405 ± 26	556 ± 129
Sp26a24	0.488 ± 0.051	0.0660 ± 0.0050	0.0535 ± 0.0043	403 ± 34	412 ± 30	352 ± 176
Sp26a26	0.488 ± 0.037	0.0655 ± 0.0041	0.0540 ± 0.0026	404 ± 25	409 ± 25	373 ± 107
				Pooled U-Pb concordant age (n=4):		*413 ± 13*

TABLE 3: Laser ablation U-Pb zircon analyses of secondary standards (cont.)

Analysis	$\frac{^{207}Pb}{^{235}U}$	$\frac{^{206}Pb}{^{238}U}$	$\frac{^{207}Pb}{^{206}Pb}$	Ages (Ma) $\frac{^{207}Pb}{^{235}U}$	Ages (Ma) $\frac{^{206}Pb}{^{238}U}$	Ages (Ma) $\frac{^{207}Pb}{^{206}Pb}$
Sp27a06	0.509 ± 0.038	0.0649 ± 0.0037	0.0568 ± 0.0029	417 ± 25	405 ± 22	484 ± 110
Sp27a08	0.556 ± 0.042	0.0697 ± 0.0040	0.0579 ± 0.0030	449 ± 27	434 ± 24	524 ± 111
Sp27a22	0.497 ± 0.033	0.0627 ± 0.0032	0.0574 ± 0.0026	409 ± 22	392 ± 19	506 ± 98
Sp27a24	0.503 ± 0.034	0.0633 ± 0.0032	0.0577 ± 0.0027	414 ± 23	395 ± 19	518 ± 100
Sp27a52	0.541 ± 0.043	0.0689 ± 0.0033	0.0569 ± 0.0040	439 ± 28	429 ± 20	488 ± 153
Sp27a54	0.575 ± 0.041	0.0692 ± 0.0030	0.0603 ± 0.0035	461 ± 26	431 ± 18	613 ± 123
Sp27a74	0.548 ± 0.037	0.0632 ± 0.0028	0.0628 ± 0.0031	443 ± 24	395 ± 17	703 ± 102
Sp27a76	0.575 ± 0.045	0.0663 ± 0.0033	0.0629 ± 0.0042	461 ± 29	414 ± 20	705 ± 139
Sp27a78	0.507 ± 0.030	0.0644 ± 0.0023	0.0571 ± 0.0025	417 ± 20	402 ± 14	496 ± 97
				Pooled U-Pb concordant age (n=9):		*406 ± 16*
MCC-515E						
Oc09a08	4.58 ± 0.14	0.3013 ± 0.0059	0.1102 ± 0.0021	1746 ± 26	1698 ± 29	1782 ± 18
Oc09a10	4.49 ± 0.14	0.2957 ± 0.0056	0.1102 ± 0.0021	1730 ± 25	1670 ± 28	1781 ± 17
Oc09a26	4.80 ± 0.15	0.3176 ± 0.0065	0.1095 ± 0.0021	1784 ± 26	1778 ± 32	1769 ± 18
Oc09a28	4.70 ± 0.15	0.3095 ± 0.0063	0.1101 ± 0.0021	1767 ± 26	1738 ± 31	1780 ± 18
Oc09b22	4.36 ± 0.19	0.289 ± 0.012	0.1094 ± 0.0014	1704 ± 36	1636 ± 60	1789 ± 23
Oc09b24	4.36 ± 0.19	0.289 ± 0.012	0.1093 ± 0.0014	1704 ± 36	1636 ± 60	1789 ± 23
Oc09b34	4.31 ± 0.19	0.290 ± 0.012	0.1078 ± 0.0014	1695 ± 36	1641 ± 60	1762 ± 23
Oc09b36	4.39 ± 0.20	0.292 ± 0.012	0.1089 ± 0.0014	1710 ± 37	1652 ± 61	1782 ± 23
				Mean $^{207}Pb/^{206}Pb$ age (n=8):		*1779 ± 19*

Chapter 4: Results

4.1 Petrography

4.1.1 Labait

Twenty-three mafic granulite xenoliths from Labait have been examined in this study. A summary of the petrographic characteristics of these samples (along with those from the Lashaine and Naibor Soito volcanoes) is provided in Table 1. All but one of the Labait xenoliths are meta-gabbros, following the IUGS scheme for crustal rocks.

Three types of meta-gabbroic xenoliths have been defined. The most common are two-pyroxene granulites comprised of antiperthite (or sometimes plagioclase, as in LB04-04), clinopyroxene, and orthopyroxene with accessory Fe-Ti oxide, zircon, and apatite (Fig. 2a-d). Feldspar comprises more than half of the mode in most samples. Brown to pink pleochroic orthopyroxene is typically the most abundant pyroxene, although in some samples green clinopyroxene is more common. Alignment of mafic phases may define a weak foliation. All phases are anhedral and have curved or irregular grain boundaries, only locally preserving triple junctions between crystals. Brown glass lines plagioclase grain boundaries. Most samples also exhibit a moderate degree of alteration, including mottling of feldspar and yellow or orange alteration rinds along the edges of clinopyroxene crystals (Fig. 2c).

The two other types of gabbroic xenoliths, the garnet-orthopyroxene and the hornblende-bearing granulites, are less common. The garnet-orthopyroxene granulites (LB04-39, LB04-91) consist of 0.5-3mm garnet porphyroblasts or bands in a plagioclase and orthopyroxene matrix (Fig. 2e-f). Feldspar is strongly altered along grain boundaries.

Quartz is also present in the matrix of LB04-39, but only forms irregular, discontinuous bands in LB04-91. Garnet in these samples is commonly embayed and extensively fractured, with rims and fractures usually altered to kelyphite. This is a common feature in lower crustal xenoliths and occurs as a result of decompression melting during the ascent of the xenolith through the crust (Padovani and Carter, 1977). In the hornblende-bearing xenoliths, amphibole occurs as texturally equilibrated crystals in otherwise typical two-pyroxene granulites (LB04-07, LB04-48, and LB04-82; Fig. 2g-h). Hornblende makes up 10-15 percent of the mode of the whole-rock, but is usually concentrated into mm-scale bands. Crystals of all phases are equigranular and anhedral, and feldspar in the hornblende-bearing xenoliths is plagioclase.

LB04-27 is a meta-anorthosite and consists of 80% coarse plagioclase (~3 mm) with garnet and orthopyroxene and accessory spinel, corundum, and ilmenite (Fig. 2i-j). The mafic phases in this xenolith are extensively altered, replaced by fine-grained minerals in veins that crosscut the rock.

4.1.2 Lashaine

Crustal xenoliths from Lashaine have previously been described by Dawson (1977), Jones et al. (1983), and Cohen et al. (1984). The major features of the previously described crustal xenoliths are identical to those described here.

Fourteen xenoliths from Lashaine have been examined in this study (Table 1). Of these, 12 are olivine normative meta-gabbros consisting of plagioclase-clinopyroxene-garnet±orthopyroxene±rutile±kyanite±apatite (Fig. 3a-h). Polygonal plagioclase (35-75%), clinopyroxene (20-40%), and garnet (5-30%) comprise >95% of the mode in most

of these xenoliths, and they will hereafter be referred to as garnet-clinopyroxene granulites. They are similar to the garnet-plagioclase clinopyroxenites described in Jones et al. (1983). Garnet is typically confined to boundaries between plagioclase and clinopyroxene, implying a metamorphic origin. By contrast, plagioclase and clinopyroxene are likely to be igneous, as argued by Jones et al. (1983) and supported by chemical data presented below.

Plagioclase occurs as coarse (0.5-1 mm) polygonal crystals and typically makes up 50 to 75% of the mode; only two samples (89-730 and 89-734) contain <50% plagioclase. Scapolite is present in some samples at triple junctions between plagioclase crystals. Acicular kyanite is common as an inclusion in plagioclase, particularly in samples exhibiting a coronal texture Fig. 3k). In samples with >50% modal plagioclase, garnet-ringed clinopyroxene aggregates form atolls like those described by Jones et al. (1983) (Fig. 3a-d). The structure of these atolls varies with the proportions of major phases in a xenolith. In plagioclase-rich samples (>70% modal plagioclase, including 89-729, 89-731, 89-735), atolls are small, isolated, and take one of three forms: (1) ~2-5 mm aggregates of small, pale green, anhedral clinopyroxene crystal aggregates ringed by garnet or plagioclase-garnet coronae (Fig. 3c-d, right side of image); (2) ~5-10 mm tabular clinopyroxene megacrysts ringed by discontinuous chains of garnet (Fig. 3e-f); or (3) rare ~5 mm aggregates of garnet and plagioclase, which likely represent edges of garnet-plagioclase coronae whose centers lie out of the plane of the thin section (Fig. 3c-d, left side of image). Jones et al. (1983) noted that the pyroxene megacrysts were similar in size to the pyroxene aggregates and suggested that the mafic clusters originated via recrystallization of these megacrysts. As the volume occupied by mafic phases increases

to 40-50%, only mafic atolls of the first type are observed, and these become larger and more interconnected, in some samples defining a plane of foliation. Where acicular kyanite and these strained atolls co-exist, kyanite needles are aligned subparallel to the foliation defined by the mafic phases. By contrast, in samples with only ~30 percent modal plagioclase (89-730 and 89-734), mafic atolls are absent, and the plagioclase, pyroxene, and garnet occur in subequal proportions in a mosaic of ~0.2 mm crystals (Fig. 3g-h).

Biotite occurs rarely as a major phase in xenoliths from Lashaine. Only two biotite granulites (89-733 and 89-745) were found. These xenoliths contain biotite, plagioclase, clinopyroxene, orthopyroxene, garnet, and ilmenite as major phases (Fig. 3i-j). Biotite forms red-brown to semi-opaque crystals up to 1 mm in length. In 89-733, platy mica crystals define a plane of foliation in the sample, whereas in 89-745, biotite is arranged in radiating clusters and no foliation is present. Crystals of most other phases are small (typically ~ 0.1 mm) and anhedral, their size limited by the biotite crystals. Orthopyroxene, however, forms somewhat larger, embayed, and commonly discolored crystals.

All xenoliths from this locality record evidence of decompression mineral breakdown during their ascent from the lower crust, including widespread kelyphitization of garnet and formation of brown glass along the grain boundaries between plagioclase crystals. Clinopyroxenes within the mafic clusters are commonly heavily altered, giving the interior of the clusters a grungy appearance (Fig. 3a).

4.1.3 Naibor Soito

Crustal xenoliths from this locality include both mafic and intermediate granulites. This xenolith suite is markedly different from the suites at Lashaine and Labait, in that it spans a wider compositional range and includes both quartz and alkali feldspar as major phases. Quartz-bearing xenoliths are dominated by anhydrous, felsic domains, but many also contain bands rich in both hydrous and anhydrous mafic phases. Felsic domains consist of coarse, anhedral crystals of plagioclase, quartz, orthopyroxene, and clinopyroxene (Fig. 4a-d). Alkali feldspar is present in some samples, generally those with an intermediate (SiO_2>56 wt%) bulk chemistry. Whereas feldspar and quartz are coarse and anhedral in these domains, pyroxene more commonly forms chains of elongated, irregular crystals along boundaries between felsic phases (Fig. 4c-d).

Mafic domains in the quartz xenoliths consist of plagioclase, pyroxene, hornblende, biotite, garnet, and rare quartz. Hydrous phases are an important component of mafic domains, in contrast to the felsic domains where they are rare or absent. Megacrysts of orthopyroxene (~1 mm) are also present in the mafic domains and are commonly recrystallized along their margins (Fig. 4e-h). Excepting the pyroxene megacrysts, crystals are small (<0.1 mm), and the transition from felsic- to mafic-rich bands is generally marked by a pronounced fining of crystal sizes.

Three Naibor Soito xenoliths studied here are unbanded, lack quartz, and contain abundant pyroxene. Two such quartz-free xenoliths (NS04-61 and NS04-80) exhibit a coronal texture similar to that observed in the Lashaine xenoliths, wherein interconnected, medium-grained pyroxene aggregates are surrounded by rings of metamorphic garnet (Fig. 4i-j). Pyroxene is commonly recrystallized into a fine fabric

similar to that seen in the mafic bands of the quartz granulites. Larger, embayed pyroxene relicts also remain (Fig. 4i-j). One quartz-free xenolith (NS04-150) lacks coronae and is hornblende-rich.

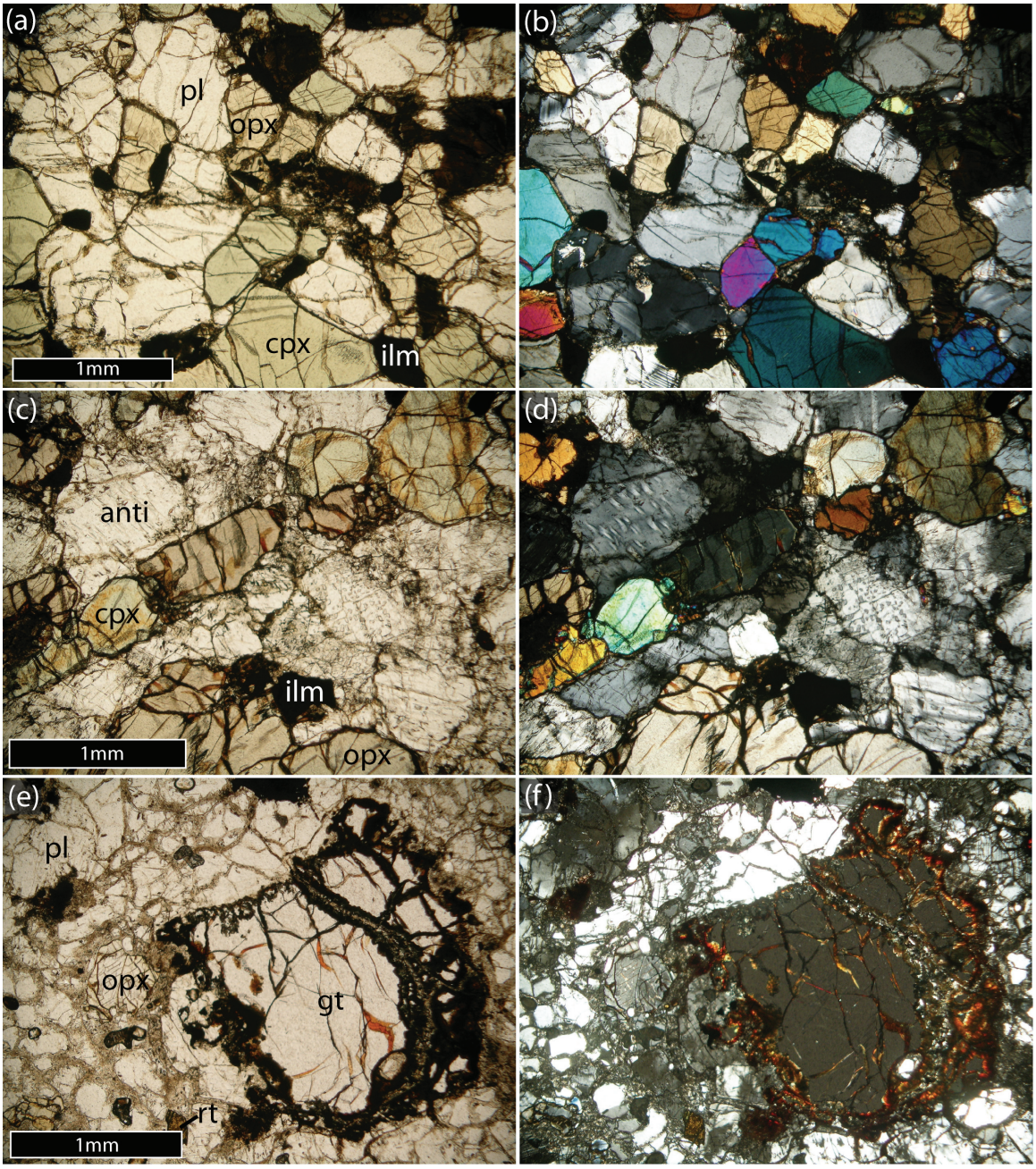

Figure 2. (a) LB04-52, 2px granulite. Plane-polarized light. (b) LB04-52, 2px granulite. Cross-polarized light. (c) LB04-19, 2px granulite. Plane-polarized light. (d) LB04-19, 2px granulite. Cross-polarized light. (e) LB04-39, gt-opx granulite. Plane-polarized light. (f) LB04-39, gt-opx granulite. Cross-polarized light.

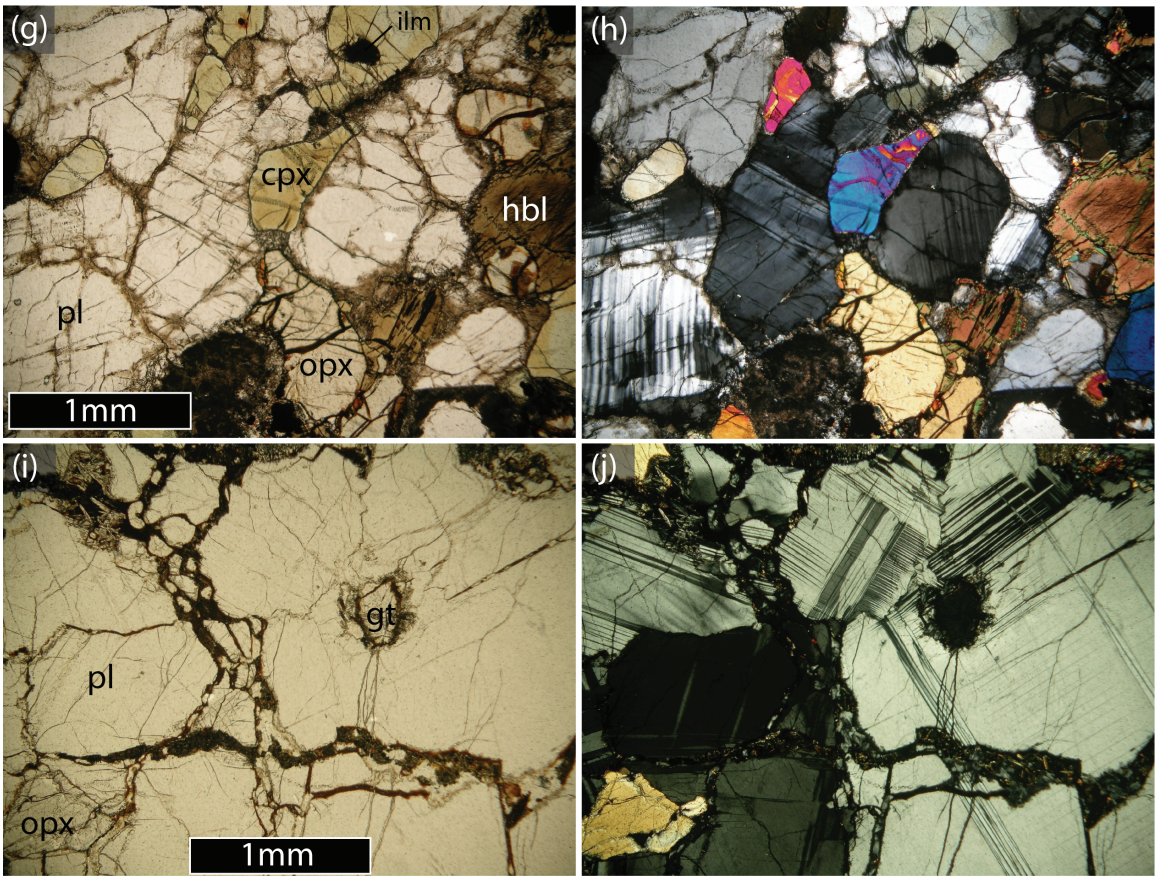

Figure 2 (cont.) (g) LB04-82, 2px-hbl granulite. Plane-polarized light. (h) LB04-82, 2px-hbl granulite. Cross-polarized light. (i) LB04-27, anorthosite. Plane-polarized light. (j) LB04-27, anorthosite. Cross-polarized light.

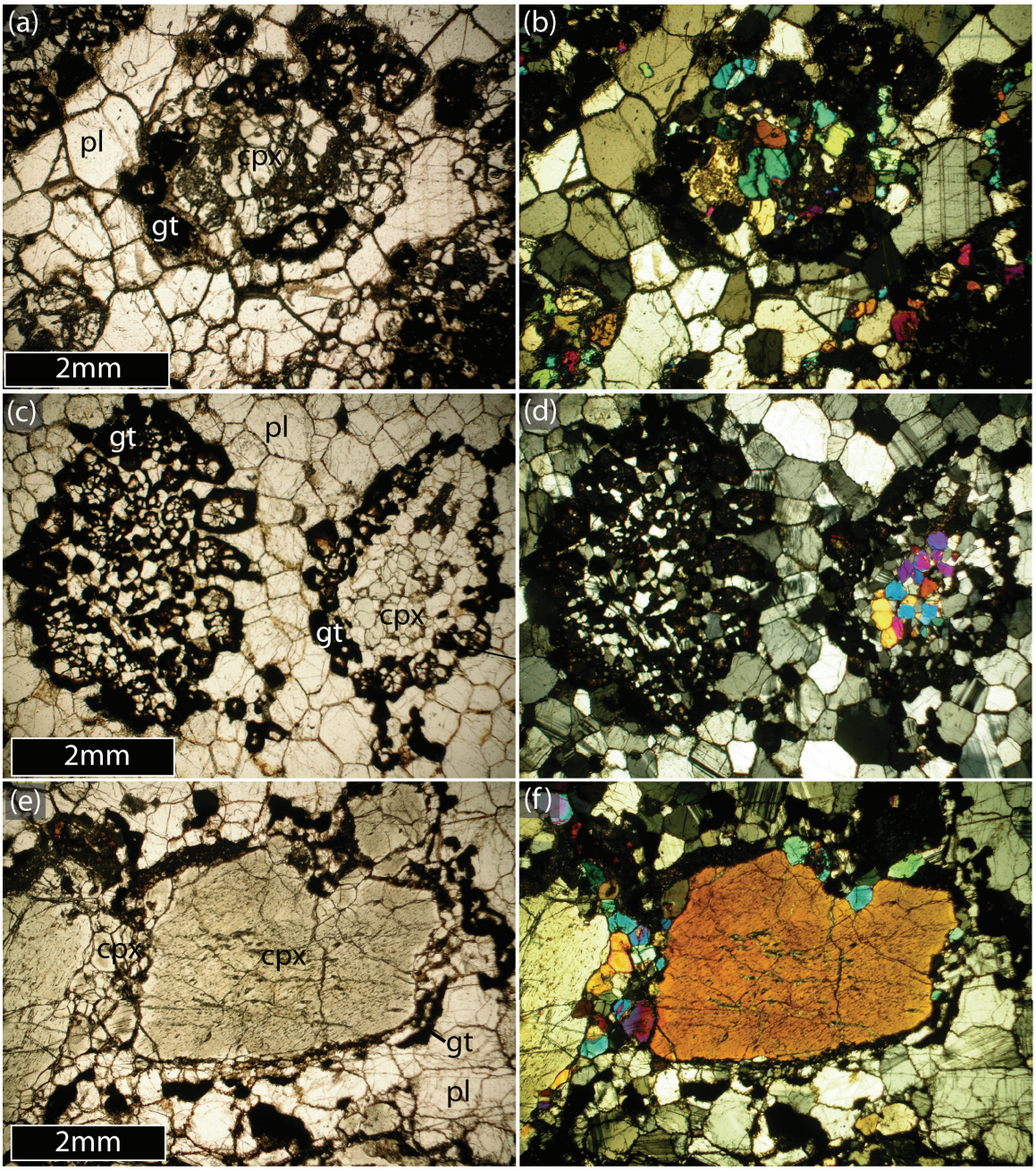

Figure 3. (a) 89-727, gt-cpx granulite with atoll texture. Plane-polarized light. (b) 89-727, gt-cpx granulite with atoll texture. Cross-polarized light. (c) 89-729, gt-cpx granulite with atoll texture. Plane-polarized light. (d) 89-729, gt-cpx granulite with atoll texture. Cross-polarized light. (e) 89-729, gt-cpx granulite with atoll texture. Plane-polarized light. (f) 89-729, gt-cpx granulite with atoll texture. Cross-polarized light.

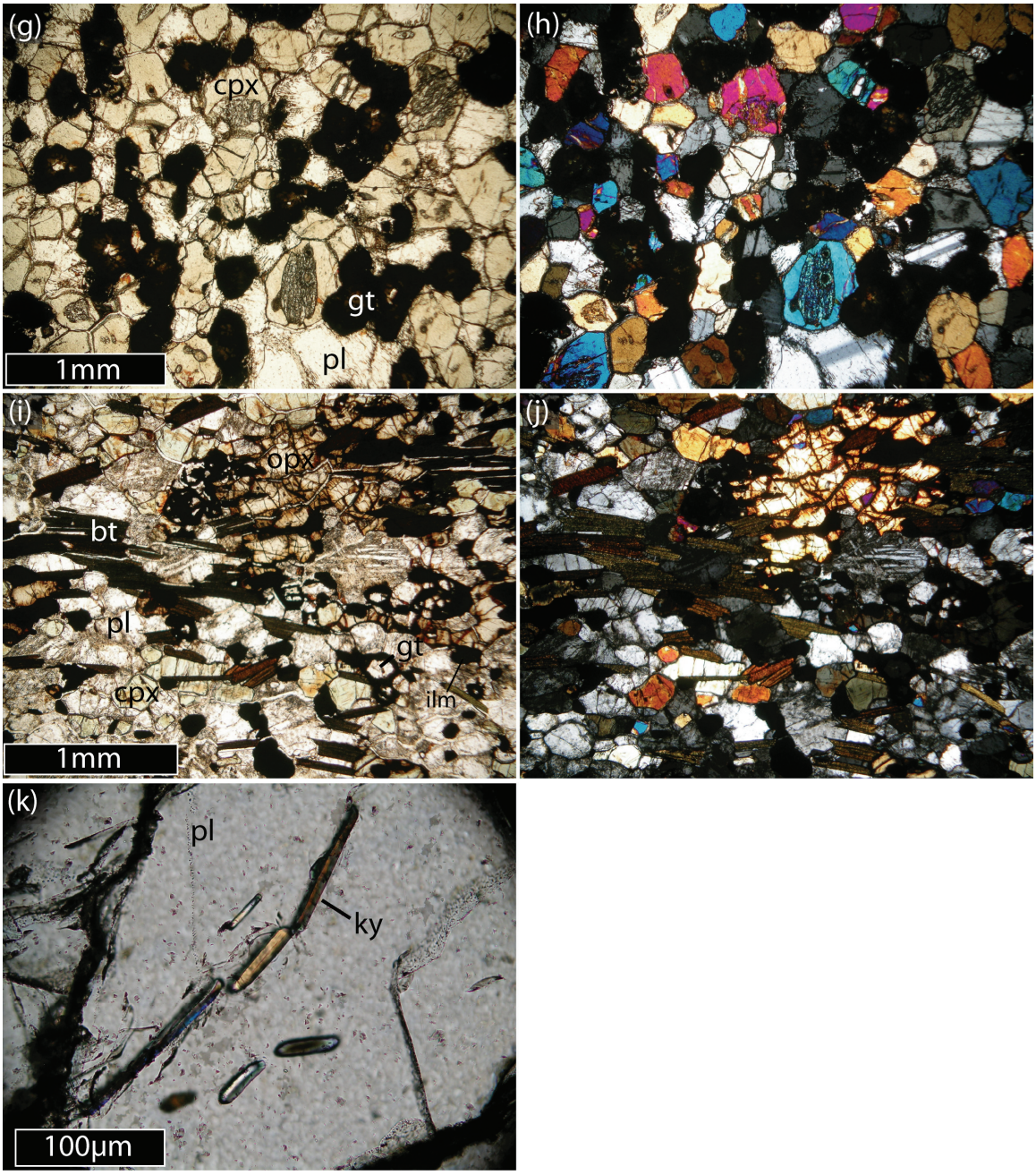

Figure 3 (cont.) (g) 89-730, gt-cpx granulite with mosaic texture. Plane-polarized light. (h) 89-730, gt-cpx granulite with mosaic texture. Cross-polarized light. (i) 89-733, bt granulite. Plane-polarized light. (j) 89-733, bt granulite. Cross-polarized light. (k) 89-727, ky inclusions in pl in gt-cpx granulite with atoll texture. Plane-polarized light.

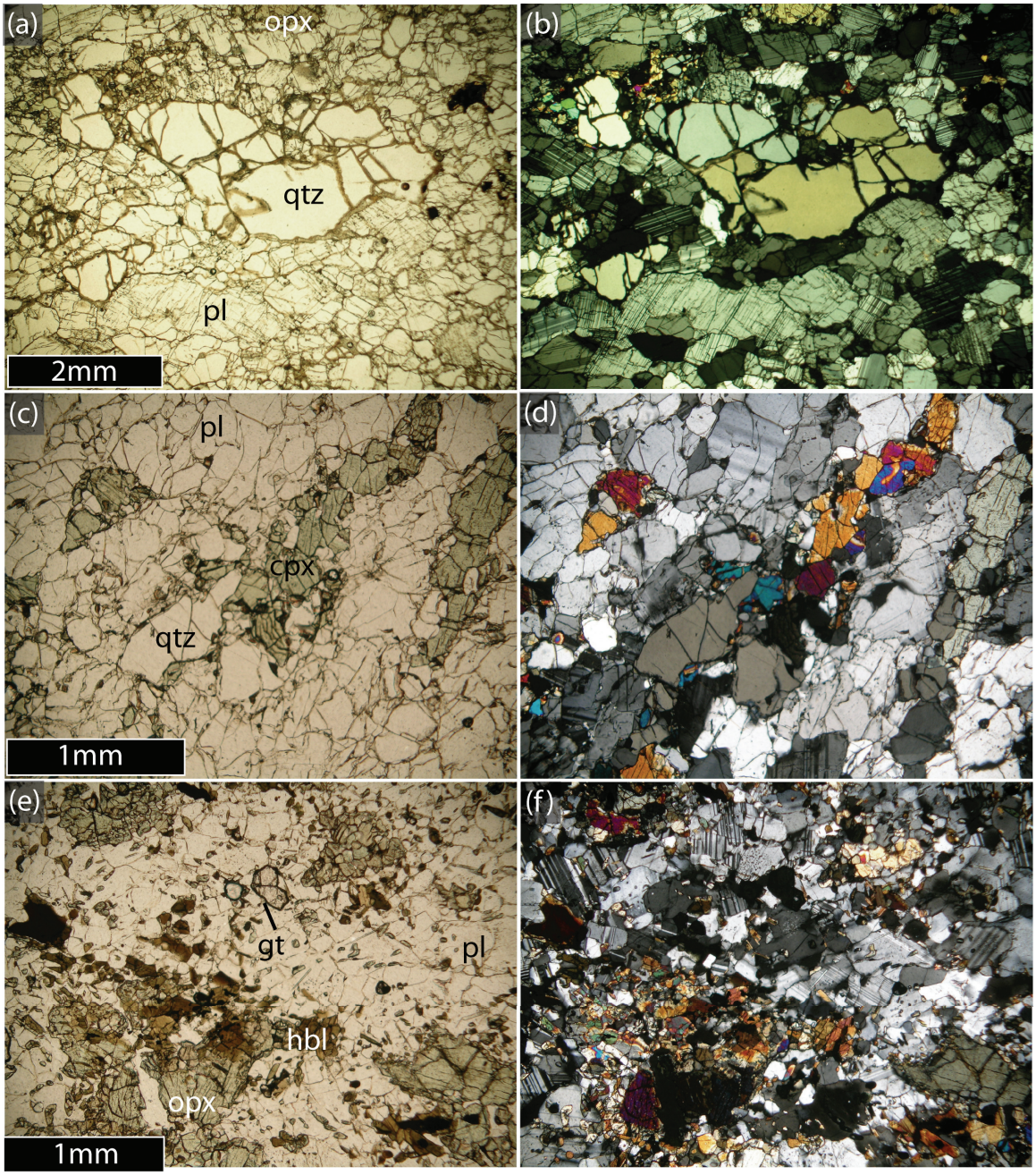

Figure 4. (a) NS04-05, qtz granulite. Plane-polarized light. (b) NS04-05, qtz granulite. Cross-polarized light. (c) NS04-13, qtz granulite. Plane-polarized light. (d) NS04-13, qtz granulite. Cross-polarized light. (e) NS04-13, qtz granulite. Plane-polarized light. (f) NS04-13, qtz granulite. Cross-polarized light.

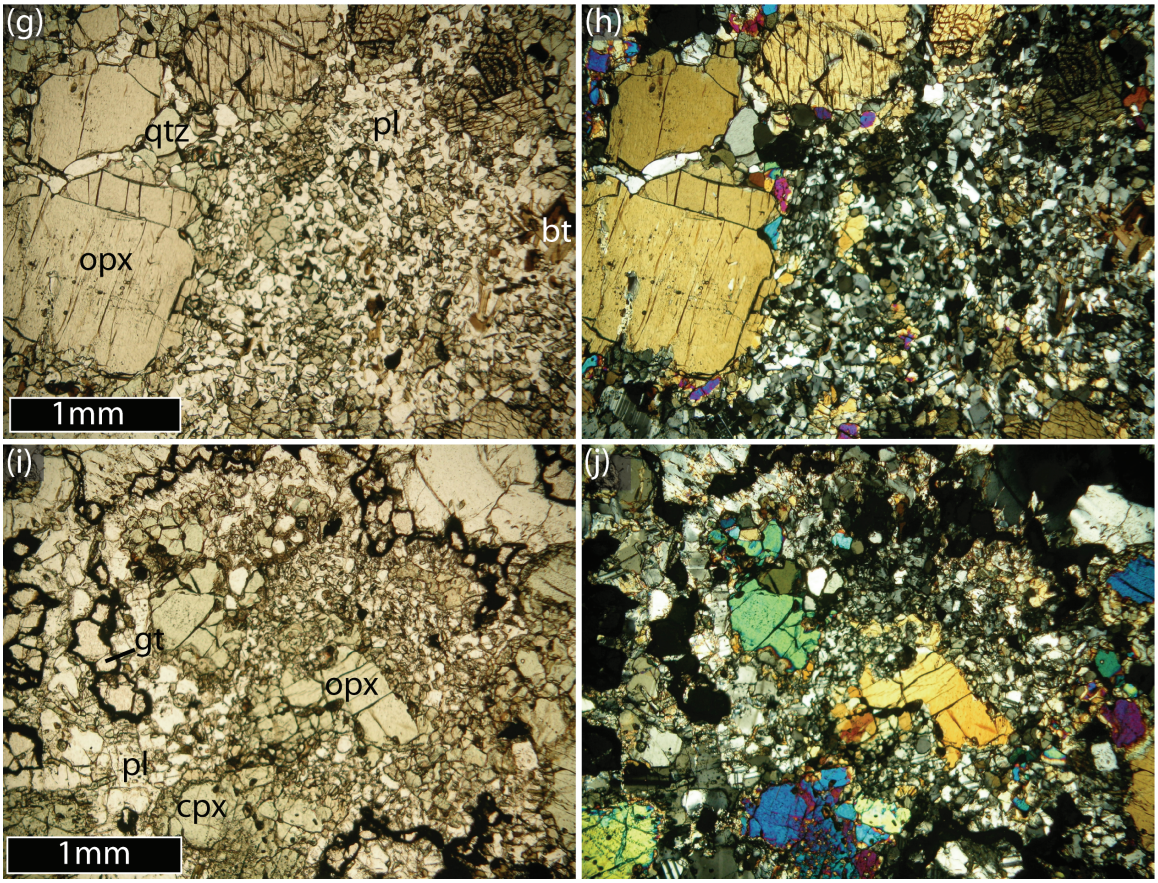

Figure 4 (cont.) (g) NS04-91, qtz granulite. Plane-polarized light. (h) NS04-91, qtz granulite. Cross-polarized light. (i) NS04-80, qtz-free granulite. Plane-polarized light. (j) NS04-80, qtz-free granulite. Cross-polarized light.

4.2 Phase Chemistry

Analytical precision for major element abundances in each phase was established based on the reproducibility of homogenous standard materials measured with samples and is reported in Tables 4-9.

4.3.1 Labait

Feldspar: Feldspar in two-pyroxene granulite xenoliths from Labait consists primarily of antiperthite (Fig. 2c-d). Plagioclase is of the composition $An_{32-55}Ab_{47-64}Or_{0-6}$, whereas lamellae of alkali feldspar are $An_{1-3}Ab_{7-23}Or_{73-91}$ (Tables 4 and 5, Fig. 5). Hornblende-bearing and garnet-orthopyroxene xenoliths typically contain plagioclase in lieu of antiperthite. Plagioclase chemistry is similar to the plagioclase component of antiperthite in the two-pyroxene granulites. Crystals in all samples are unzoned, except in four two-pyroxene granulites where K_2O contents in antiperthite increase from core to rim, and plagioclase compositions are relatively homogenous between samples and types. A key feature of the alkali feldspar lamellae are high BaO contents (0.53-1.75 wt%), which contribute to the extremely high Ba concentrations in these xenoliths.

The anorthosite LB04-27 contains calcic plagioclase ($An_{87-89}Ab_{11-12}$, Fig. 5). This composition is unique among these xenolith suites considered here, but is similar to plagioclase compositions from Archean anorthosite complexes (Ashwal, 1993). No alkali feldspar lamellae are present in this sample.

Pyroxene: Pyroxenes from all localities are classified using the Ca-Fe-Mg and Ca-Na systems described by Morimoto (1988). Clinopyroxenes from Labait are diopsides

or Mg-rich augites of the composition $En_{35-40}Fs_{7-21}Wo_{44-53}$ (Table 6, Fig. 6). Na_2O contents are low (0.49-1.20 wt%), which, along with the lack of garnet in most Labait xenoliths, implies equilibration at a shallower depth than the xenoliths from Lashaine (e.g., Holland, 1980). Clinopyroxene compositions are similar across the suite, with a notable exception being the Al_2O_3-rich, FeO-poor composition of accessory clinopyroxene in garnet-orthopyroxene granulite LB04-39. Two prominent zoning patterns are noted in the Labait clinopyroxenes: (1) in the two-pyroxene xenoliths, rimward zoning to higher FeO and TiO_2 and lower CaO; and (2) in the hornblende-bearing xenoliths, rimward zoning to lower Al_2O_3 and higher CaO. In the two-pyroxene xenoliths, chemical zoning coincides with discoloration along clinopyroxene rims and fractures noted in thin section (Fig. 2c). The significance of these observations is explored in the section on thermobarometry below.

Orthopyroxene in the two-pyroxene (±hornblende) granulites is hypersthene ($En_{52-66}Fs_{34-46}Wo_{0-4}$) (Table 7, Fig. 6). Crystals are unzoned and fairly homogenous throughout the suite, although Al_2O_3 contents range from 1.3-5.9 wt%. Orthopyroxene from garnet-orthopyroxene granulite LB04-39 is MgO-rich relative to the rest of the suite.

Garnet: Only three Labait xenoliths, anorthosite LB04-27 and garnet-orthopyroxene granulites LB04-39 and LB04-91, contain garnet. Garnet compositions were measured in the former two samples. These garnets contain somewhat less FeO and more MgO than those in xenoliths from Lashaine, but have similar, relatively low CaO contents (Table 8, Fig. 7). Notably, garnet in the anorthosite has a higher proportion of CaO relative to that in garnet-orthopyroxene granulite LB04-39. Garnets in both samples

are similar to those from high-pressure granulites or eclogites (Fig. 7).

Hydrous phases: Hornblende occurs as a major phase in LB04-07, LB04-48, and LB04-82, and biotite is a common accessory phase in the Labait xenoliths. Compositions for both phases are consistent with formation at high pressure and temperature (Table 9). Ti concentrations in biotite, for example, tend to increase with metamorphic grade. In rocks where Ti is saturated (i.e., rocks containing minerals in which Ti is an essential structural constituent, for example, rutile and ilmenite), this effect is fairly predictable. Ti concentrations similar to those in the Labait biotites (4.2-4.5 wt%) are typical of granulite-facies metabasites and metapelites (Guidotti, 1984). The significance of F concentrations in hydrous minerals is more ambiguous. Most rocks do not contain minerals with intrinsic F, and F concentrations can therefore vary with both metamorphic grade and sample chemistry. However, F concentrations in hydrous minerals also tend to increase with metamorphic grade, with experiments suggesting that substitution of F for (OH) stabilizes these phases at high pressures and temperatures (Gilbert et al., 1982; Guidotti, 1984). F concentrations in biotites (1.4-1.7 wt%) and hornblendes (0.6-0.8 wt%) from the Labait xenoliths are therefore consistent with (if not diagnostic of) granulite-facies metamorphism.

4.2.2 Lashaine

Feldspar: Plagioclases from Lashaine range from $An_{22-45}Ab_{58-76}Or_{2-5}$ (Table 4, Fig. 5). The anorthite component generally increases from the pyroxene-rich (An_{22-26}) to the plagioclase-rich xenoliths (An_{40}). Plagioclase in the biotite granulite 89-733 has a composition similar to plagioclase in xenoliths with similar proportions of plagioclase

and pyroxene (An_{30}). Pyroxene-rich xenoliths contain the most sodic plagioclase observed in the crustal xenoliths considered in this study (Fig. 5). Most plagioclase crystals are unzoned, save medium-grained crystals associated with the mafic atolls, which are sometimes zoned to higher SiO_2 and Na_2O on their rims. No alkali feldspar was observed in the Lashaine xenoliths.

Pyroxene: Clinopyroxenes in Lashaine xenoliths are sodian diopsides ($En_{38-44}Fs_{7-15}Wo_{46-51}$) (Table 6, Fig. 6). Na_2O concentrations range from 1.2 to 2.4 wt%, corresponding to compositions of $Jd_{6-17}Ae_{0-4}$ using the Ca-Na pyroxene classification scheme in Morimoto (1988). These are the highest Na_2O contents measured in this study, and the values are typical of clinopyroxenes equilibrated at granulite- or eclogite-facies conditions (e.g., Holland, 1980). Clinopyroxenes in most samples are FeO-poor relative to clinopyroxenes from Labait and Naibor Soito, but clinopyroxene in pyroxene-rich xenolith 89-734 has a higher FeO content more typical of this phase in the other suites.

Orthopyroxene is rare at Lashaine and has been recognized in only four xenoliths (89-733, 89-734, 89-742, 89-744) (Table 7, Fig. 6). Crystal compositions are variable and are mostly distinct from orthopyroxene in xenoliths from the other localities. Orthopyroxenes from 89-742 and 89-744 are MgO-rich relative to those from all other xenoliths save the garnet-orthopyroxene granulite LB04-39 from Labait, which has a similar composition. Crystals from pyroxene-rich sample 89-734 fall within the range defined by the Labait and Naibor Soito xenoliths. Orthopyroxene from biotite granulite 89-733 has a FeO-rich composition, comparable to orthopyroxene from the quartz-free granulites from Naibor Soito and consistent with the high Fe content in this xenolith.

Garnet: Garnets in the garnet-clinopyroxene granulites have the composition

$Py_{30-48}Alm_{29-55}Grs_{13-26}$ (Table 8, Fig. 7). Like Labait anorthosite, LB04-27, garnets in most Lashaine xenoliths are CaO-rich. Garnets from pyroxene-rich granulite 89-734 and biotite granulite 89-733 are FeO-rich and Al_2O_3- and CaO-poor relative to those in the rest of the suite, consistent with the bulk chemistry of these samples. Garnet from biotite granulite 89-733 has an especially high FeO-content and plots away from the rest of the suite in Fig. 7. Outside of these two samples, the range of compositions does not correlate with the bulk composition of the xenoliths. Crystals are unzoned, but again have compositions that overlap with eclogitic garnets.

Hydrous phases: Biotite is a major phase in two Lashaine xenoliths (89-733 and 89-745), but was not analyzed for this study. However, the reddish-brown coloration noted in biotite from 89-733 implies that the crystals are Ti-rich (>2.5% TiO_2; Hall, 1941), consistent with partitioning of Ti into biotite at high metamorphic grades (Guidotti, 1984).

4.2.3 Naibor Soito

Feldspar: Plagioclase from Naibor Soito is orthoclase-rich relative to xenoliths from Labait or Lashaine ($An_{25-48}Ab_{50-68}Or_{2-11}$) (Table 4, Fig. 5). The orthoclase component in plagioclase is somewhat higher in intermediate relative to mafic xenoliths, consistent with generally higher whole-rock K_2O contents in xenoliths of intermediate bulk composition. Phase chemistry between samples is otherwise similar. Plagioclase is unzoned, except in NS04-13A and B, in which rims are depleted in K_2O relative to cores (Table 4).

Alkali feldspar ($An_6Ab_{31-34}Or_{60-64}$) has been identified in four samples from this

locality, all intermediate and all containing orthoclase-rich plagioclase (Table 5, Fig. 5). In contrast to alkali feldspar in the Labait xenoliths, this phase forms discrete crystals in Naibor Soito samples. Relative to Labait, alkali feldspar at Naibor Soito contains higher CaO and Na_2O and lower K_2O. BaO contents, however, are similar (0.59-1.26 wt%), though extreme Ba concentrations are not observed at the whole-rock scale.

Pyroxene: Clinopyroxenes from the Naibor Soito xenoliths are mostly augites ($En_{32-38}Fs_{18-26}Wo_{41-45}$) and have higher average FeO contents than samples from the other localities (Table 6, Fig. 6). Compositions are fairly homogenous, and variability does not correlate with bulk sample chemistry. Average Na_2O contents are lower than those measured in both the Labait and Lashaine suites, and crystals are sometimes zoned to higher FeO contents on their rims.

Orthopyroxene compositions overlap for the most part with those from Labait, although those in intermediate xenoliths range to more ferrosilite-rich compositions ($En_{46-61}Fs_{37-54}Wo_{1-3}$) (Table 7, Fig. 6). Compositions do not correlate with sample mineralogy or chemistry. Orthopyroxene TiO_2 and CaO contents are commonly two or more times as abundant in this suite relative to Lashaine and Labait.

Garnet: Garnets from Naibor Soito have a restricted compositional range ($Py_{29-34}Alm_{48-54}Grs_{15-26}$) and plot within a relatively small field on the garnet ternary plot (Table 8, Fig. 7). They are similar to high-pressure garnets from crustal xenoliths from the Kola peninsula (Kempton et al., 1995). Garnet from quartz granulite NS04-53 has a somewhat different composition, containing more FeO but less MgO and CaO. On the whole, garnets from this locality have high contents of FeO and MgO relative to those from Lashaine and Labait. Crystals are unzoned except for MnO, which increases from

core to rim.

Hydrous phases: Both biotite and hornblende are common in mafic domains in the Naibor Soito xenoliths. As in the Labait xenoliths, biotite is Ti-rich (5.2-5.6 wt%), suggesting formation at granulite-facies conditions (Table 9). F concentrations in biotite and hornblende are, however, much lower than might be expected for granulite-facies rocks, though for the reasons described above this does not necessarily imply equilibration at a lower metamorphic grade (Gilbert et al., 1982; Guidotti, 1984).

TABLE 4: Plagioclase feldspar chemistry for Tanzanian granulite xenoliths

	Labait													
	Two-pyroxene granulites													
	LB04-04		LB04-12		LB04-16		LB04-19		LB04-34		LB04-38		LB04-41	
Domain	core	rim	core	rim	core	rim	core	rim	core	rim	core	rim	core	rim
n	5	5	5	5	5	5	5	5	5	5	3	3	5	5
SiO_2	59.7	59.6	56.8	56.1	59.8	59.8	58.5	58.7	58.9	58.8	58.6	58.0	57.4	57.4
Al_2O_3	26.2	26.4	28.0	28.4	25.9	25.7	26.7	27.1	26.7	27.2	27.1	27.1	28.2	28.1
CaO	7.69	7.93	9.83	10.34	7.11	7.04	8.14	8.41	8.06	8.51	8.39	8.56	9.52	9.37
Na_2O	7.10	6.88	5.88	5.63	6.75	6.63	6.13	6.07	6.11	6.04	6.16	5.98	5.59	5.36
K_2O	0.09	0.09	0.32	0.35	0.40	0.64	0.50	0.46	0.63	0.52	0.42	0.47	0.45	1.02
BaO	-	-	0.01	0.01	0.01	0.02	0.01	0.01	0.02	0.02	0.00	0.01	0.01	0.01
Total	100.8	100.8	100.8	100.8	100.0	99.8	100.0	100.8	100.4	101.0	100.7	100.1	101.1	101.2
Si	2.64	2.63	2.53	2.50	2.66	2.67	2.61	2.60	2.62	2.60	2.60	2.59	2.54	2.55
Al	1.37	1.37	1.47	1.50	1.36	1.35	1.40	1.42	1.40	1.42	1.42	1.43	1.47	1.47
Ca	0.36	0.38	0.47	0.49	0.34	0.34	0.39	0.40	0.38	0.40	0.40	0.41	0.45	0.45
Na	0.61	0.59	0.51	0.49	0.58	0.57	0.53	0.52	0.53	0.52	0.53	0.52	0.48	0.46
K	0.01	0.01	0.02	0.02	0.02	0.04	0.03	0.03	0.04	0.03	0.02	0.03	0.03	0.06
Ba	0.00	0.00	0.00	0.00	0.00	0.00	0.00	0.00	0.00	0.00	0.00	0.00	0.00	0.00
An	37	39	47	49	36	36	41	42	41	42	42	43	47	46
Ab	62	61	51	49	62	61	56	55	56	55	56	54	50	48
Or	1	1	2	2	2	4	3	3	4	3	2	3	3	6

Analytical uncertainty (2σ RSD, n > 20): SiO_2 = 2.1%; Al_2O_3 =2.0%; CaO = 5.4%; Na_2O = 10%; K_2O = 2.7%; BaO ~ 220%

TABLE 4: Plagioclase feldspar chemistry for Tanzanian granulite xenoliths (cont.)

	Labait												
	Two-pyroxene granulites									Gt-opx gran		2px-hbl gran	
	LB04-50		LB04-52		LB04-53		LB04-93		LB-48	LB04-39		LB04-07	
Domain	core	rim	core	rim	core	rim	core	rim	mean	core	rim	core	rim
n	5	5	5	4	5	5	5	5	14	5	5	5	5
SiO_2	61.0	60.8	58.9	58.6	60.4	60.2	59.2	58.8	59.0	58.5	59.4	56.2	56.4
Al_2O_3	25.5	25.3	26.8	27.2	25.9	26.2	26.7	26.6	26.1	26.9	26.3	28.9	28.9
CaO	6.61	6.51	8.21	8.44	7.08	7.40	8.11	8.32	7.80	8.03	7.91	10.7	10.8
Na_2O	7.15	6.99	6.15	6.11	6.81	6.69	6.71	6.26	6.47	6.92	6.92	5.53	5.43
K_2O	0.51	0.79	0.49	0.43	0.32	0.40	0.40	0.84	0.54	0.29	0.33	0.27	0.30
BaO	0.01	0.01	0.01	0.01	0.00	0.01	0.01	0.03	-	-	-	-	-
Total	100.7	100.4	100.6	100.7	100.6	100.9	101.0	100.9	99.9	100.6	100.9	101.6	101.9
Si	2.69	2.69	2.61	2.60	2.67	2.65	2.62	2.61	2.64	2.60	2.63	2.49	2.49
Al	1.32	1.32	1.40	1.42	1.35	1.36	1.39	1.39	1.37	1.41	1.37	1.51	1.51
Ca	0.31	0.31	0.39	0.40	0.33	0.35	0.38	0.40	0.37	0.38	0.37	0.51	0.51
Na	0.61	0.60	0.53	0.53	0.58	0.57	0.58	0.54	0.56	0.60	0.59	0.48	0.47
K	0.03	0.04	0.03	0.02	0.02	0.02	0.02	0.05	0.03	0.02	0.02	0.02	0.02
Ba	0.00	0.00	0.00	0.00	0.00	0.00	0.00	0.00	0.00	0.00	0.00	0.00	0.00
An	33	32	41	42	36	37	39	40	39	38	38	51	52
Ab	64	63	56	55	62	61	59	55	58	60	60	48	47
Or	3	5	3	3	2	2	2	5	3	2	2	2	2

TABLE 4: Plagioclase feldspar chemistry for Tanzanian granulite xenoliths (cont.)

	Labait						Lashaine							
	2px-hbl granulites				Anorthosite		Garnet-clinopyroxene granulites							
	LB04-48		LB04-82		LB04-27		89-726	89-727						89-730
Domain	core	rim	core	rim	core	rim	matrix	matrix		outside corona		inside corona		matrix
								core	rim	core	rim	core	rim	
n	5	5	5	5	5	5	5	5					4	
SiO_2	57.5	57.3	58.7	58.0	46.6	46.3	58.3	60.7	59.7	60.6	61.1	60.4	60.8	62.0
Al_2O_3	27.4	27.9	27.4	26.3	35.7	36.0	26.3	25.4	26.1	25.5	25.1	24.6	24.5	23.8
CaO	9.23	9.63	8.91	8.86	18.0	18.3	8.30	6.78	7.28	6.77	6.36	6.17	6.33	5.38
Na_2O	6.15	6.00	6.60	6.40	1.43	1.25	6.55	7.16	6.90	7.17	7.33	7.15	7.04	8.04
K_2O	0.42	0.50	0.07	0.08	0.04	0.06	0.34	0.49	0.49	0.49	0.58	0.61	0.60	0.68
BaO	0.02	0.02	-	-	-	-	-	-	-	-	-	-	-	
Total	100.8	101.4	101.7	99.6	101.8	101.9	99.7	100.6	100.4	100.5	100.5	99.0	99.3	99.9
Si	2.56	2.54	2.58	2.60	2.11	2.09	2.61	2.69	2.65	2.68	2.70	2.71	2.72	2.76
Al	1.44	1.46	1.42	1.39	1.90	1.92	1.39	1.32	1.36	1.33	1.31	1.30	1.29	1.25
Ca	0.44	0.46	0.42	0.43	0.87	0.89	0.40	0.32	0.35	0.32	0.30	0.30	0.30	0.26
Na	0.53	0.52	0.56	0.56	0.12	0.11	0.57	0.61	0.59	0.62	0.63	0.62	0.61	0.69
K	0.02	0.03	0.00	0.00	0.00	0.00	0.02	0.03	0.03	0.03	0.03	0.03	0.03	0.04
Ba	0.00	0.00	0.00	0.00	0.00	0.00	0.00	0.00	0.00	0.00	0.00	0.00	0.00	0.00
An	44	46	43	43	87	89	40	33	36	33	31	31	32	26
Ab	53	52	57	56	12	11	58	64	61	64	65	65	64	70
Or	2	3	0	0	0	0	2	3	3	3	3	4	4	4

TABLE 4: Plagioclase feldspar chemistry for Tanzanian granulite xenoliths (cont.)

	Lashaine												
	Garnet-clinopyroxene granulites												
	89-731	89-734		89-739						89-742			
Domain	matrix	matrix		matrix		outside corona		inside corona		matrix		outside corona	
		core	rim	core	rim	core	rim	core	rim	core	rim	core	rim
n	5	4	4	4	4	4	4	4	3	5	3	5	4
SiO_2	57.6	63.8	63.5	61.6	60.8	62.7	61.8	62.7	59.2	61.1	60.1	62.6	59.3
Al_2O_3	26.9	23.2	23.7	24.5	25.4	24.1	24.5	23.8	24.5	25.2	25.2	24.5	25.5
CaO	9.09	4.43	4.86	5.77	6.21	5.32	5.78	5.22	6.56	6.49	6.76	5.60	7.68
Na_2O	5.97	8.53	8.27	7.68	7.46	7.95	7.71	7.88	6.67	7.29	6.89	7.93	6.66
K_2O	0.29	0.37	0.40	0.51	0.48	0.56	0.47	0.56	0.50	0.46	0.92	0.55	0.48
BaO	-	-	-	-	-	-	-	-	-		-	-	-
Total	99.9	100.3	100.7	100.1	100.3	100.7	100.2	100.2	97.5	100.6	100.0	101.2	99.7
Si	2.58	2.81	2.79	2.73	2.69	2.76	2.73	2.77	2.70	2.70	2.68	2.74	2.66
Al	1.42	1.20	1.22	1.28	1.32	1.25	1.28	1.24	1.32	1.31	1.33	1.27	1.35
Ca	0.44	0.21	0.23	0.27	0.29	0.25	0.27	0.25	0.32	0.31	0.32	0.26	0.37
Na	0.52	0.73	0.70	0.66	0.64	0.68	0.66	0.67	0.59	0.62	0.60	0.67	0.58
K	0.02	0.02	0.02	0.03	0.03	0.03	0.03	0.03	0.03	0.03	0.05	0.03	0.03
Ba	0.00	0.00	0.00	0.00	0.00	0.00	0.00	0.00	0.00	0.00	0.00	0.00	0.00
An	45	22	24	28	31	26	28	26	34	32	33	27	38
Ab	53	76	74	69	67	71	69	71	63	65	61	70	59
Or	2	2	2	3	3	3	3	3	3	3	5	3	3

TABLE 4: Plagioclase feldspar chemistry for Tanzanian granulite xenoliths (cont.)

	Lashaine			Naibor Soito									
	Gt-cpx gran		Bt gran	Quartz granulites									
	89-742		89-733	NS04-13A		NS04-13B		NS04-53		NS04-91		NS04-93	
Domain	inside corona			core	rim	core	rim	core	rim	core	rim	core	rim
	core	rim											
n	5	4		5	5	5	5	5	5	5	5	5	5
SiO_2	62.2	61.5	61.6	62.0	61.6	60.4	58.8	61.8	62.1	60.0	59.5	60.3	58.4
Al_2O_3	24.3	24.5	24.2	23.8	24.3	25.3	26.2	23.6	23.9	25.5	26.0	25.8	27.0
CaO	5.62	6.02	6.06	5.26	5.79	6.78	7.99	4.93	5.17	7.07	7.51	7.06	8.50
Na_2O	7.89	7.49	7.51	6.73	6.69	6.44	5.98	6.84	6.81	6.30	6.08	6.62	5.95
K_2O	0.53	0.46	0.52	1.71	1.46	1.29	0.98	1.86	1.75	1.12	1.02	0.74	0.57
BaO	-	-	-	0.10	0.09	0.01	0.02	0.03	0.05	0.04	0.03	0.03	0.03
Total	100.6	100.0	99.9	99.5	99.8	100.2	100.0	99.1	99.7	100.0	100.1	100.6	100.5
Si	2.74	2.73	2.74	2.76	2.74	2.69	2.63	2.77	2.76	2.67	2.65	2.67	2.60
Al	1.26	1.28	1.27	1.25	1.27	1.33	1.38	1.25	1.26	1.34	1.36	1.35	1.42
Ca	0.27	0.29	0.29	0.25	0.28	0.32	0.38	0.24	0.25	0.34	0.36	0.33	0.41
Na	0.67	0.64	0.65	0.58	0.58	0.56	0.52	0.59	0.59	0.54	0.53	0.57	0.51
K	0.03	0.03	0.03	0.10	0.08	0.07	0.06	0.11	0.10	0.06	0.06	0.04	0.03
Ba	0.00	0.00	0.00	0.00	0.00	0.00	0.00	0.00	0.00	0.00	0.00	0.00	0.00
An	27	30	30	27	30	34	40	25	26	36	38	35	43
Ab	70	67	67	63	62	58	54	63	63	58	56	60	54
Or	3	3	3	10	9	8	6	11	11	7	6	4	3

TABLE 4: Plagioclase feldspar chemistry for Tanzanian granulite xenoliths (cont.)

	Naibor Soito									
	Quartz granulites					Quartz-free xenoliths				
	NS04-96		NS04-104		W3S-2	NS04-61		NS04-80		
Domain	core	rim	core	rim	mean	core	rim	core	rim	corona
n	5	5	5	5	15	5	5	5	5	4
SiO_2	62.5	61.9	61.2	60.5	61.2	58.2	57.3	58.6	57.3	57.5
Al_2O_3	24.3	24.4	24.6	25.0	24.3	25.9	26.6	26.6	27.7	27.3
CaO	5.51	5.73	6.05	6.54	6.03	7.94	8.73	8.37	9.59	9.09
Na_2O	7.37	7.23	6.51	6.35	6.85	5.84	5.61	6.10	5.47	5.73
K_2O	0.74	0.71	1.48	1.35	1.43	1.03	0.87	0.46	0.37	0.41
BaO	0.05	0.05	0.07	0.09	-	0.02	0.02	0.01	0.01	0.01
Total	100.4	100.0	99.9	99.7	99.8	98.9	99.1	100.2	100.5	100.1
Si	2.75	2.74	2.72	2.70	2.73	2.63	2.59	2.61	2.56	2.57
Al	1.26	1.27	1.29	1.31	1.28	1.38	1.42	1.40	1.46	1.44
Ca	0.26	0.27	0.29	0.31	0.29	0.38	0.42	0.40	0.46	0.44
Na	0.63	0.62	0.56	0.55	0.59	0.51	0.49	0.53	0.47	0.50
K	0.04	0.04	0.08	0.08	0.08	0.06	0.05	0.03	0.02	0.02
Ba	0.00	0.00	0.00	0.00	0.00	0.00	0.00	0.00	0.00	0.00
An	28	29	31	33	30	40	44	42	48	46
Ab	68	67	60	58	62	54	51	55	50	52
Or	4	4	9	8	8	6	5	3	2	2

TABLE 5: Alkali feldspar chemistry for Tanzanian granulite xenoliths

	Labait							
	Two-pyroxene granulites							
	LB04-12	LB04-16	LB04-19	LB04-34	LB04-38	LB04-41	LB04-50	LB04-52
SiO_2	65.2	64.8	63.3	64.2	63.6	63.6	64.4	64.4
Al_2O_3	19.5	19.2	19.0	19.4	19.5	19.1	19.1	19.2
CaO	0.19	0.07	0.22	0.14	0.25	0.25	0.11	0.08
Na_2O	2.29	1.89	1.95	1.77	2.40	0.71	1.43	1.34
K_2O	12.3	13.3	12.6	13.1	11.8	14.7	13.9	13.9
BaO	1.29	0.53	0.95	0.84	1.20	0.89	0.70	0.81
Total	100.8	99.8	98.1	99.4	98.7	99.3	99.7	99.8
Si	2.97	2.98	2.96	2.97	2.95	2.96	2.97	2.97
Al	1.05	1.04	1.05	1.05	1.07	1.05	1.04	1.05
Ca	0.01	0.00	0.01	0.01	0.01	0.01	0.01	0.00
Na	0.10	0.08	0.09	0.08	0.11	0.03	0.06	0.06
K	0.36	0.39	0.38	0.39	0.35	0.44	0.41	0.41
Ba	0.02	0.01	0.02	0.02	0.02	0.02	0.01	0.01
An	2	1	2	2	3	3	1	1
Ab	22	18	19	17	23	7	13	13
Or	76	82	79	82	74	91	85	87

Analytical uncertainty (2σ RSD wt%, n > 20): SiO_2 = 2.8%; Al_2O_3 = 2.1%; CaO = 5.4%; Na_2O = 10%; K_2O = 2.7%; BaO = 75%

TABLE 5: Alkali feldspar chemistry for Tanzanian granulite xenoliths (cont.)

	Labait				Naibor Soito			
	2px gran			2px-hbl	Qtz granulites			
	LB04-53	LB04-93	LB-48	LB04-48	NS04-13	NS04-53	NS04-104	W3S-2
SiO_2	64.3	65.3	64.1	65.0	65.3	65.4	64.9	65.7
Al_2O_3	19.2	19.8	19.4	19.8	19.5	19.5	19.7	19.2
CaO	0.06	0.32	0.35	0.18	0.60	0.58	0.61	0.54
Na_2O	1.38	1.51	2.37	2.17	3.62	3.49	3.35	3.32
K_2O	13.9	13.4	11.5	12.5	9.85	10.2	10.2	10.5
BaO	0.74	0.99	-	1.75	1.20	0.90	1.26	-
Total	99.6	101.4	97.8	101.5	100.1	100.1	100.0	99.3
Si	2.97	2.96	2.97	2.95	2.97	2.97	2.96	2.99
Al	1.05	1.06	1.06	1.06	1.05	1.04	1.06	1.03
Ca	0.00	0.02	0.02	0.01	0.03	0.03	0.03	0.03
Na	0.06	0.07	0.11	0.10	0.16	0.15	0.15	0.15
K	0.41	0.39	0.34	0.36	0.29	0.29	0.30	0.31
Ba	0.01	0.02	0.00	0.03	0.02	0.02	0.02	0.00
An	1	3	4	2	6	6	6	6
Ab	13	14	23	21	34	32	31	31
Or	86	83	73	78	60	62	62	64

TABLE 6: Clinopyroxene chemistry for Tanzanian granulite xenoliths

	Labait																			
	Two-pyroxene granulites																			
	LB04-04		LB04-12		LB04-16		LB04-19		LB04-34		LB04-38		LB04-41		LB04-50		LB04-52		LB04-53	
Domain	core	rim	core	rim	core	rim	core	rim	core	rim	core	rim	core	rim	core	rim	core	rim	core	rim
n	5	5	5	5	5	5	5	5	5	5	5	5	5	5	5	5	5	5	5	5
SiO_2	52.0	52.4	50.7	51.1	51.1	51.7	51.0	50.8	51.1	50.9	50.3	50.4	49.8	50.5	51.7	51.7	51.5	51.8	51.9	52.3
TiO_2	0.26	0.20	0.47	0.40	0.36	0.24	0.43	0.41	0.57	0.43	0.68	0.52	0.76	0.61	0.32	0.25	0.36	0.33	0.38	0.32
Al_2O_3	2.41	1.98	5.39	5.48	3.86	3.30	4.35	4.69	4.38	4.72	6.03	5.87	6.86	6.34	3.47	3.52	4.42	4.15	4.13	4.07
FeO	12.7	10.9	10.9	9.19	11.1	9.92	9.49	8.46	9.03	8.49	9.14	7.95	8.17	7.59	11.1	10.1	8.98	7.79	9.18	8.06
MnO	0.38	0.34	0.19	0.17	0.07	0.08	0.05	0.03	0.03	0.03	0.04	0.04	0.05	0.05	0.06	0.07	0.04	0.05	0.02	0.04
MgO	12.2	12.6	11.9	11.9	11.7	12.1	12.3	12.2	12.2	12.3	12.0	12.0	11.7	12.3	11.7	12.1	12.3	12.7	12.4	12.8
CaO	21.2	22.6	21.5	23.0	21.6	22.6	21.7	22.7	22.1	22.5	21.4	22.8	22.4	22.6	21.9	22.6	22.3	23.1	22.3	22.9
Na_2O	0.58	0.49	0.95	0.92	0.94	0.90	0.96	0.95	0.96	0.92	1.05	0.99	1.20	0.87	0.96	0.88	0.97	0.93	1.12	1.03
Total	101.8	101.5	102.0	102.1	100.8	100.8	100.3	100.2	100.4	100.3	100.6	100.6	100.9	100.9	101.2	101.2	100.8	100.8	101.3	101.4
Si	1.94	1.95	1.87	1.87	1.91	1.93	1.90	1.89	1.90	1.89	1.87	1.87	1.84	1.86	1.92	1.92	1.91	1.91	1.91	1.92
Ti	0.01	0.01	0.01	0.01	0.01	0.01	0.01	0.01	0.02	0.01	0.02	0.01	0.02	0.02	0.01	0.01	0.01	0.01	0.01	0.01
Al^{IV}	0.06	0.05	0.13	0.13	0.09	0.07	0.10	0.11	0.10	0.11	0.13	0.13	0.16	0.14	0.08	0.08	0.09	0.09	0.09	0.08
Al^{VI}	0.04	0.03	0.11	0.11	0.08	0.07	0.09	0.10	0.09	0.10	0.13	0.12	0.14	0.14	0.08	0.07	0.10	0.09	0.09	0.09
Fe^{2+}	0.33	0.28	0.24	0.19	0.26	0.23	0.22	0.19	0.22	0.20	0.22	0.17	0.16	0.19	0.27	0.23	0.21	0.17	0.20	0.18
Fe^{3+}	0.07	0.06	0.10	0.09	0.08	0.08	0.07	0.08	0.06	0.07	0.06	0.08	0.10	0.05	0.08	0.08	0.07	0.07	0.08	0.07
Mn	0.01	0.01	0.01	0.01	0.00	0.00	0.00	0.00	0.00	0.00	0.00	0.00	0.00	0.00	0.00	0.00	0.00	0.00	0.00	0.00
Mg	0.68	0.70	0.66	0.65	0.65	0.67	0.68	0.68	0.68	0.68	0.66	0.66	0.65	0.68	0.65	0.67	0.68	0.70	0.68	0.70
Ca	0.85	0.90	0.85	0.90	0.87	0.90	0.87	0.90	0.88	0.90	0.85	0.90	0.89	0.89	0.87	0.90	0.89	0.91	0.88	0.90
Na	0.04	0.03	0.07	0.07	0.07	0.06	0.07	0.07	0.07	0.07	0.08	0.07	0.09	0.06	0.07	0.06	0.07	0.07	0.08	0.07
En	35	36	36	35	35	36	37	37	37	37	37	37	36	38	35	35	37	38	37	38
Fs	21	18	19	16	19	17	16	14	15	14	16	14	14	13	19	17	15	13	15	13
Wo	44	46	46	49	46	48	47	49	48	49	47	50	50	49	47	48	48	49	48	49

Analytical uncertainty (2σ RSD, n > 12): SiO_2 = 2.3%; TiO2 = 8.5%; Al_2O_3 = 3.9%; FeO = 4.1%; MnO ~150%; MgO = 2.2%; CaO = 2.7%; Na_2O = 13.1%

TABLE 6: Clinopyroxene chemistry for Tanzanian granulite xenoliths (cont.)

	Labait												Lashaine							
	2px gran				Gt-opx gran		Two-pyroxene-hornblende granulites						Garnet-clinopyroxene granulites							
	LB04-93		LB-48		LB04-39		LB04-07		LB04-48		LB04-82		89-727		89-729	89-730	89-731	89-734	89-739	
Domain	core	rim	core	rim	core	rim	core	rim	core	rim	core	rim	core	rim					core	rim
n	5	5	5	5	5	5	5	5	5	5	5	5	5	5					5	5
SiO_2	51.7	52.4	50.6	50.8	49.7	51.1	51.8	51.5	51.7	50.1	51.1	51.6	52.4	52.6	52.2	51.6	51.3	52.4	52.9	52.8
TiO_2	0.43	0.37	0.38	0.35	0.67	0.64	0.40	0.51	0.41	0.53	0.49	0.34	0.53	0.53	0.44	0.48	0.28	0.23	0.46	0.46
Al_2O_3	4.07	4.42	4.33	4.23	9.97	7.21	3.81	4.92	4.31	5.93	4.95	4.43	8.29	8.03	7.29	7.56	4.92	3.16	6.85	7.61
FeO	10.4	8.05	9.25	8.60	4.56	4.05	10.4	10.1	10.1	9.79	9.74	9.19	4.09	3.99	5.86	5.93	6.12	8.59	4.58	4.52
MnO	0.04	0.02	0.19	0.18	0.01	0.00	0.08	0.07	0.22	0.18	0.27	0.26	0.01	0.02	-	-	-	-	0.00	0.01
MgO	12.8	12.6	12.7	12.7	12.4	13.5	12.3	12.7	12.2	12.6	12.0	12.4	13.0	13.2	11.7	11.6	12.6	12.9	13.3	13.1
CaO	21.1	22.9	21.0	21.9	24.0	24.5	22.5	20.5	22.5	21.1	22.2	22.4	20.7	20.7	20.1	20.3	23.3	21.2	20.5	20.0
Na_2O	0.87	0.91	0.97	0.95	0.88	0.79	0.60	0.72	0.80	0.93	1.02	0.97	1.92	1.93	2.31	2.37	1.22	1.42	1.91	2.17
Total	101.4	101.7	99.4	99.7	102.3	101.8	101.9	101.1	102.2	101.2	101.8	101.5	100.9	101.0	99.9	99.8	99.7	99.9	100.5	100.7
Si	1.91	1.92	1.90	1.90	1.79	1.84	1.91	1.90	1.90	1.85	1.88	1.90	1.85	1.89	1.88	1.87	1.88	1.92	1.91	1.90
Ti	0.01	0.01	0.01	0.01	0.02	0.02	0.01	0.01	0.01	0.01	0.01	0.01	0.01	0.01	0.01	0.01	0.01	0.01	0.01	0.01
Al^{IV}	0.09	0.08	0.10	0.10	0.21	0.16	0.09	0.10	0.10	0.15	0.12	0.10	0.15	0.11	0.12	0.13	0.12	0.08	0.09	0.10
Al^{VI}	0.09	0.11	0.09	0.09	0.21	0.15	0.07	0.11	0.09	0.11	0.10	0.09	0.20	0.22	0.19	0.19	0.09	0.06	0.20	0.22
Fe^{2+}	0.25	0.21	0.21	0.18	0.09	0.08	0.26	0.30	0.24	0.20	0.20	0.20	0.12	0.12	0.18	0.18	0.19	0.26	0.14	0.13
Fe^{3+}	0.07	0.03	0.08	0.09	0.05	0.04	0.06	0.01	0.07	0.11	0.10	0.08	0.00	0.00	0.00	0.00	0.00	0.00	0.00	0.00
Mn	0.00	0.00	0.01	0.01	0.00	0.00	0.00	0.00	0.01	0.01	0.01	0.01	0.00	0.00	0.00	0.00	0.00	0.00	0.00	0.00
Mg	0.71	0.69	0.71	0.71	0.67	0.72	0.68	0.70	0.67	0.70	0.66	0.68	0.69	0.71	0.63	0.62	0.68	0.71	0.72	0.70
Ca	0.84	0.90	0.85	0.88	0.92	0.95	0.89	0.81	0.89	0.84	0.88	0.88	0.78	0.80	0.78	0.79	0.91	0.83	0.79	0.77
Na	0.06	0.06	0.07	0.07	0.06	0.06	0.04	0.05	0.06	0.07	0.07	0.07	0.13	0.13	0.16	0.17	0.09	0.10	0.13	0.15
En	38	38	38	38	39	40	36	38	36	38	36	37	43	44	40	39	38	39	44	44
Fs	17	13	16	15	8	7	17	17	17	17	17	16	8	7	11	11	10	15	8	8
Wo	45	49	46	47	53	53	47	44	47	45	48	48	49	49	49	49	51	46	48	48

TABLE 6: Clinopyroxene chemistry for Tanzanian granulite xenoliths (cont.)

	Lashaine			Naibor Soito																	
	Gt-cpx gran			Quartz xenoliths															Quartz-free xenoliths			
	89-741	89-742		89-744	NS04-13A		NS04-13B		NS04-91		NS04-93		NS04-96		NS04-104		W3S-2		NS04-61		NS04-80	
Domain		core	rim		core	rim	core	rim	core	rim	core	rim	core	rim	core	rim	core	rim	core	rim	core	rim
n		5	5		5	5	5	5	5	5	5	5	5	5	5	5	5	5	5	5	5	5
SiO_2	52.9	52.4	52.3	52.5	51.1	51.0	50.8	50.5	51.3	51.2	50.7	50.5	50.8	50.8	50.0	50.4	50.0	50.5	50.8	50.6	50.8	50.9
TiO_2	0.31	0.52	0.49	0.38	0.29	0.30	0.28	0.26	0.28	0.29	0.33	0.33	0.31	0.28	0.31	0.27	0.32	0.26	0.29	0.31	0.36	0.31
Al_2O_3	4.90	7.78	7.56	7.34	2.89	2.76	4.00	3.59	3.60	3.23	4.52	4.30	2.96	2.87	3.42	3.01	3.93	3.30	3.81	3.56	4.46	3.69
FeO	6.25	4.55	4.62	5.10	13.1	12.8	11.7	12.8	10.9	11.4	11.6	12.8	14.2	14.6	14.8	14.9	14.4	14.5	11.5	13.2	10.6	11.0
MnO	-	0.04	0.02	-	0.23	0.25	0.26	0.31	0.23	0.23	0.16	0.21	0.40	0.36	0.49	0.49	0.48	0.50	0.22	0.31	0.14	0.13
MgO	13.3	13.1	13.1	12.4	12.2	12.4	12.4	12.1	12.9	13.0	12.5	12.3	11.6	11.8	10.8	11.0	10.7	10.9	12.7	12.0	12.6	12.8
CaO	20.0	20.2	20.4	20.0	19.8	20.3	20.2	20.3	20.8	20.9	20.5	20.3	19.3	19.2	19.5	19.4	19.0	19.0	20.5	20.2	20.9	21.1
Na_2O	2.07	2.00	1.91	1.99	0.84	0.73	0.83	0.72	0.74	0.67	0.95	0.80	0.99	0.96	0.81	0.79	0.82	0.79	0.72	0.58	0.76	0.62
Total	99.8	100.6	100.3	99.8	100.4	100.4	100.5	100.6	100.7	100.9	101.2	101.5	100.5	100.8	100.2	100.3	99.7	99.7	100.4	100.8	100.6	100.5
Si	1.91	1.89	1.89	1.88	1.93	1.92	1.90	1.90	1.91	1.91	1.89	1.88	1.92	1.92	1.91	1.92	1.91	1.93	1.90	1.91	1.89	1.90
Ti	0.01	0.01	0.01	0.01	0.01	0.01	0.01	0.01	0.01	0.01	0.01	0.01	0.01	0.01	0.01	0.01	0.01	0.01	0.01	0.01	0.01	0.01
Al^{IV}	0.09	0.11	0.11	0.12	0.07	0.08	0.10	0.10	0.09	0.09	0.11	0.12	0.08	0.08	0.09	0.08	0.09	0.07	0.10	0.09	0.11	0.10
Al^{VI}	0.12	0.22	0.22	0.19	0.06	0.05	0.08	0.06	0.07	0.05	0.09	0.07	0.06	0.05	0.06	0.06	0.09	0.08	0.07	0.06	0.09	0.07
Fe^{2+}	0.19	0.14	0.14	0.15	0.32	0.30	0.28	0.30	0.26	0.26	0.25	0.28	0.34	0.34	0.37	0.38	0.40	0.41	0.27	0.33	0.25	0.26
Fe^{3+}	0.00	0.00	0.00	0.00	0.09	0.10	0.09	0.11	0.08	0.10	0.12	0.12	0.11	0.12	0.10	0.10	0.06	0.05	0.09	0.08	0.07	0.08
Mn	0.00	0.00	0.00	0.00	0.01	0.01	0.01	0.01	0.01	0.01	0.01	0.01	0.01	0.01	0.02	0.02	0.02	0.02	0.01	0.01	0.00	0.00
Mg	0.72	0.70	0.70	0.67	0.69	0.70	0.69	0.68	0.72	0.72	0.69	0.68	0.66	0.66	0.61	0.63	0.61	0.62	0.71	0.67	0.70	0.71
Ca	0.77	0.78	0.79	0.77	0.80	0.82	0.81	0.82	0.83	0.84	0.82	0.81	0.78	0.78	0.80	0.79	0.78	0.78	0.82	0.81	0.83	0.85
Na	0.14	0.14	0.13	0.14	0.06	0.05	0.06	0.05	0.05	0.05	0.07	0.06	0.07	0.07	0.06	0.06	0.06	0.06	0.05	0.04	0.05	0.04
En	43	43	43	42	36	36	37	36	38	38	37	36	35	35	32	33	33	33	37	35	38	37
Fs	11	9	9	10	22	21	20	22	18	19	19	21	24	25	26	26	26	25	19	22	18	18
Wo	46	48	48	48	42	43	43	43	44	43	44	43	41	41	42	41	42	41	43	43	45	44

TABLE 7: Orthopyroxene chemistry for Tanzanian granulite xenoliths

	Labait																			
	Two-pyroxene granulites																			
	LB04-04		LB04-12		LB04-16		LB04-19		LB04-34		LB04-38		LB04-41		LB04-50		LB04-52		LB04-53	
Domain	core	rim	core	rim	core	rim	core	rim	core	rim	core	rim	core	rim	core	rim	core	rim	core	rim
n	5	5	5	5	5	5	5	5	5	5	5	5	5	5	5	5	5	5	5	5
SiO_2	52.3	52.6	51.7	51.8	51.9	50.9	52.0	52.1	52.2	52.4	52.1	52.0	52.2	52.4	52.0	52.9	52.3	52.3	52.8	52.9
TiO_2	0.07	0.06	0.09	0.03	0.06	0.05	0.07	0.04	0.04	0.04	0.10	0.05	0.05	0.08	0.10	0.04	0.04	0.02	0.02	0.02
Al_2O_3	1.51	1.31	5.05	4.97	2.83	3.51	4.03	4.02	3.90	4.76	5.04	5.74	5.71	5.87	2.63	2.73	3.81	4.00	3.60	3.38
FeO	27.2	27.7	24.0	24.3	26.3	26.0	23.0	23.2	23.2	22.4	22.2	22.8	21.2	20.8	27.3	26.0	23.5	23.9	23.9	23.2
MnO	0.80	0.85	0.47	0.45	0.21	0.22	0.09	0.11	0.09	0.10	0.10	0.10	0.09	0.07	0.14	0.16	0.11	0.10	0.07	0.12
MgO	18.7	18.6	20.5	20.6	19.5	17.5	21.6	21.7	21.8	21.2	22.1	21.8	23.0	23.0	19.6	19.4	21.2	21.4	22.0	22.1
CaO	0.54	0.43	0.48	0.28	0.49	1.97	0.59	0.28	0.46	0.33	0.44	0.27	0.30	0.23	0.55	0.39	0.71	0.26	0.26	0.28
Na_2O	0.01	0.01	0.03	0.01	0.03	0.26	0.03	0.01	0.02	0.01	0.04	0.01	0.08	0.03	0.02	0.16	0.04	0.01	0.01	0.00
Total	101.0	101.5	102.4	102.4	101.4	100.3	101.4	101.5	101.7	101.3	102.1	102.7	102.6	102.5	102.4	101.9	101.8	101.9	102.7	102.0
Si	1.97	1.98	1.89	1.89	1.94	1.93	1.91	1.91	1.91	1.92	1.89	1.88	1.88	1.88	1.93	1.96	1.92	1.91	1.92	1.93
Ti	0.00	0.00	0.00	0.00	0.00	0.00	0.00	0.00	0.00	0.00	0.00	0.00	0.00	0.00	0.00	0.00	0.00	0.00	0.00	0.00
Al^{IV}	0.03	0.02	0.11	0.11	0.06	0.07	0.09	0.09	0.09	0.08	0.11	0.12	0.12	0.12	0.07	0.04	0.08	0.09	0.08	0.07
Al^{VI}	0.04	0.03	0.11	0.11	0.06	0.08	0.08	0.09	0.08	0.12	0.10	0.12	0.12	0.13	0.05	0.08	0.08	0.09	0.07	0.07
Fe^{2+}	0.86	0.87	0.73	0.74	0.82	0.82	0.70	0.71	0.70	0.68	0.67	0.69	0.62	0.62	0.82	0.81	0.72	0.73	0.72	0.71
Fe^{3+}	0.00	0.00	0.00	0.00	0.00	0.01	0.01	0.00	0.01	0.00	0.01	0.00	0.01	0.00	0.03	0.00	0.00	0.00	0.01	0.00
Mn	0.03	0.03	0.01	0.01	0.01	0.01	0.00	0.00	0.00	0.00	0.00	0.00	0.00	0.00	0.00	0.00	0.00	0.00	0.00	0.00
Mg	1.05	1.04	1.12	1.12	1.09	0.99	1.18	1.19	1.19	1.16	1.20	1.17	1.23	1.23	1.09	1.07	1.16	1.17	1.19	1.20
Ca	0.02	0.02	0.02	0.01	0.02	0.08	0.02	0.01	0.02	0.01	0.02	0.01	0.01	0.01	0.02	0.02	0.03	0.01	0.01	0.01
Na	0.00	0.00	0.00	0.00	0.00	0.02	0.00	0.00	0.00	0.00	0.00	0.00	0.01	0.00	0.00	0.01	0.00	0.00	0.00	0.00
En	54	53	59	59	56	52	62	62	62	62	63	63	65	66	55	56	61	61	62	62
Fs	45	46	40	40	43	44	37	37	37	37	36	37	34	34	43	43	38	38	38	37
Wo	1	1	1	1	1	4	1	1	1	1	1	1	1	0	1	1	1	1	1	1

Analytical uncertainty (2σ RSD, n > 12): SiO_2 = 2.3%; TiO_2 = 8.5%; Al_2O_3 = 3.9%; FeO = 3.0%; MnO ~150%; MgO = 2.2%; CaO = 2.7%; Na_2O ~170%

TABLE 7: Orthopyroxene chemistry for Tanzanian granulite xenoliths (cont.)

	Labait										Lashaine				Naibor Soito			
	2px gran		Gt-opx gran		2px-hbl gran						Gt-cpx gran			Bt gran	Quartz granulites			
	LB04-93		LB04-39		LB04-07		LB04-48		LB04-82		89-734	89-741	89-744	89-733	NS04-13A		NS04-13B	
Domain	core	rim	core	rim	core	rim	core	rim	core	rim					core	rim	core	rim
n	5	5	5	5	5	5	5	5	5	5					5	5	5	5
SiO_2	52.5	52.2	55.3	55.5	52.8	53.2	52.2	52.4	52.6	53.0	52.9	54.7	51.5	50.5	51.2	51.3	51.1	51.0
TiO_2	0.03	0.06	0.02	0.02	0.06	0.03	0.06	0.05	0.07	0.04	-	-	0.06	-	0.28	0.25	0.18	0.17
Al_2O_3	3.53	5.25	3.78	3.78	2.76	2.06	3.76	3.40	3.74	3.17	1.21	2.09	8.20	0.42	1.87	1.86	3.10	2.91
FeO	23.0	22.5	13.2	12.8	24.8	24.9	24.8	24.4	22.8	22.3	22.6	15.2	11.7	33.9	25.7	25.4	25.7	25.7
MnO	0.09	0.09	0.05	0.02	0.13	0.15	0.51	0.46	0.70	0.66	-	-	-	0.23	0.46	0.49	0.58	0.63
MgO	21.5	20.6	28.5	28.5	20.3	20.7	20.2	20.1	21.5	21.6	23.2	26.7	26.8	14.5	19.5	19.5	19.3	19.4
CaO	0.46	0.56	0.27	0.19	0.86	0.38	0.51	0.84	0.56	0.34	0.22	0.66	1.61	0.41	0.98	1.05	0.94	1.05
Na_2O	0.03	0.02	0.02	0.01	0.02	0.01	0.02	0.09	0.01	0.02	-	0.64	-	0.13	0.04	0.04	0.04	0.05
Total	101.2	101.3	101.1	100.8	101.7	101.4	102.1	101.7	101.9	101.2	100.1	100.0	99.8	100.0	100.1	99.9	100.9	100.9
Si	1.93	1.91	1.94	1.95	1.95	1.97	1.92	1.93	1.92	1.95	1.96	1.97	1.83	1.99	1.94	1.95	1.92	1.92
Ti	0.00	0.00	0.00	0.00	0.00	0.00	0.00	0.00	0.00	0.00	0.00	0.00	0.00	0.00	0.01	0.01	0.01	0.00
Al^{IV}	0.07	0.09	0.06	0.05	0.05	0.03	0.08	0.07	0.08	0.05	0.04	0.03	0.17	0.01	0.06	0.05	0.08	0.08
Al^{VI}	0.08	0.14	0.09	0.10	0.07	0.06	0.08	0.08	0.08	0.08	0.02	0.06	0.17	0.01	0.03	0.03	0.06	0.05
Fe^{2+}	0.71	0.69	0.39	0.38	0.76	0.77	0.76	0.75	0.70	0.68	0.67	0.42	0.35	1.09	0.79	0.79	0.78	0.77
Fe^{3+}	0.00	0.00	0.00	0.00	0.00	0.00	0.00	0.00	0.00	0.00	0.03	0.03	0.00	0.02	0.03	0.02	0.03	0.04
Mn	0.00	0.00	0.00	0.00	0.00	0.00	0.02	0.01	0.02	0.02	0.00	0.00	0.00	0.01	0.01	0.02	0.02	0.02
Mg	1.18	1.13	1.49	1.49	1.12	1.14	1.11	1.11	1.17	1.18	1.28	1.43	1.42	0.85	1.10	1.10	1.08	1.09
Ca	0.02	0.02	0.01	0.01	0.03	0.02	0.02	0.03	0.02	0.01	0.01	0.03	0.06	0.02	0.04	0.04	0.04	0.04
Na	0.00	0.00	0.00	0.00	0.00	0.00	0.00	0.01	0.00	0.00	0.00	0.04	0.00	0.01	0.00	0.00	0.00	0.00
En	62	61	79	80	58	59	58	58	61	62	64	75	78	43	56	56	56	56
Fs	37	38	21	20	40	40	41	40	38	37	35	24	19	56	42	42	43	42
Wo	1	1	1	0	2	1	1	2	1	1	0	1	3	1	2	2	2	2

TABLE 7: Orthopyroxene chemistry for Tanzanian granulite xenoliths (cont.)

	Naibor Soito													
	Quartz granulites												Qtz-free gran	
	NS04-53		NS04-91				NS04-93		NS04-96		NS04-104		NS04-61	NS04-80
Domain	core	rim	core	rim	corona	GM	corona	GM	core	rim	core	rim	corona	corona
n	5	5	5	5	5	5	5	5	5	5	5	5	5	5
SiO_2	48.8	49.0	52.2	51.8	51.4	51.2	51.3	50.7	51.1	50.9	50.2	50.3	50.9	51.7
TiO_2	0.27	0.26	0.14	0.20	0.20	0.21	0.21	0.22	0.23	0.28	0.24	0.25	0.25	0.20
Al_2O_3	4.10	3.98	2.34	2.28	2.50	3.39	3.83	4.54	1.93	1.82	2.33	2.11	2.92	2.73
FeO	31.4	31.2	23.4	23.4	24.7	24.0	24.9	25.1	27.2	26.9	28.6	28.5	25.9	23.7
MnO	0.45	0.46	0.45	0.51	0.57	0.53	0.38	0.40	0.71	0.70	0.98	0.91	0.54	0.30
MgO	15.2	15.3	21.9	21.1	20.3	20.1	20.2	19.6	18.5	18.4	16.5	16.8	18.9	21.0
CaO	0.41	0.41	0.65	0.95	0.99	0.93	1.03	0.99	1.20	1.30	1.19	1.22	1.10	0.85
Na_2O	0.04	0.03	0.03	0.04	0.04	0.04	0.05	0.05	0.07	0.08	0.06	0.05	0.04	0.02
Total	100.7	100.7	101.1	100.2	100.7	100.4	101.9	101.6	100.9	100.4	100.1	100.1	100.6	100.5
Si	1.89	1.89	1.93	1.94	1.93	1.92	1.90	1.88	1.94	1.94	1.94	1.94	1.92	1.93
Ti	0.01	0.01	0.00	0.01	0.01	0.01	0.01	0.01	0.01	0.01	0.01	0.01	0.01	0.01
Al^{IV}	0.11	0.11	0.07	0.06	0.07	0.08	0.10	0.12	0.06	0.06	0.06	0.06	0.08	0.07
Al^{VI}	0.08	0.08	0.04	0.04	0.04	0.07	0.07	0.08	0.02	0.02	0.04	0.03	0.05	0.05
Fe^{2+}	0.99	0.98	0.69	0.71	0.74	0.74	0.73	0.75	0.81	0.82	0.90	0.89	0.80	0.72
Fe^{3+}	0.03	0.03	0.04	0.02	0.03	0.01	0.04	0.03	0.05	0.04	0.02	0.02	0.02	0.02
Mn	0.01	0.02	0.01	0.02	0.02	0.02	0.01	0.01	0.02	0.02	0.03	0.03	0.02	0.01
Mg	0.88	0.88	1.21	1.18	1.13	1.12	1.11	1.09	1.05	1.04	0.95	0.96	1.07	1.17
Ca	0.02	0.02	0.03	0.04	0.04	0.04	0.04	0.04	0.05	0.05	0.05	0.05	0.04	0.03
Na	0.00	0.00	0.00	0.00	0.00	0.00	0.00	0.00	0.01	0.01	0.00	0.00	0.00	0.00
En	46	46	61	60	58	58	57	57	53	53	49	49	55	60
Fs	54	53	37	38	40	40	40	41	45	45	49	48	43	38
Wo	1	1	1	2	2	2	2	2	2	3	3	3	2	2

GM denotes groundmass

TABLE 8: Garnet chemistry for Tanzanian granulite xenoliths (cont.)

	Labait			Lashaine										
	Gt-opx gran		Anorth	Garnet-clinopyroxene granulites										
	LB04-39		LB04-27	89-727		89-729	89-730	89-731	89-734	89-739		89-741	89-742	
n	core	rim	kelyphite	core	rim					core	rim		core	rim
Domain	5	5	7	5	5					5	5		5	5
SiO_2	39.6	39.6	39.3	39.3	39.4	40.1	40.0	39.9	38.7	39.6	39.3	40.6	39.6	39.5
TiO_2	0.02	0.01	0.08	0.06	0.06	-	0.72	-	-	0.05	0.06	-	0.05	0.06
Al_2O_3	22.5	22.4	22.8	22.2	22.4	22.5	21.7	22.1	21.7	22.4	22.5	22.4	22.4	22.4
FeO	19.2	18.7	13.5	15.0	14.2	18.3	18.5	20.3	25.9	15.1	15.1	19.0	15.0	14.9
MnO	0.42	0.40	0.24	0.31	0.30	0.19	0.21	0.18	0.26	0.32	0.33	0.16	0.29	0.33
MgO	13.8	13.4	13.2	12.7	12.2	10.5	10.7	8.99	7.92	13.1	13.1	12.4	12.5	12.6
CaO	4.65	5.18	7.28	9.25	9.70	8.44	8.25	8.60	5.57	7.95	7.59	4.89	8.90	8.77
Na_2O	0.01	0.01	0.95	-	-	-	-	-	-	-	-	0.41	-	-
Total	100.2	99.8	97.2	98.8	98.3	100.0	100.0	100.2	100.0	98.4	98.0	99.9	98.8	98.5
Si	2.95	2.96	2.97	2.95	2.97	3.00	3.00	3.02	2.99	2.97	2.97	3.02	2.97	2.97
Ti	0.00	0.00	0.00	0.00	0.00	0.00	0.04	0.00	0.00	0.00	0.00	0.00	0.00	0.00
Al	1.98	1.98	2.03	1.97	1.99	1.98	1.92	1.97	1.97	1.98	2.00	1.97	1.98	1.98
Fe^{2+}	1.02	1.02	0.60	0.77	0.80	1.14	1.16	1.28	1.60	0.85	0.86	1.13	0.84	0.84
Fe^{3+}	0.18	0.15	0.25	0.17	0.09	0.01	0.00	0.00	0.07	0.10	0.09	0.06	0.11	0.10
Mn	0.03	0.03	0.02	0.02	0.02	0.01	0.01	0.01	0.02	0.02	0.02	0.01	0.02	0.02
Mg	1.53	1.50	1.49	1.42	1.37	1.18	1.20	1.01	0.91	1.47	1.47	1.38	1.40	1.41
Ca	0.37	0.41	0.59	0.75	0.78	0.68	0.66	0.70	0.46	0.64	0.61	0.39	0.72	0.71
Na	0.00	0.00	0.14	0.00	0.00	0.00	0.00	0.00	0.00	0.00	0.00	0.06	0.00	0.00
Pyr	49	49	51	46	45	39	40	34	30	48	48	47	46	46
Alm	39	38	29	30	29	38	38	43	55	31	31	40	31	31
Grs	12	13	20	24	26	23	22	23	15	21	20	13	23	23

Analytical uncertainty (2σ RSD, n = 22): SiO_2 = 0.92%; TiO_2 = 28%; Al_2O_3 = 1.3%; FeO = 2.7%; MnO = 11%; MgO = 5.5%; CaO = 1.4%; Na_2O ~ 200%

TABLE 8: Garnet chemistry for Tanzanian granulite xenoliths (cont.)

	Lashaine		Naibor Soito											
	Gt-cpx	Bt gran	Quartz granulites								Quartz-free granulites			
	89-744	89-733	NS04-13		NS04-53		NS04-91		NS04-93		NS04-61		NS04-80	
n			core	rim	core	rim	core	rim	core	rim	core	rim	core	rim
Domain			5	5	5	5	5	5	5	5	5	5	5	5
SiO_2	40.4	37.3	38.5	38.4	37.6	37.5	38.5	38.7	38.7	38.6	38.5	38.4	38.8	38.6
TiO_2	-	-	0.03	0.02	0.02	0.03	0.03	0.03	0.03	0.03	0.03	0.03	0.03	0.03
Al_2O_3	22.7	20.8	21.8	21.8	21.2	21.1	21.7	21.8	21.8	21.9	21.7	21.7	22.0	21.8
FeO	16.8	31.1	24.5	24.6	29.4	29.7	24.4	24.3	24.2	24.3	24.8	25.1	23.0	23.2
MnO	0.21	1.29	0.94	1.36	1.07	1.15	1.25	1.37	0.83	0.94	0.98	1.29	0.64	0.73
MgO	12.50	2.76	8.76	8.28	6.32	6.42	8.61	8.64	8.78	8.58	8.04	7.66	9.21	9.08
CaO	7.49	6.67	5.70	5.68	4.04	3.41	5.78	5.83	6.38	6.43	6.11	6.10	6.99	6.66
Na_2O	-	-	0.01	0.00	0.01	0.01	0.00	0.00	0.01	0.00	0.00	0.00	0.00	0.00
Total	100.0	100.0	100.3	100.1	99.7	99.4	100.2	100.6	100.7	100.8	100.2	100.2	100.6	100.2
Si	3.00	2.99	2.96	2.96	2.97	2.97	2.96	2.97	2.96	2.96	2.97	2.97	2.96	2.96
Ti	0.00	0.00	0.00	0.00	0.00	0.00	0.00	0.00	0.00	0.00	0.00	0.00	0.00	0.00
Al	1.98	1.96	1.98	1.98	1.97	1.97	1.97	1.97	1.97	1.97	1.97	1.98	1.97	1.97
Fe^{2+}	1.00	2.00	1.42	1.45	1.81	1.85	1.42	1.41	1.38	1.39	1.48	1.50	1.30	1.33
Fe^{3+}	0.04	0.08	0.15	0.14	0.13	0.13	0.15	0.15	0.17	0.17	0.12	0.13	0.17	0.16
Mn	0.01	0.09	0.06	0.09	0.07	0.08	0.08	0.09	0.05	0.06	0.06	0.08	0.04	0.05
Mg	1.38	0.33	1.00	0.95	0.74	0.76	0.99	0.99	1.00	0.98	0.93	0.88	1.05	1.04
Ca	0.60	0.57	0.47	0.47	0.34	0.29	0.48	0.48	0.52	0.53	0.51	0.51	0.57	0.55
Na	0.00	0.00	0.00	0.00	0.00	0.00	0.00	0.00	0.00	0.00	0.00	0.00	0.00	0.00
Pyr	46	11	33	32	25	25	33	33	33	32	31	29	34	34
Alm	34	70	52	53	64	65	52	51	50	51	53	54	48	48
Grs	20	19	15	16	11	10	16	16	17	17	17	17	19	18

TABLE 9: Hydrous mineral chemistry for Tanzanian granulite xenoliths

	Hornblende							Biotite					
	Labait			Naibor Soito				Labait		Naibor Soito			
	2px-hbl gran			Qtz gran		Qtz-free gran		2px-hbl gran		Qtz gran			Qtz-free
	LB04-07	LB04-48	LB04-82	NS04-13	NS04-93	NS04-61	NS04-80	LB04-48	LB04-82	NS04-13	NS04-53	NS04-91	NS04-61
n	5	5	5	5	5	5	3	5	4	5	5	5	5
SiO_2	41.9	42.0	41.8	40.7	40.4	41.1	42.1	38.5	38.6	36.4	35.4	36.7	36.2
TiO_2	2.12	2.43	2.28	2.41	2.19	2.49	1.81	4.58	4.28	5.19	5.30	5.58	5.57
Al_2O_3	12.4	12.6	12.8	12.8	14.0	12.6	12.6	13.5	14.1	14.8	15.2	14.7	15.0
FeO	14.3	13.0	13.3	17.0	16.8	16.9	15.9	11.7	10.8	18.3	21.6	17.1	18.1
MnO	0.04	0.03	0.03	0.13	0.10	0.12	0.11	0.03	0.02	0.07	0.06	0.09	0.05
MgO	12.2	12.7	12.5	10.8	11.0	10.8	11.8	17.3	18.0	12.5	9.8	13.0	12.1
CaO	12.0	12.2	11.9	11.2	11.2	11.2	11.1	0.01	0.01	0.03	0.10	0.00	0.06
Na_2O	1.87	1.66	1.84	1.38	2.41	1.28	2.04	0.15	0.16	0.37	0.51	0.55	0.36
K_2O	1.68	2.38	2.27	1.70	1.33	1.70	0.98	10.08	10.18	9.24	8.76	9.32	9.28
Cl	0.17	0.04	0.05	0.06	0.04	0.05	0.15	0.03	0.04	0.09	0.28	0.07	0.06
F	0.59	0.76	0.64	0.38	0.22	0.36	0.28	1.71	1.41	0.56	0.69	0.56	0.50
Total	98.9	99.4	99.1	98.4	99.5	98.4	98.7	96.8	97.1	97.4	97.3	97.4	97.1

Analytical uncertainty, bt (2σ RSD, n > 10): SiO_2 = 4.2%; TiO_2 = 5.5%; Al_2O_3 = 11%; FeO = 6.6%; MnO = 120%; MgO = 3.8%; CaO = 3.3%; Na_2O = 250%, K_2O = 3.1%; Cl = 18%; F = 55%

Analytical uncertainty, hbl (2σ RSD, n = 6): SiO_2 = 5.3%; TiO_2 = 1.7%; Al_2O_3 = 6.1%; FeO = 7.8%; MnO = 300%; MgO = 5.6%; CaO = 23%; Na_2O = 7.9%, K_2O = 5.4%; Cl = 14%; F = 180%

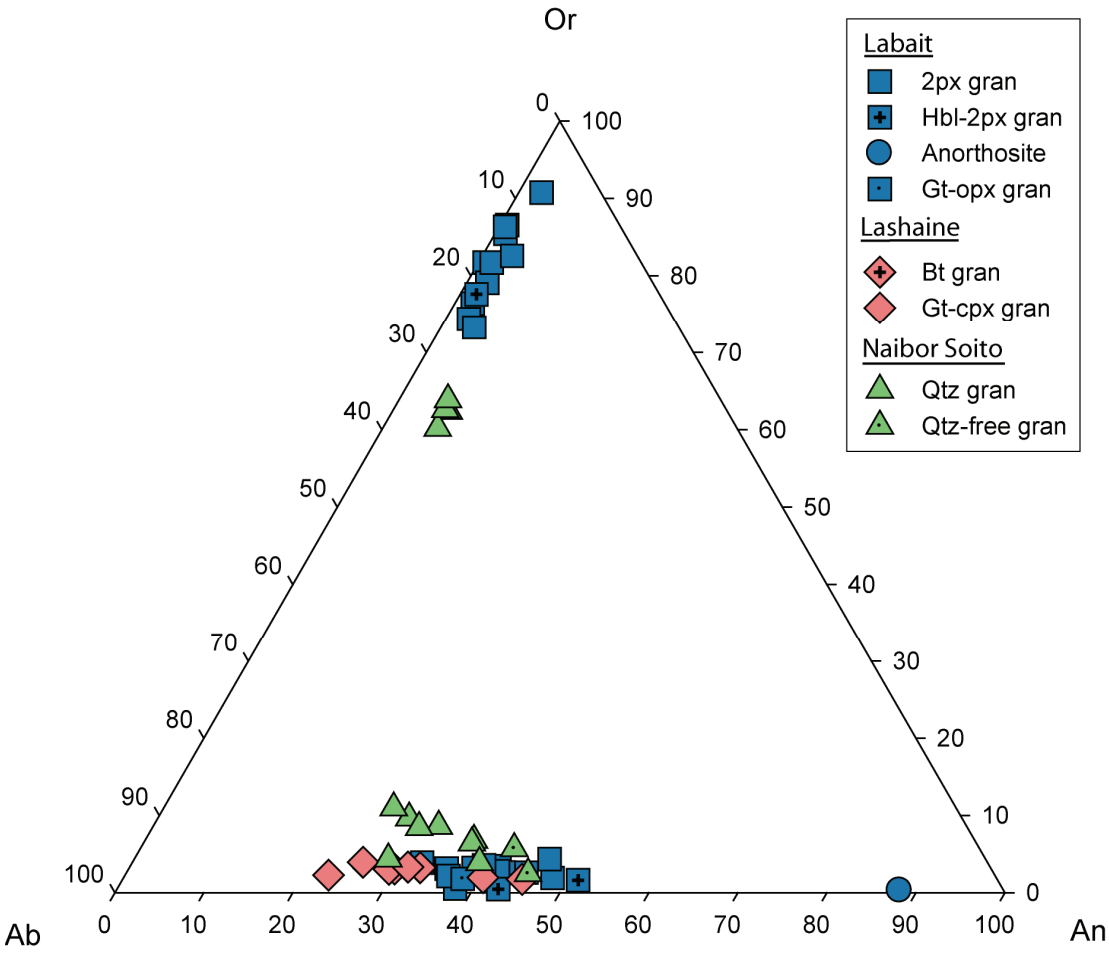

Figure 5. Plagioclase ternary diagram.

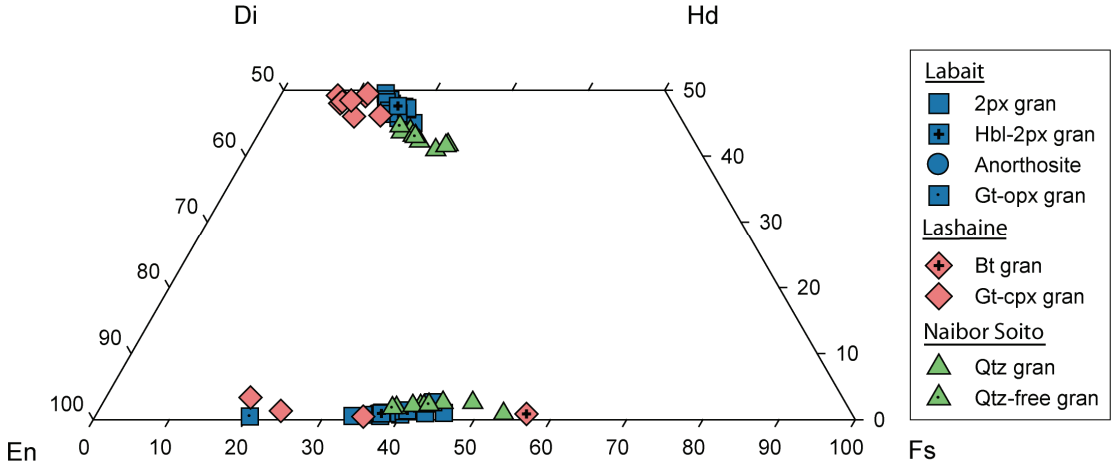

Figure 6. Pyroxene quaternary diagram.

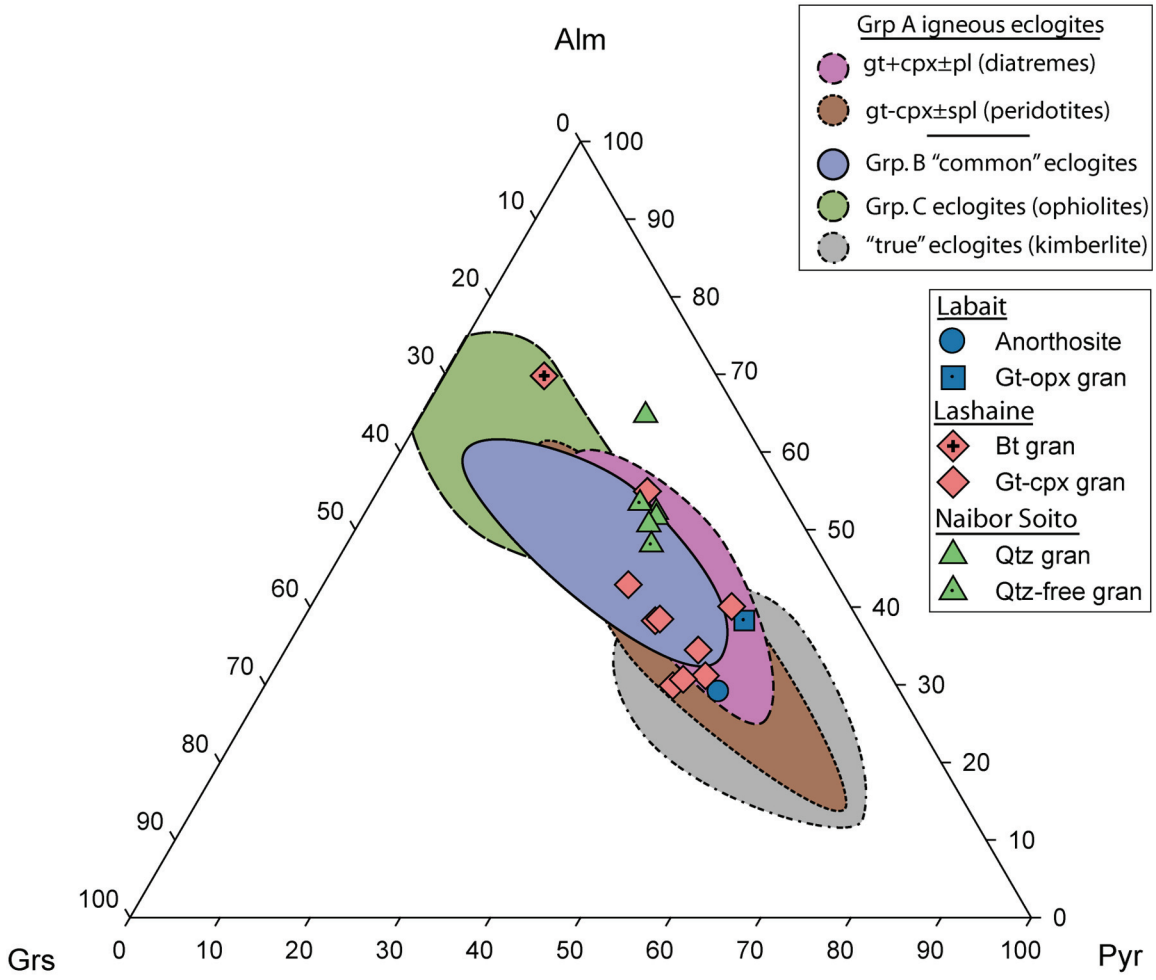

Figure 7. Garnet ternary diagram. Fields based on garnet chemistry in eclogites described in Mottana (1986), following Kempton et al. (1995).

4.3 Thermobarometry

Estimates of pressure and temperature for the Tanzanian crustal xenoliths are summarized in Table 10. Calculations were made using phase compositions normalized to 6 oxygens for pyroxene and 12 oxygens for garnet. Cations were not normalized. Most mineral phases in the granulite xenoliths are unzoned, and samples from Lashaine and Naibor Soito give similar temperatures (<30º difference) whether rim or core compositions are used. However, Labait crystal cores typically preserve temperatures 50-200º hotter than rims. Exceptions to this rule include LB04-07, LB04-41, and LB04-48, in which rim temperatures are hotter.

The garnet-clinopyroxene (T_{KR}; Ravna, 2000) and two-pyroxene (T_{BKN}; Brey and Kohler, 1990) Fe^{2+}-Mg exchange thermometers were used to calculate equilibration temperatures, and the Al-in-orthopyroxene barometer (P_{BKN}; Brey and Kohler, 1990) was used to estimate the equilibration pressure in xenoliths where garnet, orthopyroxene, and clinopyroxene coexist. Both thermometers include a pressure term, which could not be calculated in samples without coexisting orthopyroxene and garnet. In xenoliths in which an independent calculation of pressure could not be made, temperatures were calculated for an assumed pressure of 1 GPa (corresponding to a crustal thickness of ~33 km).

Fe^{3+} contents in garnet and orthopyroxene were estimated based on the charge-balance method of Droop (1987). This correction is important for the Brey and Kohler (1990) barometer, which is sensitive to the oxidation state of iron, but has little effect on temperatures calculated using either thermometer (<20°, based on calculations assuming all iron is Fe^{2+}). Pressures reported here are typically ~0.2 GPa higher than those calculated using a stoichiometric method to estimate Fe^{3+}. Larger differences occur,

however, if molar proportions of Al and Fe^{3+} in orthopyroxene are similar (Carlson and Powell, 1997), as is the case in 89-734, which yields an extremely high pressure (2.7 GPa). Nominal uncertainties, based on application of the thermobarometers to products of high *P-T* experiments, are ±40°C, ±0.6 GPa (2σ) for the Brey and Kohler (1990) thermometer and ±100°C for the Ravna (2000) thermometer. Additional sources of uncertainty not treated in these estimates include disequilibrium (e.g., Carlson and Powell, 1997; Powell, 2008), application of the Brey and Kohler (1990) thermobarometer to samples that equilibrated outside of the range over which it was calibrated (900-1400°C), and the aforementioned uncertainty in the calculation of Fe^{3+}.

T_{BKN} calculated for rim compositions suggests that the Labait xenoliths equilibrated at 480-850°C, with most two-pyroxene granulites falling between 530 and 670°C. By contrast, the Lashaine and Naibor Soito suites record higher temperatures (600-880°C and 810-850°C, respectively). T_{KR} are likewise highest in the Naibor Soito suite (850-940°C) and somewhat lower at Lashaine (590-840°C, with most samples >700°C). Phase compositions reported in Jones et al. (1983) for garnet-clinopyroxene xenoliths from Lashaine give similar T_{KR} (780-880°C). LB04-39 is the only sample from Labait for which compositions of coexisting garnet and clinopyroxene were measured and gives a T_{KR} of 610°C, similar to T_{BKN} calculated for the other Labait samples. Temperatures in the Naibor Soito suite are confined to a narrow range, irrespective of the kind of xenolith being considered, but this is not true for the other localities. At Labait, mineral rims from the hornblende-bearing xenoliths (LB04-07, LB04-41, LB04-48) record higher temperatures than those from the two-pyroxene granulites (T_{BKN} > 800°C). Rim temperatures in these xenoliths are also higher than core temperatures, suggesting

that they experienced heating, whereas most of the two-pyroxene granulites show evidence for cooling. At Lashaine, the biotite (89-733) and pyroxene-rich garnet-clinopyroxene granulites (89-734) are the only samples that equilibrated at <700°C.

For samples for which both T_{BKN} and P_{BKN} could be calculated, equilibration conditions range from 720 to 820°C, 1.7 to 2.7 GPa at Lashaine and from 820 to 880°C, 1.3 to 2.6 GPa at Naibor Soito. Jadeite-albite-quartz equilibria in the garnet-clinopyroxene granulites at Lashaine give comparable pressures (1.8-2.3 GPa, after Holland, 1980); because quartz is absent from these samples, these pressures represent maxima. Low Na_2O contents in the Labait and Naibor Soito clinopyroxenes limit the application of this phase equilibria to the Lashaine samples. These high pressures suggest equilibration at depths exceeding 80 km, that is, twice the thickness of the modern crust (Julià et al., 2005). Similar, somewhat hotter *P-T* conditions (900-1000°C, 2.0-2.3 GPa) were reported in a recent abstract about garnet-clinopyroxene granulites from Lashaine that used garnet-clinopyroxene thermometry, kyanite-garnet-clinopyroxene-quartz, and clinopyroxene-plagioclase-quartz phase equilibria to characterize metamorphic conditions (Tsujimori et al., 2008). An earlier study, however, found lower pressures (1.3-1.5 GPa) consistent with equilibration in crust of comparable thickness to that observed today (Jones et al., 1983).

TABLE 10: P-T equilibration conditions for the Tanzanian xenoliths calculated using Fe^{2+}-Mg exchange thermobarometry

		Cores	Rims			
		For 1 GPa	For 1 GPa		For P_{BKN}	
Sample	Type	T_{BKN}	T_{KR}	T_{BKN}	T_{BKN}	P_{BKN}
Labait						
LB04-04	2px gran	780	-	670	-	-
LB04-12	2px gran	760	-	550	-	-
LB04-16	2px gran	690	-	560	-	-
LB04-19	2px gran	710	-	530	-	-
LB04-34	2px gran	650	-	600	-	-
LB04-38	2px gran	750	-	510	-	-
LB04-41	2px gran	550	-	660	-	-
LB04-50	2px gran	660	-	570	-	-
LB04-52	2px gran	630	-	480	-	-
LB04-53	2px gran	610	-	540	-	-
LB04-93	2px gran	800	-	600	-	-
LB04-07	2px -hbl gran	700	-	850	-	-
LB04-48	2px-hbl gran	660	-	780	-	-
LB04-82	2px-hbl gran	650	-	640	-	-
LB04-39	Gt-opx gran	-	610	-	-	-
Lashaine						
89-733	Bt gran	-	590	600	-	-
89-727	Gt-cpx gran	-	790	-	-	-
89-729	Gt-cpx gran	-	840	-	-	-
89-730	Gt-cpx gran	-	840	-	-	-
89-731	Gt-cpx gran	-	740	-	-	-
89-734	Gt-cpx gran	-	660	680	720	2.7
89-734	Gt-cpx gran	-	630	-	-	-
89-739	Gt-cpx gran	-	820	-	-	-
89-739	Gt-cpx gran	-	800	-	-	-
89-741	Gt-cpx gran	-	750	800	820	1.7
89-742	Gt-cpx gran	-	830	-	-	-
89-744	Gt-cpx gran	-	810	870	-	-
Naibor Soito						
NS04-13	Qtz gran	850	910	830	880	2.6
NS04-91	Qtz gran	830	850	830	870	1.7
NS04-93	Qtz gran	820	940	840	820	1.3
NS04-61	Qtz-free gran	820	910	840	870	2.2
NS04-80	Qtz-free gran	820	890	810	850	1.3

4.4 Major and Trace Element Geochemistry

Major and trace element data for all samples are summarized in Table 11 and Figs. 8-16. In addition to Harker diagrams (Fig. 8) and primitive-mantle-normalized trace and rare-earth element diagrams (Figs. 11-16), chemical data from the Tanzanian crustal xenoliths have been plotted on a discrimination diagram described by Kempton and Harmon (1992), which uses variation in SiO_2/Al_2O_3 ratio relative to trace element concentrations in crustal xenoliths to make a first-order distinction between xenoliths formed via melt crystallization and crystal accumulation (Fig. 9a). This scheme capitalizes on the restricted range of SiO_2/Al_2O_3 in basalts (2.9 to 3.5) and andesites (3.5 to 4.5). These differ significantly from SiO_2/Al_2O_3 ratios in plagioclase (2.7 to 2.0 for An_{20-50}) and pyroxene (>6), such that a cumulate/restite dominated by one of these phases may exhibit a bulk rock ratio significantly different than would be found in a crystallized melt. Trace elements provide a second constraint, as a cumulate will fractionate trace elements based on their compatibility in the crystallizing phases, resulting in low concentrations of incompatible elements and variable but generally high concentrations of compatible elements in the bulk rock. Typical ranges in SiO_2/Al_2O_3 and Sm for basaltic to andesitic melts define the gray field in Fig. 9a.

La/Nb and Ti/V ratios are useful in discriminating between igneous rocks formed in different tectonic settings. High La/Nb ratios result from the sequestration of certain fluid-immobile elements (Nb, Ta, and Ti) in rutile in subducting ocean crust. As a result, slab fluids that fertilize the mantle wedge that undergoes partial melting to form arc basalts typically have low concentrations of Nb relative to similarly incompatible elements. Low La/Nb ratios (<1.4) are therefore typical of mid-ocean ridge basalts

(MORB) or ocean-island basalts (OIB), whereas high La/Nb (>1.4) are, for the most part, confined to volcanic arc basalts (e.g., Condie, 1999). Ti/V ratios, by contrast, vary primarily based on the oxidation state of V. Ti-V systematics in basalts from different tectonic settings are summarized in Fig. 9b (Shervais, 1982).

4.4.1 Labait

All meta-gabbroic, two-pyroxene granulite xenoliths from this locality are mafic (SiO_2 = 47-54 wt%), with high TiO_2 and K_2O relative to samples from the other suites. SiO_2/Al_2O_3 ratios overlap with values found in basalts (Fig. 9a). Correlation between major elements and SiO_2 is limited, although all three subsets of the Labait meta-gabbros show negative correlations between SiO_2 and Fe_2O_3 or MnO and positive correlations between SiO_2 and K_2O (Fig. 8). The meta-gabbros have relatively high Al_2O_3 and Na_2O and low MgO relative to tholeiitic basalt (typified here by a tholeiite from the Ontong Java Plateau; Neal, 1997). LB04-46 is distinct from the other two-pyroxene granulites, with high TiO_2 and low MgO. This sample also has 410 ppm Ni, the highest concentration seen in the Tanzanian xenoliths (Fig. 10a).

Primitive-mantle-normalized-trace-element patterns (spider diagrams) for all two-pyroxene granulites are similar (Fig. 11a). Between K and Lu, patterns are generally smooth and negatively sloped, with small anomalies at Sr, P, and Ti. Concentrations of the large-ion lithophile elements (LILE, including Cs, Ba, Rb, Th, and U, all of which are extremely incompatible during partial melting of the mantle) are generally low, except for Ba, which is strongly enriched. While Nb and Ti depletions are characteristic of basalts that formed in convergent margins or that have assimilated continental crust, the

relatively low concentrations of Cs, Th, and U are atypical of basaltic melts. Extreme enrichment of Ba (>5000 ppm in some samples) is also unusual, as is its fractionation from geochemically similar elements. Ba/Rb, for example, is typically ~10 in basalts and most continental rocks, but ranges to much higher values in the two-pyroxene granulites (70-440). The highest Ni and lowest Nb concentrations in the Labait xenoliths occur in these Ba-rich xenoliths (Fig. 10a and c). REE patterns are LREE-enriched (La/Yb_n=5.0-17.4) and Eu anomalies are small or absent (Eu/Eu*=0.8-1.2) (Fig. 12a). Ni concentrations are high (>100 ppm, even at low Mg numbers), typical of Archean basalts (Arndt, 1991), but do not correlate with SiO_2 or MgO (Fig. 10a). La/Nb ratios range from 1.3 to 7.2, and Ti/V ratios range from 39 to 53 (Fig. 9b).

Both the garnet-orthopyroxene and hornblende-bearing granulites range to higher contents of TiO_2 and CaO and lower contents of Na_2O relative to the two-pyroxene granulites. The hornblende-bearing two-pyroxene granulites have higher Fe_2O_3 and MgO and lower SiO_2 relative to the two-pyroxene granulites, but generally fall on the correlations defined by the more abundant xenoliths (e.g., Fe_2O_3-SiO_2). Trace element patterns for the hornblende-bearing xenoliths are variable (Figs. 11b and 12b), but share key features, including low concentration of most LILE, Ba enrichment, and Nb and Ti depletion, with the other metagabbro xenoliths. However, LB04-07 has a flat REE pattern, and element depletions in LB04-82 are less pronounced. Both samples are LREE-enriched, but variably so, with the REE pattern for LB04-07 being relatively flat (La/Yb_n=1.7). La/Nb ratios are somewhat lower than in the two-pyroxene granulites (1.4-2.7).

The garnet-orthopyroxene granulites are characterized by relatively high Al_2O_3

contents, but also fall within the range of the two-pyroxene granulites for most major elements. Trace element systematics are likewise similar, but REE patterns show small, positive Eu anomalies (Eu/Eu*=1.2-1.4) and flat HREE patterns (Gd/Yb_n=1.1-1.5). La/Nb ratios are similar to those observed in the hornblende-bearing granulites (1.8-2.5).

Anorthosite LB04-27 bears little resemblance to the other Labait xenoliths. It is strongly enriched in Al_2O_3 and CaO, but has low concentrations of all other major elements (Fig. 8), and its SiO_2/Al_2O_3 ratio is low compared to the range seen in basaltic melts. Most trace elements are present at low concentrations, but Sr and Eu define small, positive anomalies (Eu/Eu*=1.5) (Figs. 11c and 12c). Its Ba concentration is also high, although not to the extent seen in the two-pyroxene granulites.

4.4.2 Lashaine

Dawson (1977) reported major and trace-element (Ba, Ni, Cr, Rb, Sr, Y) concentrations for three granulite xenoliths from Lashaine, one of which (BD-528) was selected for analysis of Sr and Nd isotopes by Cohen et al. (1984). With the exception of Zr concentrations, which exceed 200 ppm in all three xenoliths analyzed by Dawson (1977), these samples are very similar to the garnet-clinopyroxene granulites described here.

The Lashaine garnet-clinopyroxene granulites are mafic, with SiO_2 contents ranging from 47 to 53 wt%. They generally have high Al_2O_3 and Na_2O and low concentrations of mafic elements relative to tholeiitic basalt (Fig. 8). SiO_2/Al_2O_3 ratios vary from 2.3 to 3.1, a range that overlaps that observed in basalts, but extends to lower values more typical of plagioclase-rich cumulates (Fig. 9a). Major element abundances

are well-correlated, with Al_2O_3, Na_2O, and K_2O increasing and MgO and Fe_2O_3 decreasing as SiO_2 increases (Fig. 8). Major element abundances, in turn, relate to the modal proportion of plagioclase and pyroxene in the xenoliths, with the highest SiO_2, Al_2O_3, and Na_2O found in the plagioclase-rich samples and the highest Fe_2O_3 and MgO found in the more clinopyroxene-rich xenoliths. For some oxides, notably Fe_2O_3, the mosaic xenoliths 89-730 and 89-734 have higher concentrations than would be expected based on extrapolation of the trend defined by the other garnet-clinopyroxene xenoliths.

Incompatible trace element abundances (Fig. 13a-b, 14a-b) are low relative to most crustal xenoliths from Labait and Naibor Soito, but are comparable to those in the Labait anorthosite LB04-27. Most trace elements (including the transition metals and REEs) correlate negatively with SiO_2 and positively with MgO, such that the most plagioclase-rich (e.g., 89-729, 89-735) xenoliths have the lowest concentrations of most elements (Figs. 13a, 14a). Ni concentrations, for example, are low in the plagioclase-rich xenoliths (18-62 ppm), but high in the pyroxene-rich xenoliths (183-285 ppm). By contrast, Sr, which is compatible in plagioclase, is enriched and strongly fractionated from other moderately incompatible elements in the most plagioclase-rich xenoliths, producing extremely high Sr/Y ratios (>700) in 89-729, 89-731, and 89-735 (Fig. 10b). REE patterns are modestly LREE-enriched (La/Yb_n=1.2-21.4, with plagioclase-rich xenoliths showing the highest values) and exhibit positive Eu anomalies (Eu/Eu*=1.6-4.6) in Figs. 14a-b. Pyroxene-rich xenolith 89-734 differs dramatically from the other garnet-clinopyroxene xenoliths, showing smaller Sr and Eu anomalies (Eu/Eu*=1.2) and a generally LREE-depleted trace-element pattern (Fig. 13b, 14b).

The biotite granulites only rarely (and perhaps coincidentally) fall on the same

major-element trends as the garnet-clinopyroxene granulites, most compellingly on the plot of Al_2O_3-SiO_2 (Fig. 8). The biotite granulites are most similar to the pyroxene-rich garnet-clinopyroxene xenoliths, particularly 89-734, which, among other similarities, has a comparable Fe_2O_3. The biotite granulites, however, have much higher concentrations of TiO_2 and K_2O than any other Lashaine xenoliths, consistent with the presence of ilmenite and red-brown, Ti-rich mica. In general, they also have much higher incompatible trace element abundances than the garnet-clinopyroxene granulites and relatively smooth, negatively slope trace-element patterns (Fig. 13c). Negative Sr and Eu (Eu/Eu*=0.8) anomalies complementary to the positive anomalies for these elements in the garnet-clinopyroxene xenoliths may imply that the two sets of Lashaine xenoliths are related (Figs. 13 and 14). No significant depletions in Rb, Th, and U are observed in the biotite granulites, and they contain similar or lower concentrations of the transition metals relative to the coronal and mosaic garnet-clinopyroxene granulites (Table 11). Ti/V ratios are much higher than in any other Tanzanian crustal xenolith (73-75), and La/Nb ratios are low (1.3-1.5).

4.4.3 Naibor Soito

Trace-element compositions of the Naibor Soito xenoliths were analyzed by Dr. Shukrani Manya. Crustal xenoliths from this locality span a wide compositional range (SiO_2 = 49-65 wt%, MgO = 2-8 wt%). Quartz-free xenoliths plot at the low SiO_2, high MgO end of this range, with bulk compositions similar to a tholeiitic basalt. Quartz granulites have mafic to intermediate bulk compositions atypical of primitive basalts or average lower crust (e.g., Rudnick and Gao, 2003), with the most evolved compositions

found in NS04-13 and NS04-83. The low MgO (~1.6 wt%) and Ni (~20 ppm) concentrations in these two samples are similar to leucosomes in composite crustal xenoliths from the Kola Peninsula (Kempton, 1995). SiO_2 correlates well with most major elements in all xenoliths in this suite, with Al_2O_3 and Na_2O increasing and Fe_2O_3, MgO, and CaO decreasing with increasing SiO_2 contents (Fig. 8). K_2O contents range up to ~1 wt%, similar to those of the Labait xenoliths but less surprising given the intermediate bulk compositions in the quartz granulites. SiO_2/Al_2O_3 ratios for the Naibor Soito xenoliths range from 3.1-4.0, overlapping the fields for basalt and andesite, but low REE concentrations in the most evolved samples plot below the range typically observed in mafic melts (Fig. 9a). Transition metal concentrations, represented by Ni in Fig. 10a, correlate positively with MgO across both the quartz-bearing and quartz-free xenoliths.

Spider diagrams (Fig. 15a) emphasize the wide range in trace element concentrations within the quartz xenoliths (e.g., 0.1-2.0 ppm Yb). The range is smaller for some elements. For example, Eu concentrations vary by only a factor of ~2 (0.7-1.8 ppm). As a result, samples with the highest concentrations of incompatible trace elements have negative Eu anomalies, whereas samples with lower concentrations show positive Eu anomalies. Setting the wide range in element abundances aside, the patterns themselves are qualitatively similar to those described from Labait: K and Sr are enriched and Cs, Rb, Th, U, Nb, and Ti are depleted. La/Nb ratios are high (2.3-6.8). Ti/V ratios are moderate (33-49). Eu/Eu* anomalies, however, are much larger in the evolved Naibor Soito xenoliths relative to the granulites from Labait (Fig. 16a).

Trace-element patterns in quartz-free xenoliths NS04-61 and NS04-80 are negatively sloped (Fig. 15b). Small depletions in Cs, Rb, Th, U, Nb, Zr, and Ti are

present. Sr is slightly enriched in NS04-61, but no Eu anomaly is present in either sample and REE patterns are smooth (Fig. 16b). Both La/Nb (1.3-1.5) and Ti/V (17-24) are low relative to the quartz granulites, but Ni concentrations are relatively high (95-117 ppm).

TABLE 11: Major and trace element concentrations of the Tanzanian granulite xenoliths

	Labait										
	Two-pyroxene granulates								2Px-hbl gran.		Anor.
	LB04-09	LB04-19	LB04-36	LB04-46	LB04-52	LB04-53	LB04-65	LB04-93	LB04-07	LB04-82	LB04-27
SiO_2	53.60	51.63	52.37	48.01	51.15	52.07	52.87	53.67	47.23	48.19	43.53
TiO_2	0.78	0.90	0.81	2.98	0.88	0.85	0.96	0.92	0.97	1.31	0.23
Al_2O_3	17.44	16.00	17.94	16.85	15.66	15.21	15.63	16.41	15.03	15.87	28.91
Fe_2O_3	6.42	8.16	7.10	10.45	8.66	7.97	8.10	7.90	12.07	12.26	3.82
MnO	0.11	0.13	0.11	0.10	0.14	0.12	0.12	0.13	0.21	0.19	0.06
MgO	3.73	6.75	3.19	2.90	7.12	6.67	4.35	5.95	7.89	6.71	3.31
CaO	5.66	6.53	6.34	4.78	6.55	6.86	7.70	6.36	10.23	7.81	15.17
Na_2O	4.07	3.17	2.93	3.96	3.12	3.45	3.67	3.66	2.45	3.26	1.30
K_2O	1.90	1.54	2.58	2.13	1.29	1.56	1.76	2.06	0.84	1.02	0.38
P_2O_5	0.25	0.29	0.16	1.01	0.35	0.31	0.21	0.33	0.09	0.42	0.10
LOI	2.78	1.65	4.86	2.48	1.13	1.54	1.97	1.02	1.06	1.49	1.63
Trace	0.98	0.83	0.24	0.89	0.87	0.78	0.50	0.38	0.27	0.37	0.24
Total	97.74	97.58	98.63	96.53	96.93	97.38	97.85	98.78	98.33	98.90	98.68
Mg#	45.2	54.0	38.9	28.2	53.8	54.3	43.2	51.7	48.1	43.7	55.1
SiO_2/Al_2O_3	3.1	3.2	2.9	2.8	3.3	3.4	3.4	3.3	3.1	3.0	1.5
XRF											
Sc^	15	22	17	11	25	24	27	21	39	35	13
V^	114	138	92	147	162	159	163	154	263	209	80
Cr^	78	254	65	40	287	284	161	228	265	138	48
Ni^	253	197	107	410	205	169	122	194	202	102	97
Cu^	b.d.	25	18	42	33	44	25	32	51	25	18
Zn^	81	98	72	125	109	101	98	97	102	166	33
Ga^	25	21	19	23	21	18	21	22	18	26	19
Rb^	22	25	75	21	14	22	27	20	11	17	11
Sr^	1042	735	521	723	547	722	703	849	524	1044	436
Y	12	16	19	16	16	15	20	13	26	28	4
Zr^	121	124	268	525	80	92	193	109	53	111	29
Nb	3	4	8	20	4	4	7	9	5	10	7
Ba^	6726	5448	631	5243	5957	4935	2546	1345	531	927	1211
La	18	19	16	61	20	30	19	12	b.d.	32	b.d.
Ce	40	49	27	141	44	61	45	37	14	80	b.d.
Nd	22	29	15	77	32	36	33	21	11	46	7
Pb^	10	8	b.d.	14	6	9	6	9	b.d.	7	b.d.
Th	3	b.d.	b.d.	b.d.	b.d.	b.d.	b.d.	b.d.	b.d.	b.d.	b.d.
ICP-MS											
Sc	-	9.75	2.86	-	18.0	19.6	19.5	17.4	22.2	29.3	8.49
V	-	139	88.4	-	117	140	150	156	234	194	89.4
Cr	-	256	74.2	-	262	263	145	221	229	137	96.9
Co^	-	33.6	18.8	-	34.1	28.3	25.2	28.9	42.6	32.2	19.7
Cu	-	20.4	45.1	-	31.4	33.4	38.8	260	37.7	15.5	18.5
Rb	-	23.3	59.0	-	14.0	21.2	24.5	18.7	10.0	15.3	10.4
Sr	-	688	462	-	573	701	672	868	440	960	462
Y^	-	14.1	15.9	-	15.8	12.9	17.5	11.8	20.1	23.9	2.96

TABLE 11: Major and trace element concentrations of the Tanzanian granulite xenoliths (cont.)

	Labait										
	Two-pyroxene granulates								2Px-hbl gran.		Anor.
	LB04-09	LB04-19	LB04-36	LB04-46	LB04-52	LB04-53	LB04-65	LB04-93	LB04-07	LB04-82	LB04-27
ICP-MS (cont.)											
Zr	-	83	120	-	67	78	110	87	50	80	27
Nb^	-	4.59	10.3	-	3.20	3.90	6.33	11.2	4.37	11.4	-
Cs	-	0.10	0.036	-	0.033	0.057	0.046	0.078	0.020	0.016	0.23
Ba	-	5521	1331	-	11399	8771	4359	2417	458	1354	1659
La^	-	23.2	13.9	-	19.3	28.0	15.7	14.9	6.0	30.8	3.65
Ce^	-	55.6	28.0	-	48.4	62.4	42.3	33.8	16.7	76.2	7.24
Pr^	-	6.79	3.55	-	7.21	8.38	6.35	4.39	2.46	10.52	0.84
Nd^	-	29.7	15.2	-	33.1	36.0	29.4	19.7	11.3	44.6	3.37
Sm^	-	6.10	3.67	-	7.01	6.97	6.48	4.25	3.04	9.56	0.68
Eu^	-	2.2	1.3	-	1.7	1.7	1.6	1.6	1.0	2.0	0.3
Gd^	-	5.03	4.02	-	5.67	5.41	5.43	3.64	3.69	8.19	0.73
Tb^	-	0.67	0.63	-	0.74	0.68	0.74	0.49	0.64	1.10	0.10
Dy^	-	3.35	3.73	-	3.60	3.14	3.72	2.51	4.12	5.40	0.54
Ho^	-	0.61	0.73	-	0.66	0.54	0.68	0.47	0.86	0.96	0.10
Er^	-	1.67	2.07	-	1.79	1.44	1.81	1.28	2.54	2.58	0.30
Tm^	-	0.22	0.29	-	0.23	0.18	0.23	0.17	0.37	0.33	0.04
Yb^	-	1.40	1.89	-	1.43	1.09	1.42	1.08	2.43	2.06	0.26
Lu^	-	0.20	0.27	-	0.20	0.15	0.19	0.15	0.35	0.28	0.036
Hf^	-	2.21	2.77	-	1.92	2.08	2.72	2.15	1.53	2.34	0.51
Pb	-	10.60	3.59	-	6.94	9.53	7.19	12.60	2.59	7.30	1.32
Th^	-	0.091	0.077	-	0.11	0.093	0.16	0.11	0.23	1.57	0.27
U^	-	0.037	0.089	-	0.044	0.027	0.084	0.16	0.12	0.28	0.12
K/Rb	720	510	286	858	787	578	548	862	648	513	280
Rb/Cs	-	259	2078	-	419	396	579	252	539	1048	50
Ba/Rb	306	217	8.4	255	437	220	95.5	67.9	49.3	56.0	106
Ti/V	41	39	53	122	33	32	35	36	22	38	17
Th/U	-	2.5	0.9	-	2.6	3.5	1.9	0.7	2.0	5.6	2.2
Sr/Y	86	46	28	46	34	48	35	64	20	37	114
La/Nb	-	5.1	1.4	-	6.0	7.2	2.5	1.3	1.4	2.7	-
La/Yb_n	-	11.3	5.0	-	9.2	17.4	7.5	9.4	1.7	10.2	9.7
La/Sm_n	-	2.4	2.4	-	1.7	2.5	1.5	2.2	1.2	2.0	3.3
Gd/Yb_n	-	2.9	1.7	-	3.2	4.0	3.1	2.7	1.2	3.2	2.3
Eu/Eu*	-	1.2	1.0	-	0.8	0.9	0.8	1.2	0.9	0.7	1.5

^ denotes preferred value

- denotes that a given element was not measured

b.d. denotes that a given element was present in concentrations below the lower limit of determination

TABLE 11: Major and trace element concentrations of the Tanzanian granulite xenoliths (cont.)

	Labait		Lashaine									
	Gt-opx gran.		Garnet-clinopyroxene granulites								Bt gran.	
	LB04-39	LB04-91	89-726	89-727	89-729	89-730	89-731	89-732	89-734	89-735	89-733	89-745
SiO_2	51.73	50.43	50.96	51.60	52.46	49.28	52.43	52.62	47.33	53.41	46.31	46.55
TiO_2	0.84	1.18	0.36	0.30	0.36	0.52	0.39	0.33	0.81	0.17	3.15	2.71
Al_2O_3	18.37	21.18	17.69	19.47	22.67	16.56	22.56	19.65	15.51	22.31	13.28	13.03
Fe_2O_3	8.36	9.69	4.82	4.76	4.26	9.16	4.20	4.62	14.86	3.36	15.72	14.76
MnO	0.13	0.17	0.09	0.10	0.06	0.16	0.06	0.07	0.19	0.05	0.23	0.22
MgO	5.39	4.45	6.40	5.71	2.86	8.01	2.91	5.01	8.39	4.11	4.83	5.24
CaO	4.95	4.88	11.99	10.20	9.53	10.99	9.48	10.86	9.14	8.61	8.11	7.90
Na_2O	2.40	3.60	3.45	3.70	4.46	3.03	4.45	3.98	2.25	4.94	2.74	3.21
K_2O	2.42	1.64	0.53	0.84	0.63	0.46	0.64	0.76	0.22	0.74	2.30	2.81
P_2O_5	0.21	0.08	0.10	0.04	0.05	0.03	0.06	0.12	0.06	0.16	0.59	0.51
LOI	3.43	1.04	2.26	2.57	1.98	1.32	1.96	2.39	1.84	1.83	1.91	2.23
Trace	0.45	0.39	0.30	0.30	0.23	0.26	0.24	-	-	-	0.30	0.30
Total	98.69	98.74	98.93	99.59	99.54	99.79	99.37	100.41	100.60	99.69	99.47	99.48
Mg#	47.8	39.4	65.3	63.0	48.8	55.4	49.6	60.6	44.5	63.4	30.4	33.5
SiO_2/Al_2O_3	2.8	2.4	2.9	2.7	2.3	3.0	2.3	2.7	3.1	2.4	3.5	3.6
XRF												
Sc^	29	26	24	17	9	32	10	19	32	10	30	29
V^	171	190	125	86	40	233	42	95	281	46	261	230
Cr^	382	320	395	219	31	334	35	212	399	112	119	195
Ni^	278	165	230	133	18	153	19	123	285	62	74	93
Cu^	66	120	145	70	b.d.	52	29	75	46	17	121	109
Zn^	95	151	30	34	23	52	43	40	100	39	157	140
Ga^	19	30	15	17	18	16	17	15	17	17	21	20
Rb^	69	28	14	25	17	8	16	18	7	9	75	67
Sr^	502	886	1160	1365	1417	927	1440	1506	119	1760	371	279
Y	29	22	7	5	b.d.	5	2	4	17	b.d.	48	44
Zr^	117	253	11	12	6	13	7	37	10	39	280	242
Nb	8	15	b.d.	3	b.d.	3	b.d.	5	4	4	22	18
Ba^	1904	859	192	408	301	192	315	478	35	410	676	752
La	16	30	b.d.	b.d.	b.d.	b.d.	b.d.	b.d.	10	b.d.	31	33
Ce	29	47	13	12	b.d.	b.d.	b.d.	b.d.	b.d.	14	80	71
Nd	12	15	7	7	b.d.	b.d.	b.d.	b.d.	b.d.	b.d.	43	39
Pb^	12	12	b.d.	6	5	5	4	b.d.	b.d.	b.d.	13	14
Th	b.d.	b.d.	b.d.	3	3	b.d.	3	b.d.	b.d.	b.d.	6	5
ICP-MS												
Sc	15.4	24.2	21.0	3.29	5.55	18.4	-	14.8	28.5	6.01	15.7	29.0
V	126	196	140	74.1	48.7	206	-	94.2	245	53.2	235	224
Cr	253	324	414	181	74.8	247	-	215	318	163	132	197
Co^	33.1	36.1	27.9	24.9	19.8	41.1	-	25.4	60.4	17.2	42.2	42.9
Cu	55.6	116	130	145	8.9	92.4	-	75.7	44.5	16.7	110	112
Rb	44.6	26.4	14.6	17.1	15.9	7.74	-	19.2	7.33	9.62	67.0	67.3
Sr	441	838	1186	996	1456	825	-	1696	239	1789	332	482
Y^	25.1	22.1	5.83	2.90	1.08	3.73	-	4.21	13.6	1.77	39.3	36.5

TABLE 11: Major and trace element concentrations of the Tanzanian granulite xenoliths (cont.)

	Labait		Lashaine									
	Gt-opx gran.		Garnet-clinopyroxene granulites								Bt gran.	
	LB04-39	LB04-91	89-726	89-727	89-729	89-730	89-731	89-732	89-734	89-735	89-733	89-745
ICP-MS (cont.)												
Zr	108	143	11.1	12.3	5.96	11.1	-	30.9	29.2	6.84	280	260
Nb^	7.29	9.96	0.72	4.16	-	3.81	-	-	-	-	25.6	-
Cs	0.29	0.12	0.057	0.043	0.19	0.079	-	0.037	0.18	0.042	2.09	0.72
Ba	2565	1488	213	598	416	184	-	649	54	470	630	1013
La^	13.4	24.9	3.35	4.81	2.07	2.80	-	4.60	3.20	3.73	34.0	34.4
Ce^	25.9	41.8	6.75	7.66	3.01	5.32	-	7.61	4.75	4.65	83.0	68.3
Pr^	2.36	3.98	0.97	0.97	0.46	0.75	-	1.14	0.77	0.57	10.1	-
Nd^	8.86	14.1	4.62	4.03	1.94	3.29	-	4.95	3.69	2.09	42.3	42.5
Sm^	2.45	3.17	1.26	0.89	0.39	0.83	-	1.18	1.29	0.35	9.43	8.94
Eu^	1.2	1.6	0.7	0.6	0.6	0.5	-	0.7	0.6	0.5	2.4	2.2
Gd^	3.78	4.13	1.44	0.90	0.38	0.95	-	1.26	2.02	0.36	9.47	8.93
Tb^	0.67	0.66	0.22	0.13	0.048	0.15	-	0.19	0.41	0.045	1.47	1.41
Dy^	4.51	3.92	1.26	0.73	0.24	0.88	-	1.03	2.79	0.24	8.49	8.10
Ho^	0.95	0.77	0.24	0.14	0.041	0.17	-	0.19	0.60	0.05	1.67	1.58
Er^	2.77	2.20	0.63	0.36	0.10	0.47	-	0.50	1.78	0.13	4.78	4.66
Tm^	0.41	0.32	0.082	0.047	0.012	0.063	-	0.064	0.27	0.018	0.67	0.65
Yb^	2.77	2.16	0.52	0.29	0.075	0.40	-	0.40	1.78	0.12	4.37	4.18
Lu^	0.40	0.33	0.069	0.040	0.010	0.056	-	0.054	0.26	0.018	0.62	0.60
Hf^	2.43	3.66	0.42	0.36	0.14	0.41	-	0.65	0.92	0.16	6.75	6.60
Pb	16.3	16.2	3.07	4.02	3.55	3.40	-	4.58	4.69	2.63	17.8	12.2
Th^	0.10	0.32	0.07	0.22	0.12	0.17	-	0.27	0.25	0.20	6.87	10.15
U^	0.11	0.26	0.15	0.050	0.042	0.055	-	0.11	0.04	0.08	1.69	1.83
K/Rb	290	494	319	283	308	481	326	345	277	698	256	347
Rb/Cs	239	225	245	576	91	102	-	496	36	209	36	93
Ba/Rb	27.4	31.1	13.8	16.6	17.6	24	19.3	26.1	5.3	47	9.1	11.2
Ti/V	29	37	17	21	21	54	56	22	13	17	73	71
Th/U	0.9	1.3	0.5	4.4	2.8	3.2	-	2.4	7.0	2.6	4.1	5.6
Sr/Y	17	39	170	286	1306	184	734	430	7	994	8	6
La/Nb	1.8	2.5	4.7	1.2	-	0.7	-	-	-	-	1.3	-
La/Yb_n	3.3	7.8	4.4	11.1	18.9	4.7	-	7.8	1.2	21.4	5.3	5.6
La/Sm_n	3.4	4.9	1.7	3.4	3.3	2.1	-	2.4	1.6	6.6	2.2	2.4
Gd/Yb_n	1.1	1.5	2.3	2.5	4.1	1.9	-	2.6	0.9	2.4	1.8	1.7
Eu/Eu*	1.2	1.4	1.6	1.9	4.6	1.6	-	1.8	1.2	3.9	0.8	0.8

TABLE 11: Major and trace element concentrations of the Tanzanian granulite xenoliths (cont.)

	Naibor Soito									
	Quartz granulites							Quartz-free granulites		
	NS04-01	NS04-05	NS04-13	NS04-73	NS04-83	NS04-91	NS04-98	NS04-150	NS04-61	NS04-80
SiO_2	56.20	53.70	65.30	57.88	61.26	55.54	56.40	49.01	50.08	49.52
TiO_2	0.78	0.67	0.14	0.69	0.47	0.78	0.78	0.86	1.01	0.67
Al_2O_3	16.19	17.47	16.49	16.37	17.07	15.56	15.12	15.88	13.68	14.02
Fe_2O_3	5.51	6.16	1.81	5.76	3.66	8.07	7.44	9.01	11.59	10.84
MnO	0.14	0.08	0.03	0.08	0.06	0.18	0.14	0.14	0.21	0.21
MgO	3.00	4.46	1.55	2.68	1.59	6.14	4.85	6.49	7.58	8.07
CaO	6.89	6.04	5.61	6.73	5.77	7.35	7.15	8.27	9.86	11.70
Na_2O	3.56	4.60	4.82	4.61	5.41	3.87	4.27	3.94	2.62	2.29
K_2O	2.37	1.41	0.98	0.96	0.91	0.86	1.00	1.30	0.83	0.48
P_2O_5	0.38	0.39	0.07	0.22	0.29	0.18	0.21	0.68	0.24	0.22
LOI	1.91	2.39	0.57	1.74	1.51	0.35	1.17	1.86	0.81	0.79
Trace	0.24	0.35	0.14	0.20	0.19	0.20	0.21	0.42	0.23	0.19
Total	97.16	97.72	97.53	97.92	98.18	99.09	98.75	97.86	98.75	99.00
Mg#	43.6	50.7	54.8	39.7	38.1	51.9	48.0	50.5	48.1	51.4
SiO_2/Al_2O_3	3.5	3.1	4.0	3.5	3.6	3.6	3.7	3.1	3.7	3.5
XRF										
Sc^	18	13	6	13	8	23	28	26	42	46
V^	115	105	23	99	57	140	129	170	249	242
Cr^	76	108	22	24	10	164	118	233	252	307
Ni^	40	50	19	24	20	65	79	84	117	95
Cu^	b.d.	33	b.d.	17	b.d.	23	27	22	36	33
Zn^	86	105	19	73	49	112	101	118	90	83
Ga^	20	20	17	20	19	20	22	23	15	14
Rb^	51	23	3	18	15	5	7	25	16	9
Sr^	503	1054	399	783	734	315	473	1146	597	241
Y	21	6	2	8	4	15	23	27	20	18
Zr^	196	322	34	170	143	189	176	200	68	42
Nb	8	4	b.d.	3	3	7	10	6	5	5
Ba^	697	1001	658	356	454	392	374	1120	207	328
La	27	23	9	11	10	33	26	56	b.d.	b.d.
Ce	46	39	b.d.	26	25	62	57	117	22	18
Nd	22	16	b.d.	12	9	25	30	63	13	9
Pb^	9	8	8	4	5	5	6	8	4	b.d.
Th	b.d.	b.d.	b.d.	b.d.	b.d.	b.d.	b.d.	3	b.d.	b.d.
ICP-MS										
Sc	13.8	11.2	2.73	10.6	6.05	21.7	26.8	-	43.1	49.8
V	119	92.5	25.6	115	70.7	149	110	-	270	223
Cr	97.1	108	43.8	41.1	31.9	188	128	-	275	322
Co^	23.4	20.4	6.4	14.1	9.7	35.9	25.9	-	50.2	51.4
Cu	8.0	31.6	11.2	19.2	7.8	27.4	27.3	-	41.6	33.7
Rb	25.6	19.1	2.12	13.1	15.7	5.25	6.41	-	17.0	10.8
Sr	470	892	373	789	785	329	490	-	652	264
Y^	20.9	5.17	1.51	8.89	4.17	15.0	23.9	-	20.7	18.2

TABLE 11: Major and trace element concentrations of the Tanzanian granulite xenoliths (cont.)

	Naibor Soito									
	Quartz granulites							Quartz-free granulites		
	NS04-01	NS04-05	NS04-13	NS04-73	NS04-83	NS04-91	NS04-98	NS04-150	NS04-61	NS04-80
ICP-MS (cont.)										
Zr	125	35	20	64	112	62	44	-	50	31
Nb^	7.39	4.77	0.73	4.36	4.61	7.56	12.1	-	6.91	6.22
Cs	0.11	0.060	0.015	0.087	0.032	0.029	0.032	-	0.18	0.077
Ba	601	1262	727	365	552	443	421	-	233	383
La^	25.0	21.9	4.94	12.7	12.6	33.3	27.5	-	10.2	7.8
Ce^	49.8	38.1	7.08	24.2	21.7	67.6	57.6	-	22.2	15.1
Pr^	5.78	4.24	0.64	3.25	2.52	7.79	7.41	-	3.24	2.06
Nd^	22.1	15.5	2.30	13.2	9.34	27.5	30.2	-	13.9	9.04
Sm^	4.57	2.43	0.37	2.56	1.54	4.44	6.40	-	3.37	2.37
Eu^	1.4	1.8	0.8	1.2	0.9	1.2	1.1	-	1.0	0.8
Gd^	4.99	2.55	0.46	2.62	1.64	4.90	6.39	-	3.50	2.64
Tb^	0.69	0.24	0.050	0.33	0.18	0.55	0.87	-	0.60	0.48
Dy^	3.86	1.00	0.26	1.70	0.82	2.80	4.67	-	3.67	3.10
Ho^	0.77	0.18	0.052	0.32	0.15	0.55	0.88	-	0.75	0.66
Er^	2.18	0.57	0.16	0.92	0.43	1.60	2.42	-	2.15	1.93
Tm^	-	-	-	-	-	-	-	-	-	-
Yb^	1.96	0.51	0.14	0.77	0.35	1.42	2.02	-	2.04	1.94
Lu^	0.28	0.074	0.021	0.11	0.049	0.20	0.28	-	0.29	0.28
Hf^	3.11	0.85	0.52	1.70	2.44	1.70	1.43	-	1.61	1.14
Pb	7.58	8.44	8.76	3.84	4.84	7.26	8.02	-	3.77	2.46
Th^	1.67	0.12	0.069	0.13	0.058	1.23	0.93	-	0.36	0.42
U^	0.89	0.20	0.051	0.14	0.26	0.12	0.17	-	0.27	0.23
K/Rb	383	505	2567	433	490	1501	1240	432	427	449
Rb/Cs	481	387	210	213	480	163	209	-	87	116
Ba/Rb	14	43	207	19	30	82	56	45	13	37
Ti/V	41	38	38	42	49	33	36	30	24	17
Th/U	1.9	0.6	1.4	1.0	0.2	10.2	5.5	-	1.3	1.8
Sr/Y	23	183	182	93	182	21	20	42	30	13
La/Nb	3.4	4.6	6.8	2.9	2.7	4.4	2.3	-	1.5	1.3
La/Yb_n	8.7	29.3	23.4	11.3	24.7	16.0	9.3	-	3.4	2.7
La/Sm_n	3.4	5.6	8.2	3.1	5.1	4.7	2.7	-	1.9	2.1
Gd/Yb_n	2.1	4.1	2.6	2.8	3.8	2.8	2.6	-	1.4	1.1
Eu/Eu*	0.9	2.2	6.1	1.4	1.7	0.8	0.5	-	0.9	0.9

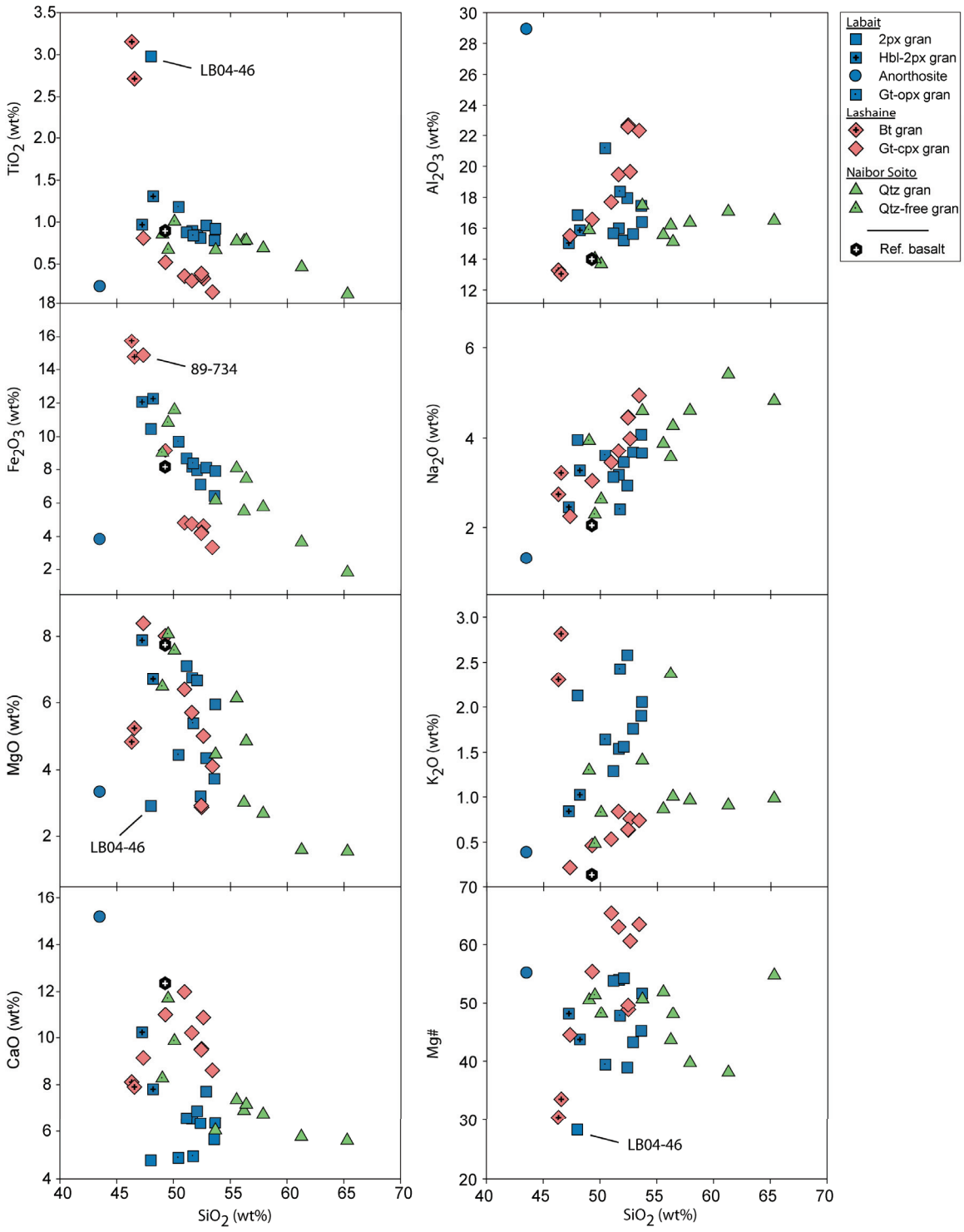

Figure 8. Harker diagrams for the Tanzanian granulite xenoliths. Reference composition is a thoeliitic basalt from the Ontong Java Plateau (O'Neal et al., 1997).

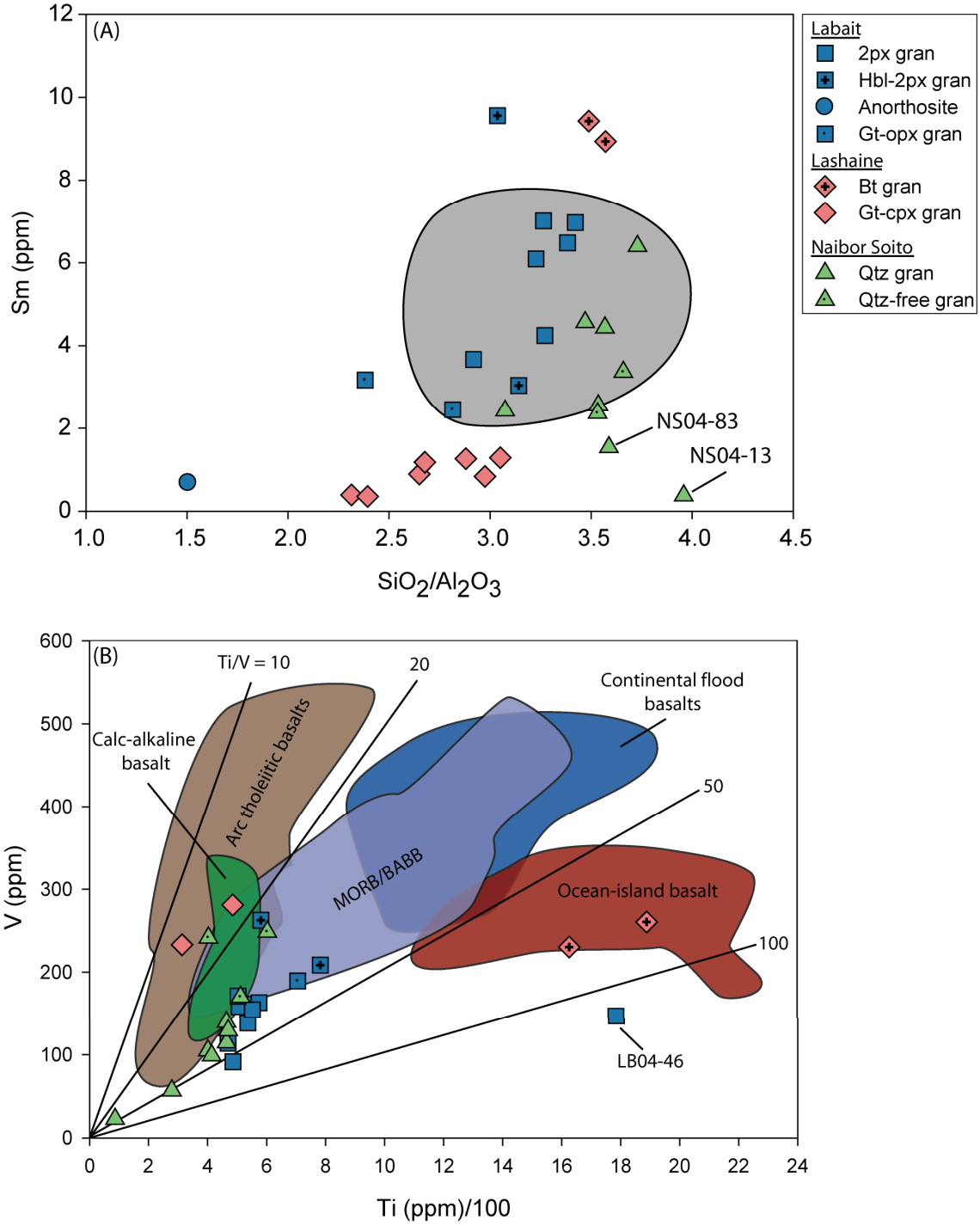

Figure 9. (a) Cumulate/melt discrimination plot, following Kempton and Harmon (1992). Gray field shows the range observed in basaltic-andesitic melts; (b) Ti-V discrimination plot, following Shervais (1982).

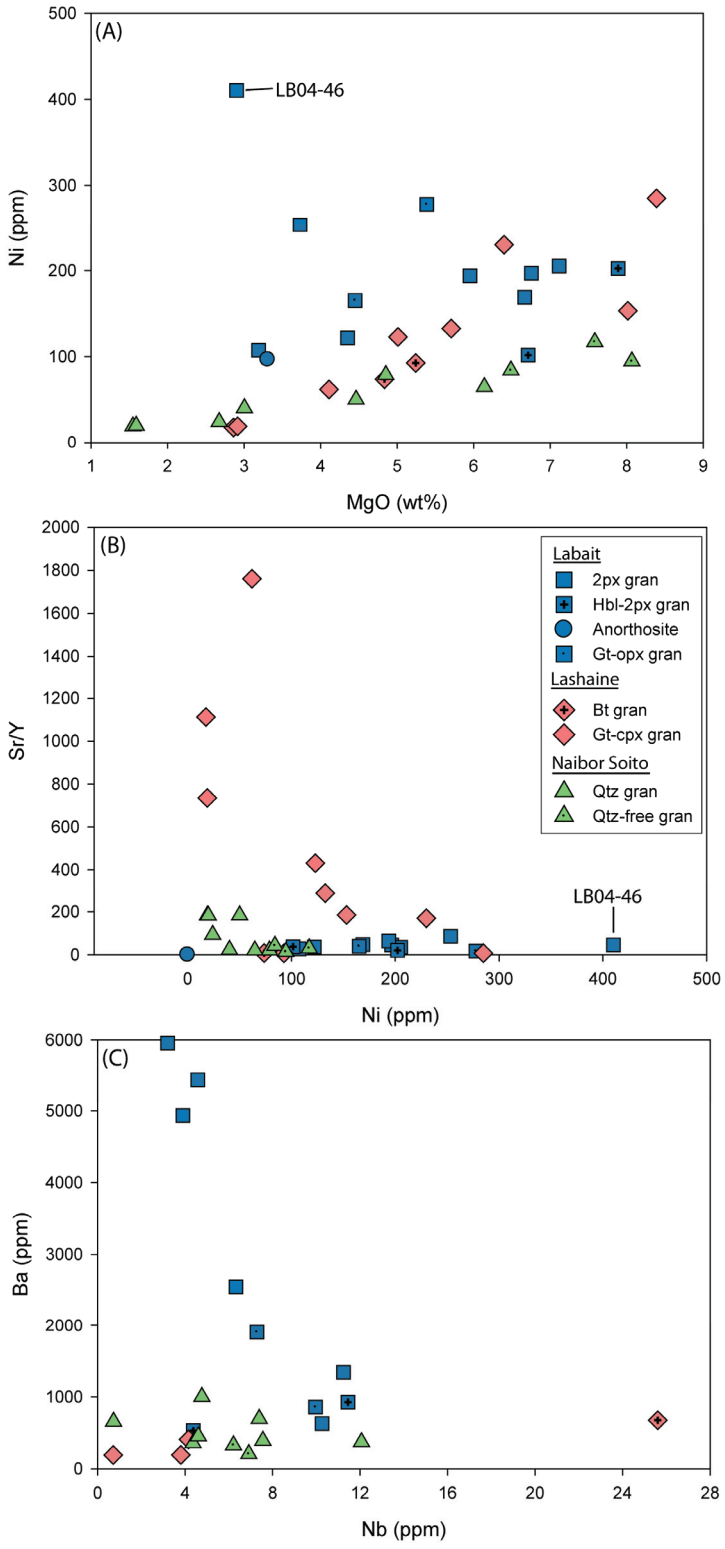

Figure 10. Trace element co-variation diagrams, including (a) Ni vs. MgO; (b) Sr/Y vs. Ni; and (c) Ba vs. Nb.

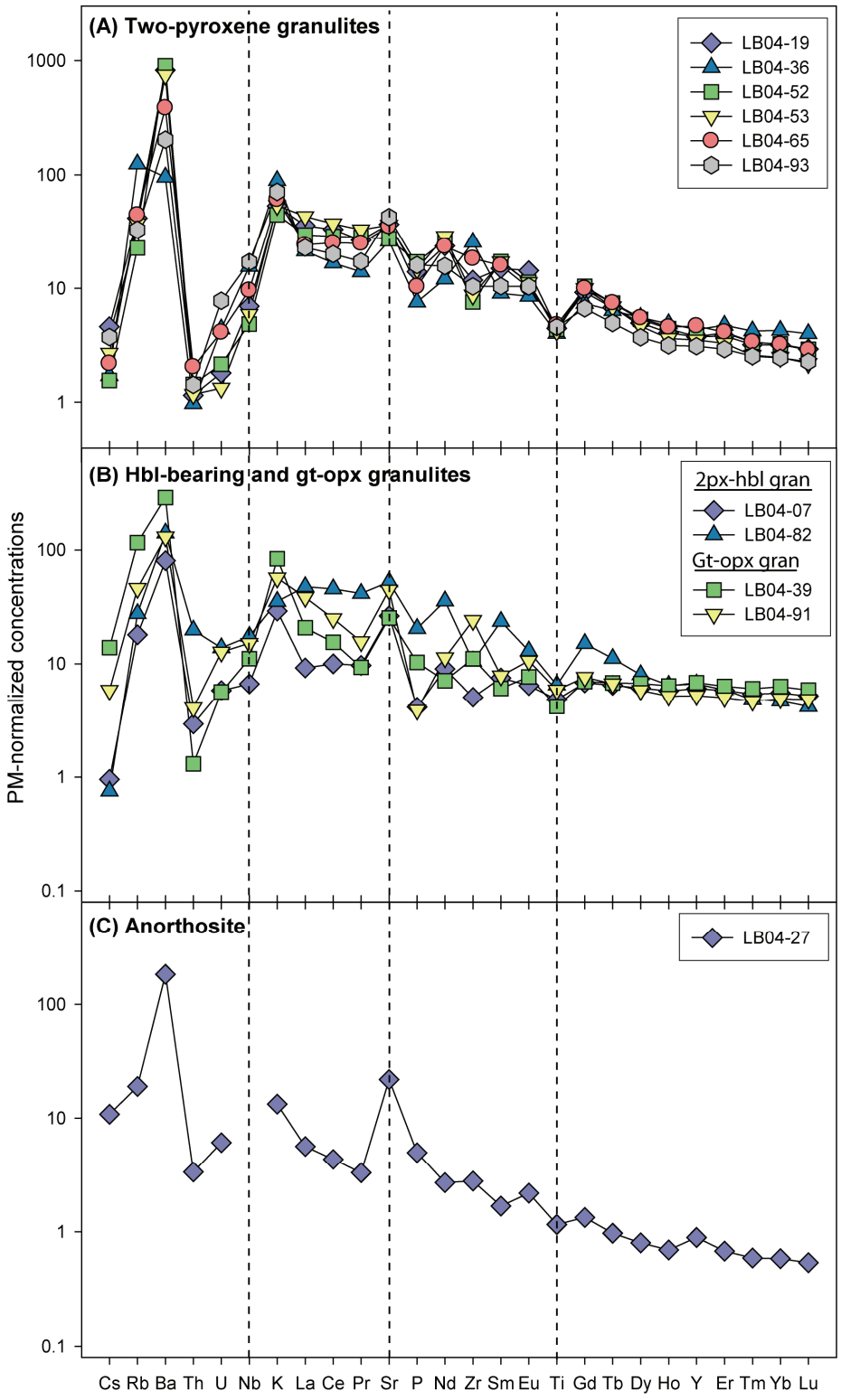

Figure 11. Primitive-mantle-normalized trace element plot for the Labait granulite xenoliths. Note different scale in (a). Normalizing values from McDonough and Sun (1995).

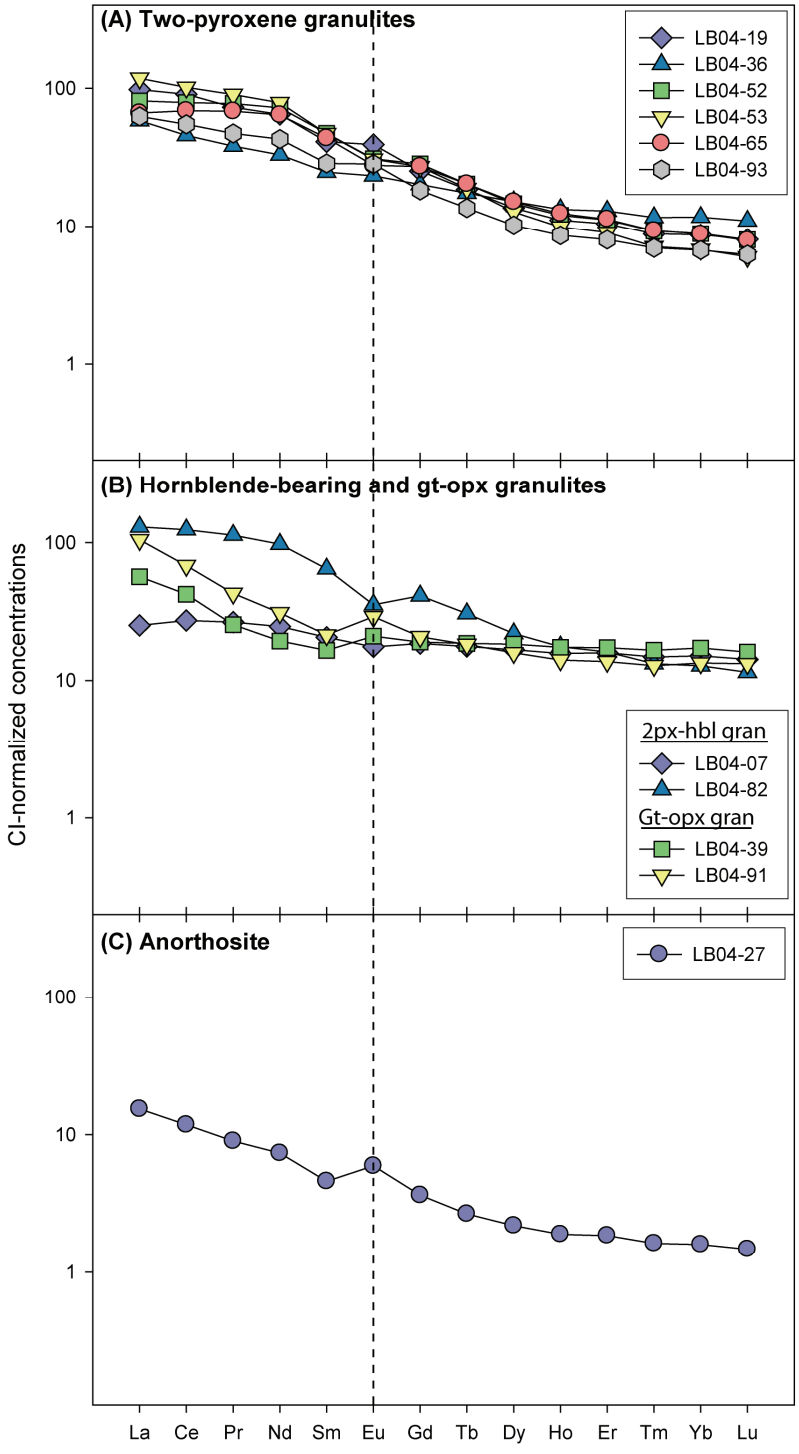

Figure 12. Chondrite-normalized rare-earth element plot for the Labait granulite xenoliths. Normalizing values from McDonough and Sun (1995).

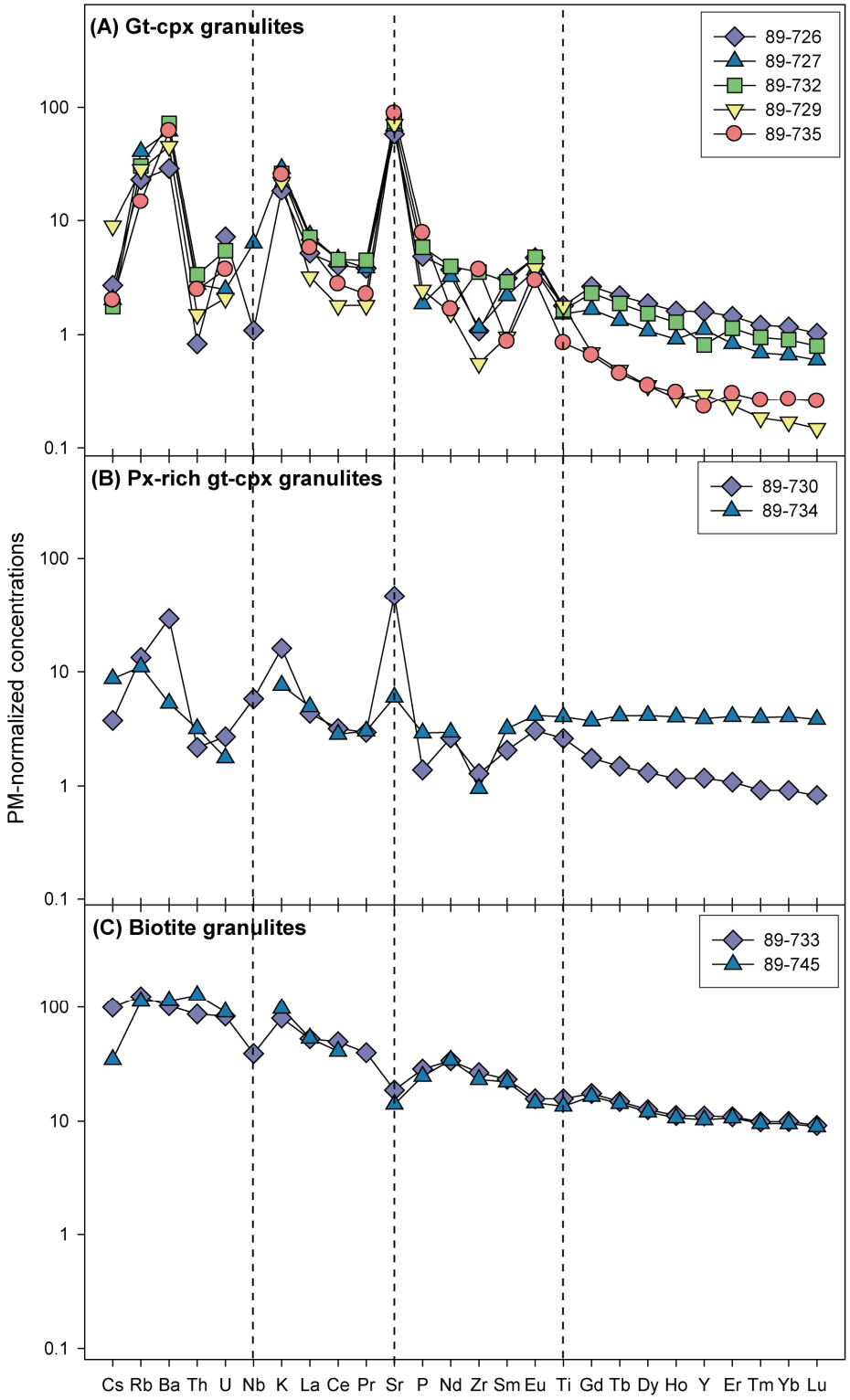

Figure 13. Primitive-mantle-normalized trace element plot for the Lashaine granulite xenoliths. Normalizing values from McDonough and Sun (1995).

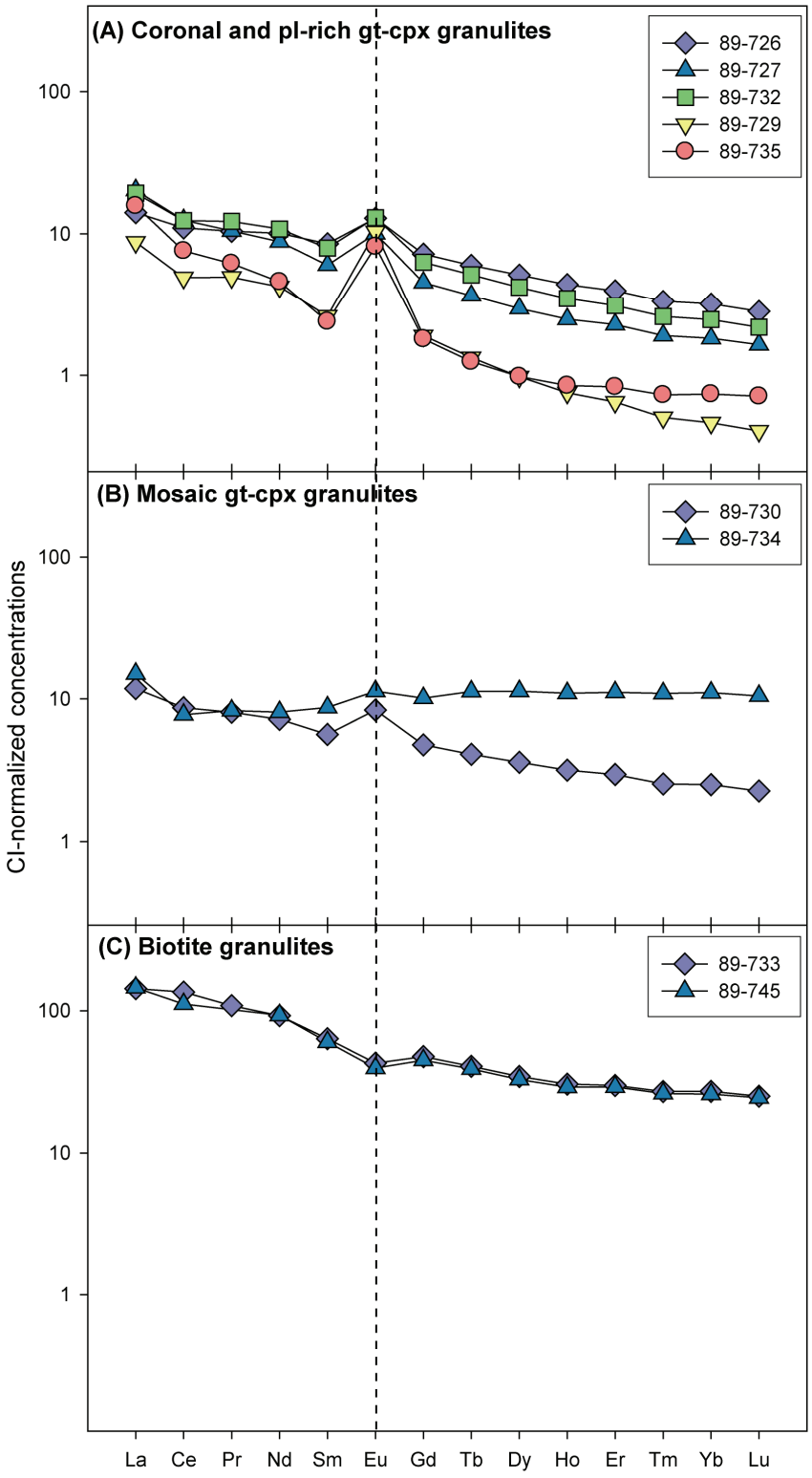

Figure 14. Chondrite-normalized rare-earth element plot for the Lashaine granulite xenoliths. Normalizing values from McDonough and Sun (1995).

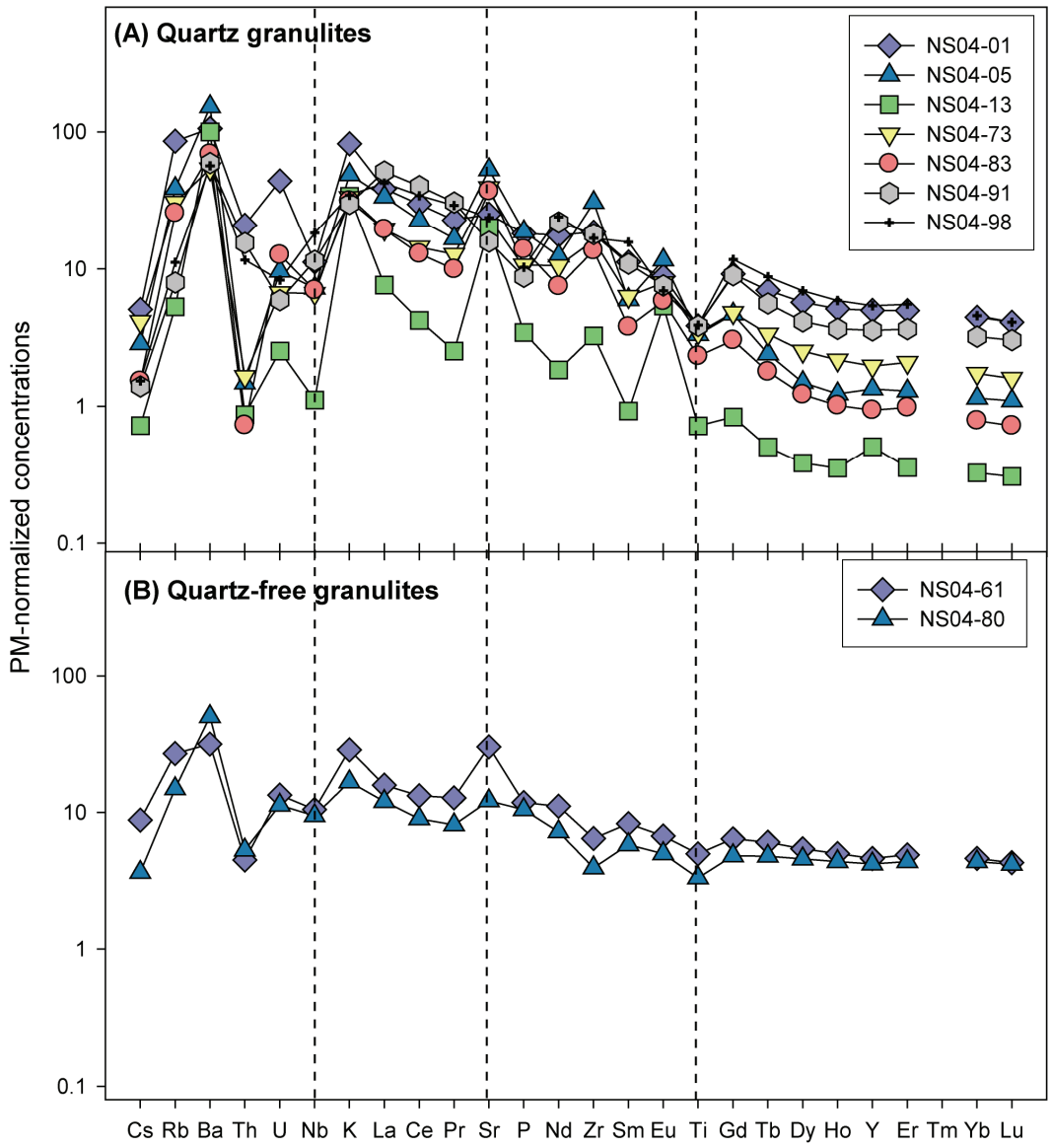

Figure 15. Primitive-mantle-normalized trace element plot for the Naibor Soito granulite xenoliths. Normalizing values from McDonough and Sun (1995).

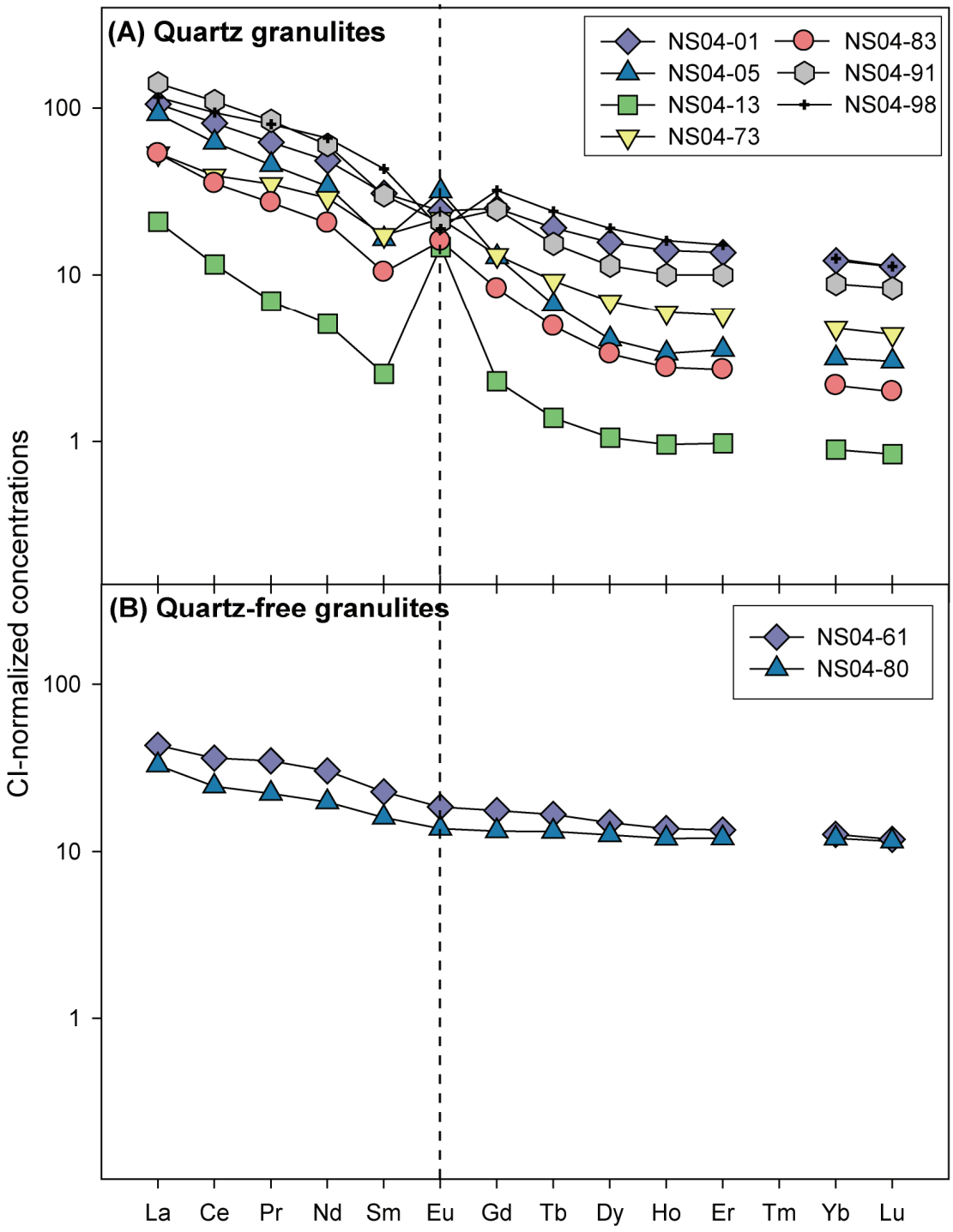

Figure 16. Chondrite-normalized rare-earth element plot for the Naibor Soito granulite xenoliths. Normalizing values from McDonough and Sun (1995).

4.5 Isotope Geochemistry

4.5.1 Labait

Nd isotope ratios were measured in each type of Labait metagabbro xenolith. Values for $^{143}Nd/^{144}Nd$ in the six analyzed meta-gabbroic xenoliths range from 0.511589 to 0.512222 (ε_{Nd} = -24.1 to -8.1) and correlate with $^{147}Sm/^{144}Nd$ (Table 12, Fig. 17a). On a Nd isochron plot the metagabbros plot below a ca. 2660 Ma isochron (Fig. 17a). Most samples have T_{DM} ages of 2.9-3.0 Ga, except LB04-39 (3.8 Ga).

Sr isotope ratios in all Labait xenoliths are confined to a narrow range (0.7037-0.7051), consistent with generally low $^{87}Rb/^{86}Sr$ (<0.1) (Table 12, Fig. 17b and 18). Ubiquitously unradiogenic Sr suggests that the observed low Rb/Sr ratios were probably typical of these samples since crystallization. Of the most radiogenic samples ($^{87}Sr/^{86}Sr$ values ~0.705 in LB04-07, LB04-36, and LB04-39), both LB04-36 and LB04-39 have relatively high Rb contents (~70 ppm) and high $^{87}Rb/^{86}Sr$ (~0.4). These high $^{87}Rb/^{86}Sr$ ratios and relatively low $^{87}Sr/^{86}Sr$ indicate recent addition of Rb to these samples. Back-calculation of $^{87}Sr/^{86}Sr$ based on the measured $^{87}Rb/^{86}Sr$ and assuming an initial $^{87}Sr/^{86}Sr$ similar to the other Labait xenoliths suggests that Rb addition occurred <200 Ma. By contrast, the slightly elevated $^{87}Sr/^{86}Sr$ in LB04-07 is unsupported by its low $^{87}Rb/^{86}Sr$ (0.058), suggesting recent Rb loss.

4.5.2 Lashaine

Nd isotope ratios were measured in three garnet-clinopyroxene granulites and two biotite granulites from Lashaine, complementing Sr-Nd isotope data measured in six xenoliths by Cohen et al. (1984). Values for $^{143}Nd/^{144}Nd$ range from 0.511689 to

0.512288 (ε_{Nd} = -18.5 to -3.8), with the least radiogenic ratios and lowest $^{147}Sm/^{144}Nd$ observed in the biotite granulites (Table 12, Fig. 17a). $^{143}Nd/^{144}Nd$ and $^{147}Sm/^{144}Nd$ correlate weakly, and T_{DM} ages range from 1.6 to 2.9 Ga. Ranges in both $^{143}Nd/^{144}Nd$ and T_{DM} (recalculated here as described above) are similar to those measured by Cohen et al. (1984) for granulite xenoliths from this locality. Some evidence, including large scatter in the Nd isochron plot relative to the other xenolith localities considered here, suggests that the isotopic composition of the garnet-clinopyroxene granulites has been modified, perhaps by the magma that carried the xenoliths to the surface. The garnet-clinopyroxene xenoliths are particularly susceptible to such contamination because of their low Nd concentrations (2 to 5 ppm, compared to ~50 ppm Nd in the host basalt; Cohen et al., 1984).

Sr concentrations in these xenoliths are generally high compared to the host basalt (280 to 1760 ppm Sr, compared to 400 ppm Sr in host), and it is unlikely that Sr isotope ratios have been significantly affected by recent overprinting. Sr isotope ratios in the garnet-clinopyroxene granulites are uniformly unradiogenic, with $^{87}Sr/^{86}Sr$ ratios ranging from 0.70249 to 0.70406 (Table 12, Fig. 17b). $^{87}Rb/^{86}Sr$ are also low (<0.06) in all garnet-clinopyroxene granulites except 89-734, which has a high $^{87}Rb/^{86}Sr$ (0.16) and a low $^{87}Sr/^{86}Sr$ (0.70249). By contrast, the biotite granulites have much higher $^{87}Rb/^{86}Sr$ (0.57-0.68) and $^{87}Sr/^{86}Sr$ (0.71653-0.72107). Regression of the $^{87}Sr/^{86}Sr$ and $^{87}Rb/^{86}Sr$ data for the Lashaine suite yields an errorchron age of ~1.8 Ga, defined mainly by the radiogenic Sr ratios in the biotite granulites (Fig. 18).

4.5.3 Naibor Soito

Nd isotope ratios were measured in seven quartz-bearing and two quartz-free xenoliths. For the quartz granulites, $^{143}Nd/^{144}Nd$ ranges from 0.510970-0.511623 (ε_{Nd} = -32.5 to -19.8). Quartz-free granulites NS04-61 and NS04-80 have comparatively radiogenic $^{143}Nd/^{144}Nd$ (0.511873-0.512273, or -14.9 to -7.1 ε) (Table 12). $^{143}Nd/^{144}Nd$ correlates with $^{147}Sm/^{144}Nd$, and T_{DM} ages range from 2.3 to 3.2 Ga (Fig. 17a).

$^{87}Sr/^{86}Sr$ ratios are unradiogenic in most of the Naibor Soito xenoliths (0.70267-0.70546) and $^{87}Rb/^{86}Sr$ ratios are low (0.02-0.10) (Table 12, Fig. 18). However, NS04-01 has relatively radiogenic Sr (0.71106) and high $^{87}Rb/^{86}Sr$ (0.29). There is no systematic difference in isotopic compositions between the quartz and quartz-free xenoliths.

TABLE 12: Sr-Nd isotope data for selected Tanzanian xenoliths

Sample	Type	$\frac{^{87}Sr}{^{86}Sr}$		$\frac{^{87}Rb}{^{86}Sr}$	$\frac{^{143}Nd}{^{144}Nd}$		$\frac{^{147}Sm}{^{144}Nd}$	Sr (ppm)	Rb (ppm)	Nd (ppm)	Sm (ppm)	ε_{Nd} 0 Ma	ε_{Nd} 2660 Ma	T_{DM} (Ga)
Labait														
LB04-19	2px gran	0.703979	± 10	0.10	0.511452	± 7	0.133	735	25.1	26.6	5.6	-23.1	-1.3	3.0
LB04-36	2px gran	0.704797	± 99	0.41	-		-	521	74.8	-	-	-	-	-
LB04-52	2px gran	0.703909	± 14	0.067	0.511539	± 7	0.135	569	13.6	30.3	6.5	-21.4	-0.3	2.9
LB04-07	2px-hbl gran	0.705147	± 20	0.058	0.512222	± 10	0.170	524	10.8	-	-	-8.1	-	-
LB04-82	2px-hbl gran	0.704131	± 15	0.048	0.511607	± 8	0.139	969	16.5	44.2	9.8	-20.1	-0.3	3.0
LB04-39	Gt-opx gran	0.704834	± 12	0.39	0.512081	± 6	0.173	504	69.4	9.8	2.7	-10.9	-2.7	3.8
LB04-91	Gt-opx gran	0.703987	± 12	0.092	0.511683	± 6	0.143	847	27.6	14.1	3.2	-18.6	-0.4	3.0
Lashaine														
89-733	Bt gran	0.716532	± 16	0.57	0.511689	± 7	0.140	371	74.6	-	-	-18.5	-	-
89-745	Bt gran	0.721067	± 23	0.68	0.511761	± 9	0.145	281	67.4	37.3	8.6	-17.1	+0.7	2.9
89-726	Gt-cpx gran	0.704055	± 42	0.034	0.512288	± 38	0.172	1160	13.9	-	-	-6.8	-	-
89-727	Gt-cpx gran	0.704002	± 20	0.051	-		-	1365	24.5	-	-	-	-	-
89-729	Gt-cpx gran	0.703665	± 17	0.034	0.51170	± 18	0.127	1417	17.1	-	-	-18.4	-	-
89-730	Gt-cpx gran	0.703834	± 12	0.024	0.512445	± 72	0.158	927	8.0	-	-	-3.8	-	-
89-734	Gt-cpx gran	0.70249	± 12	0.16	-		-	119	6.6	-	-	-	-	-
89-735	Gt-cpx gran	0.704200	± 18	0.014	-		-	1760	8.8	-	-	-	-	-
Naibor Soito														
NS04-01	Qtz gran	0.711056	± 27	0.29	0.511311	± 17	0.130	503	51.3	-	-	-25.9	-	-
NS04-05	Qtz gran	0.702671	± 12	0.073	0.510970	± 9	0.097	896	23.2	12.8	2.0	-32.5	+1.4	2.7
NS04-13	Qtz gran	0.705456	± 11	0.024	0.511328	± 29	0.102	371	3.2	2.4	0.38	-25.6	+7.0	2.3
NS04-73	Qtz gran	-		-	0.511254	± 20	0.122	-	-	-	-	-27.0	-	-
NS04-83	Qtz gran	0.703268	± 18	0.075	0.511078	± 10	0.102	692	18.5	7.8	1.3	-30.4	+3.1	2.7
NS04-91	Qtz gran	0.705486	± 13	0.044	0.511042	± 8	0.104	308	4.8	24.3	4.0	-31.1	+1.9	2.8
NS04-98	Qtz gran	-		-	0.511623	± 6	0.133	-	-	-	-	-19.8	+0.7	2.7
NS04-150	Qtz-free gran	0.703028	± 17	0.062			-	1146	25.0	-	-	-	-	-
NS04-61	Qtz-free gran	0.703837	± 20	0.075	0.511873	± 8	0.156	603	16.1	12.2	3.0	-14.9	-0.9	3.1
NS04-80	Qtz-free gran	0.703231	± 20	0.10	0.512273	± 11	0.167	246	8.9	7.9	2.1	-7.1	+3.1	2.5

Notes: Underlined values from XRF (Rb, Sr). All other values measured via isotope dilution. Errors on isotope ratios are 2x standard error of the mean. T_{DM} calculated based on depleted-mantle curve of DePaolo (1981). Values in parentheses represent analytical error.

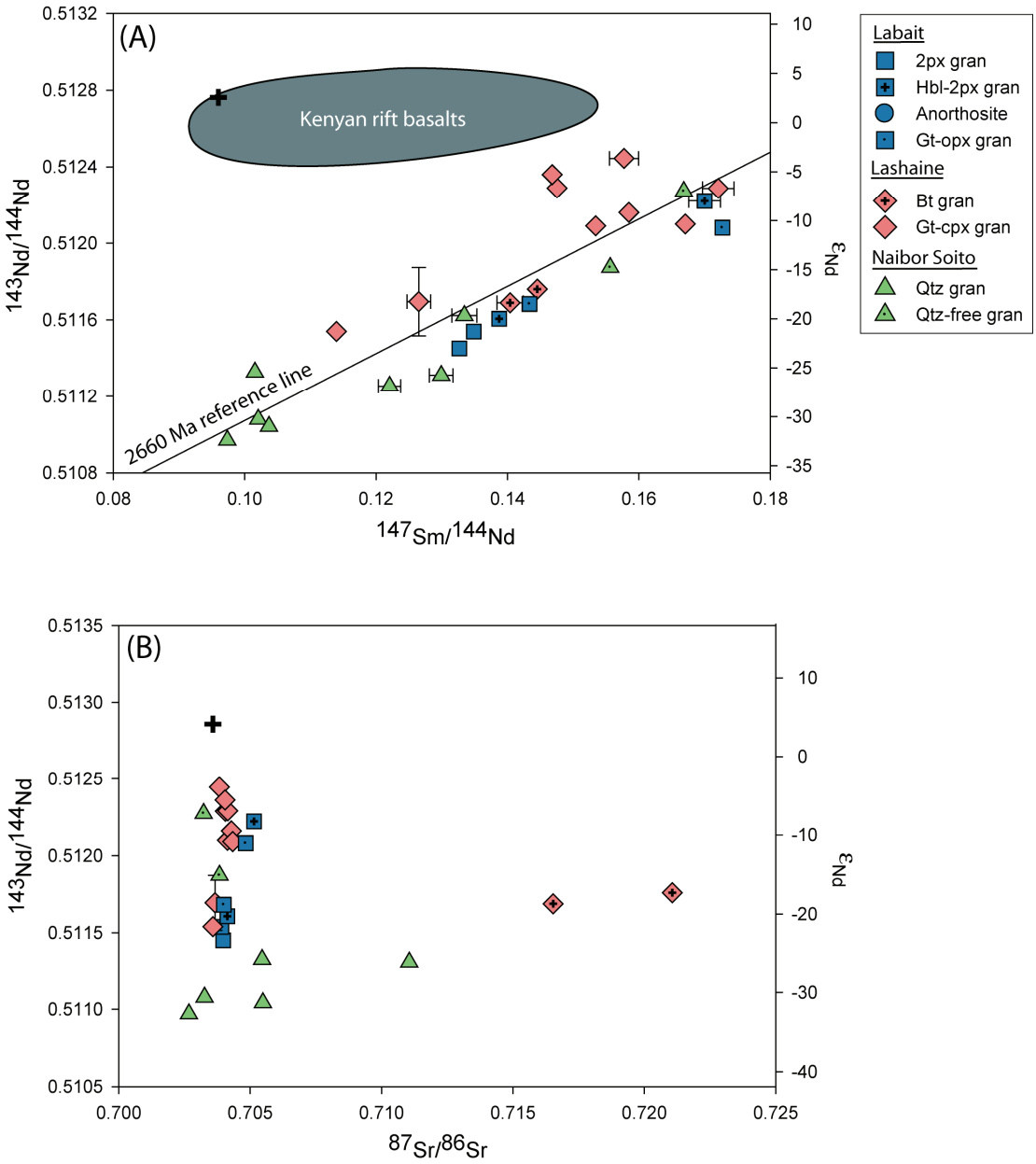

Figure 17. Nd and Sr isotope plots for the Tanzanian crustal xenoliths, including data for the Lashaine gt-cpx granulites from Cohen et al. (1984). Cross shows the composition of the Lashaine ankaramite (Cohen et al., 1984). Reference isochron in (a) is calculated for an age of 2660 Ma and an initial ε_{Nd} of +2.3, corresponding the composition of the depleted mantle of DePaolo (1981) at this time. Kenyan rift field based on data from MacDonald et al. (2001).

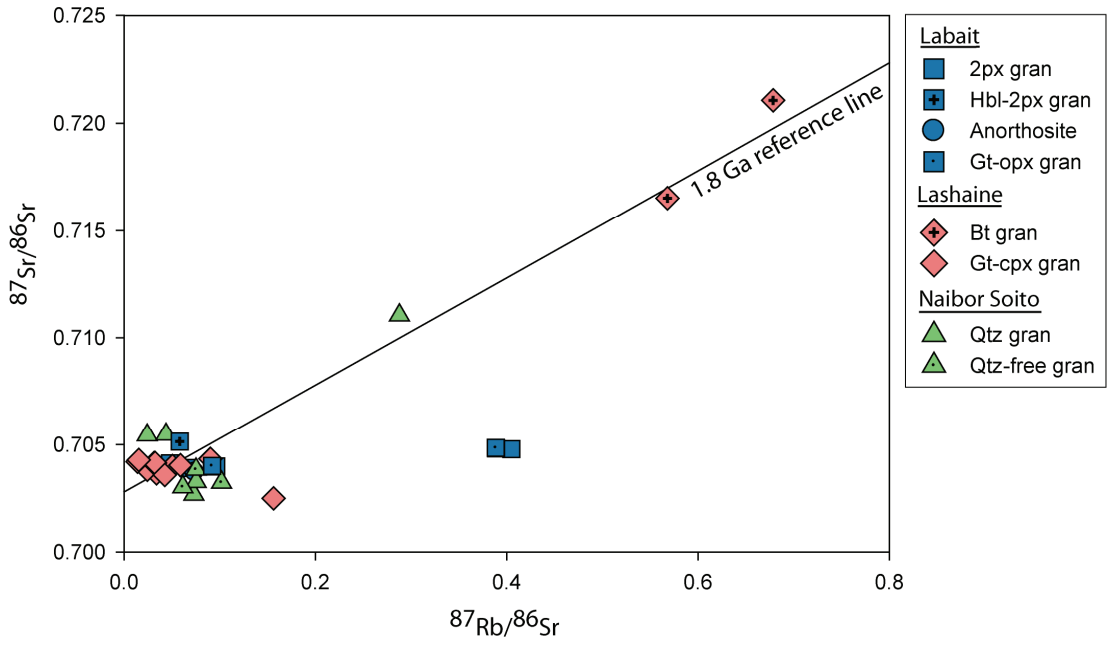

Figure 18. Sr isochron plot for the Tanzanian lower crustal xenoliths. Calculated using Isoplot/EX, v.3.00 (Ludwig, 1998).

4.6 Zircon Geochronology

Zircon U-Pb ratios and ages are summarized for the Labait and Naibor Soito xenoliths in Table 13 and Figs. 19-24; no zircons from Lashaine have been dated, although small zircons have been observed in the biotite granulites. Because the laser ablation method used here does not allow calculation of concentrations, I have also included the average number of counts per second measured during ablation for masses 202 (Hg), 204 (Hg, Pb), 206 (Pb), 207 (Pb), and 238 (U) in Table 13. These data give a qualitative sense of the differences in concentrations between samples, but are imperfect in that (1) they do not address changes in sensitivity between analytical sessions and (2) they obscure significant changes in signal strength during ablation, for example, its tendency to decrease over time and its sensitivity to internal zoning.

Because the samples considered here date from the Archean, $^{207}Pb/^{206}Pb$ ratios provide the best estimate of ages. Where Pb/U ratios are reliable, concordant ages or concordia plots have also been calculated using ISOPLOT/EX, v.3.00 (Ludwig, 1998). Concordant ages were calculated for all zircons which were discordant by <2%. In zircons with significant lead loss, $^{207}Pb/^{206}Pb$ ages skew to younger ages. Spot analyses from NS04-05 suggest that this effect is pronounced only in grains that are more than 10% discordant. These are excluded without comment from the ranges of the ages presented below, but are included in Table 13 and Figs. 19-24. Pb/U ratios could not be calculated for all analyses, particularly for zircons in Labait having very low U contents, and concordance cannot be addressed in these grains. However, $^{207}Pb/^{206}Pb$ ratios in the Labait zircons are similar in most zircons in each sample, suggesting that lead loss in these zircons has been minor. All errors quoted below are 2σ.

4.6.1 Labait

LB04-19 (two-pyroxene granulite): Zircons from this sample are spherical or less commonly oblate, with aspect ratios near one and diameters typically <200 μm. Internal zoning is present in approximately one-third of the zircons imaged using CL. The most common structure consists of a dark, polygonal core (~50 μm) surrounded by (a) ~20-40 μm wide bands of alternating light and dark gray or (b) featureless rims. A few zircons preserve broad, oscillatory zones or well-developed sector zoning, suggesting that zircons of both igneous and metamorphic origin are present. Cores displaying these textures are typically surrounded by 10-40 μm thick, featureless rims. Because of the rarity of the zoned crystals, the difficulty in obtaining reliable Pb/U ratios in U-poor zircons using the method employed here, and the destructive nature of laser analyses, I chose to analyze only homogenous zircons from this sample (Fig. 19). However, high U counts in zoned zircons from other Labait samples suggest that these crystals are probably viable targets for laser ablation.

U concentrations in the Labait zircons are low relative to the Naibor Soito zircons, consistent with the low whole-rock U concentrations at Labait (0.03-0.26 ppm) relative to Naibor Soito (0.05-0.89 ppm). Most analyses did not produce sufficient counts of ^{238}U to calculate reliable Pb/U ratios. Four concordant or near-concordant analyses give a pooled age of 2679±44 Ma (Table 13, Fig. 22a). $^{207}Pb/^{206}Pb$ ages are similar, with a prominent peak around 2680 Ma (Fig. 24a). Examination of individual zircons suggests that the total range of $^{207}Pb/^{206}Pb$ ages observed for this sample (2575-2733 Ma) may have been skewed to lower ages as a result of lead loss, possibly during transport from the lower

crust. For example, the youngest $^{207}Pb/^{206}Pb$ age for a zircon in this sample (2575±77 Ma) was one of two spots measured in crystal 11.The second spot, from a visually identical portion of the zircon, gives an older mean age (2709±84 Ma) more typical of this sample (Fig. 19). A similar comparison can be made between multiple spots on zircons 6 and 15, although in these grains the individual analyses overlap within error. On the other hand, two spots apiece on zircons 5 and 19 give effectively identical ages (ca. 2700 and 2680 Ma, respectively).

LB-48 (two-pyroxene granulite): Zircons from LB-48 are similar in morphology and size to those from LB04-19 (Fig. 19). Most imaged zircons are featureless or preserve only broad internal zoning, for example, cores of uniform texture surrounded by featureless rims. A small number of zircons contain cores (30-50 μm in diameter) that are relatively bright in CL, display oscillatory zoning, and have high concentrations of ^{238}U. In contrast, the rims of these crystals are extremely depleted in U, resulting in large errors on rim analyses for crystals 42 and 49.

As in the previous sample, low U concentrations hampered the calculation of Pb/U ratios, and only seven analyses had sufficient counts to calculate these ratios. Four of these were analyses of the bright domains described above. Analysis of this material in four separate crystals gives concordant ages ranging from 2646 to 2684 Ma. A pooled concordant age for all seven of these analyses gives an age of 2649±21 Ma (Fig. 22b). $^{207}Pb/^{206}Pb$ ages peak at a similar time (Fig. 24a).

4.6.2 Naibor Soito

NS04-05 (quartz granulite): In contrast to zircons from the Labait xenoliths,

zircons from this sample are almost always prismatic with rounded terminations (Fig. 20). Most crystals are 200-500 μm long and 100-200 μm wide, with aspect ratios between 2 and 3. (One exceptional crystal from this sample was 900 μm long, making it by far the largest zircon encountered in this study.) Despite morphologies consistent with an igneous origin, internal zoning visible in CL is rare and, where present, subtle, suggesting that zoning does not reflect large compositional differences. Distinct cores and rims are absent, save for a handful of crystals with dark polygonal or rod-shaped domains similar to those observed in LB04-19.

Zircons from Naibor Soito have high U concentrations relative to the Labait zircons, allowing Pb/U ratios to be calculated for most crystals. A large fraction of these crystals are >2% discordant, but 13 concordant spots from this sample give ages ranging from 2528-2711 Ma. $^{207}Pb/^{206}Pb$ ages define nearly an identical range (2504-2711 Ma), with a distinct peak around 2650 Ma. Among grains that display internal zoning, ages from different domains overlap. An exception to this rule is the dark material noted in crystals 17, 35, and 36, which gives young ages relative to the surrounding zircon. For crystals 17 and 35, these low apparent ages can be attributed Pb loss and discordance.

Multiple spots were measured for two large, homogenous zircons (3 and 7), producing several concordant and discordant analyses for each zircon. Analyses from zircon 3 plot on a discordia with an upper intercept of 2653±37 Ma and a lower intercept of 604±140 Ma, whereas analyses from zircon 7 give an upper intercept of 2643±48 Ma and a lower intercept of 601±220 Ma. These compare well with upper and lower intercept ages calculated using all analyses for this sample (2656±14 and 594±63 Ma, respectively) (Fig. 23a) The upper intercepts of these discordia are similar to $^{207}Pb/^{206}Pb$ ages from this

sample, and the lower intercepts correspond broadly to the timing of metamorphism in the Mozambique Belt.

NS04-91 (quartz granulite): Most zircons from this sample are spherical, with diameters of 100-250 μm, but a significant fraction are prismatic with similar dimensions to those from NS04-05 (Fig. 21). Internal zoning within both morphologies is common, including both minor gradations similar to those in the previous sample and distinct core-rim relationships, and, unlike the previous sample, differences between core and rim $^{207}Pb/^{206}Pb$ ages are sometimes preserved.

$^{207}Pb/^{206}Pb$ ages of zircons in NS04-91 cluster in two broad groups, one that ranges from 2750-2800 Ma, the other from 2550-2675 Ma (Fig. 24b). Concordant ages define similar ranges. The ca. 2800 Ma spots are rare and occur almost exclusively in zircon cores, whereas the younger ages are not restricted to a given crystal domain or structure and are more prevalent overall. Three types of core-rim relationships corresponding to domains visible in CL are preserved: (1) ca. 2800 Ma, bright, prismatic cores surrounded by 2620-2680 Ma rims (as in crystals 12, 19, 21, and 26); (2) a ca. 2630 Ma core surrounded by a 2540-2570 Ma rim (crystal 3); and (3) a ca. 2630 Ma core surrounded by a rim of identical age (crystal 29). Crystals younger than ca. 2800 Ma may be prismatic, oblate, or spherical. A U-Pb concordia plot for the ca. 2650 Ma zircons gives an upper intercept age of 2640±25 Ma and a lower intercept age of 716±350 Ma, comparable to concordia intercept ages in NS04-05 (Fig. 23b).

W3S-2 (quartz granulite): Zircons from this sample are mostly round to oblate, commonly unzoned, but sometimes contain dark, polygonal crystal cores (Fig. 19). Zircon ages are available for only two zircons from this sample. (Additional zircons from

W3S-2 were analyzed using laser ablation at UMCP and by S. Timpa using TIMS at Sam Bowring's laboratory at MIT. The laser ablation analyses for these zircons could not be processed and are not reported here).

Analyses from two zircons (11 and 13) give concordant ages of 2636±29 Ma and 2629±22 Ma. The latter analysis is of the dark, polygonal core in crystal 13, whose rim gives a somewhat younger, moderately discordant $^{207}Pb/^{206}Pb$ age (2572±25 Ma). The significance of this younger age is unclear, but the concordant ages are within uncertainty of a U-Pb upper intercept age (2655±4 Ma) measured for a multi-zircon separate from this sample using TIMS (S. Timpa, unpublished data).

TABLE 13: Laser ablation U-Pb analyses of zircons from Tanzanian granulite xenoliths

Sample	spot	$\frac{^{207}Pb}{^{235}U}$	$\frac{^{206}Pb}{^{238}U}$	$\frac{^{207}Pb}{^{206}Pb}$	Ages (Ma) $\frac{^{207}Pb}{^{235}U}$	Ages (Ma) $\frac{^{206}Pb}{^{238}U}$	Ages (Ma) $\frac{^{206}Pb}{^{207}Pb}$	Conc. age	% disc	cps 202	cps 204	kcps 206	kcps 207	kcps 238
Labait														
LB04-19	3.1	12.94 ± 0.74	0.495 ± 0.025	0.1894 ± 0.0045	2675 ± 53	2594 ± 108	2737 ± 39	- -	3.5%	66	7	76	14	160
LB04-19	3.2	12.58 ± 0.73	0.500 ± 0.026	0.1823 ± 0.0045	2649 ± 54	2616 ± 109	2674 ± 41	2668 ± 39	conc.	71	24	80	14	167
LB04-19	5.1	- -	- -	0.1856 ± 0.0059	- -	- -	2704 ± 52	- -	-	61	4	20	4	51
LB04-19	5.2	- -	- -	0.1857 ± 0.0058	- -	- -	2705 ± 51	- -	-	46	19	19	3	50
LB04-19	6.1	- -	- -	0.1857 ± 0.0077	- -	- -	2704 ± 68	- -	-	49	15	9	2	34
LB04-19	6.2	- -	- -	0.1760 ± 0.0073	- -	- -	2616 ± 68	- -	-	-15	5	9	2	34
LB04-19	7.1	- -	- -	0.1858 ± 0.0060	- -	- -	2705 ± 53	- -	-	-22	2	16	3	44
LB04-19	7.2	- -	- -	0.1791 ± 0.0067	- -	- -	2644 ± 62	- -	-	38	23	11	2	37
LB04-19	11.1	- -	- -	0.1717 ± 0.0080	- -	- -	2575 ± 77	- -	-	22	7	6	1	31
LB04-19	11.2	- -	- -	0.1862 ± 0.0096	- -	- -	2709 ± 84	- -	-	66	19	6	1	31
LB04-19	15.1	- -	- -	0.1803 ± 0.0070	- -	- -	2655 ± 63	- -	-	46	19	10	2	35
LB04-19	15.2	- -	- -	0.1889 ± 0.0083	- -	- -	2733 ± 71	- -	-	18	19	9	2	35
LB04-19	17	12.44 ± 0.92	0.494 ± 0.035	0.1828 ± 0.0038	2639 ± 69	2587 ± 151	2678 ± 34	2674 ± 33	0.6%	-895	-214	282	51	618
LB04-19	19.1	- -	- -	0.1834 ± 0.0093	- -	- -	2684 ± 83	- -	-	34	-12	10	2	36
LB04-19	19.2	- -	- -	0.1830 ± 0.0088	- -	- -	2680 ± 79	- -	-	28	6	15	3	46
LB04-19	20.1	- -	- -	0.185 ± 0.011	- -	- -	2696 ± 95	- -	-	47	159	6	1	31
LB04-19	21.1	12.15 ± 0.80	0.482 ± 0.022	0.1829 ± 0.0079	2616 ± 61	2535 ± 97	2680 ± 71	- -	3.4%	86	79	45	8	114
LB04-19	25	- -	- -	0.1874 ± 0.0091	- -	- -	2720 ± 79	- -	-	117	26	13	2	43
LB04-27	4.1	- -	- -	0.1716 ± 0.0047	- -	- -	2573 ± 45	- -	-	29	9	20	3	56
LB48	33.1	12.96 ± 0.70	0.516 ± 0.023	0.1821 ± 0.0049	2677 ± 50	2682 ± 99	2672 ± 45	2674 ± 42	conc.	94	14	59	11	128
LB48	33.2	- -	- -	0.1853 ± 0.0070	- -	- -	2701 ± 61	- -	-	35	27	32	6	70
LB48	40.1	11.78 ± 0.60	0.480 ± 0.022	0.1779 ± 0.0035	2587 ± 47	2529 ± 95	2633 ± 32	- -	2.6%	380	99	301	53	725
LB48	42.1	12.74 ± 0.68	0.502 ± 0.024	0.1840 ± 0.0039	2660 ± 50	2621 ± 104	2690 ± 34	2684 ± 33	0.5%	130	53	115	21	252
LB48	42.2	- -	- -	0.220 ± 0.021	- -	- -	2981 ± 151	- -	-	46	10	1	0	26
LB48	43.1	12.93 ± 0.61	0.512 ± 0.019	0.1830 ± 0.0047	2675 ± 44	2667 ± 83	2680 ± 42	2678 ± 39	conc.	46	12	122	22	272
LB48	49.1	12.13 ± 0.65	0.488 ± 0.024	0.1802 ± 0.0038	2614 ± 49	2562 ± 102	2655 ± 35	2646 ± 33	1.8%	180	62	148	26	336
LB48	49.2	- -	- -	0.1966 ± 0.0181	- -	- -	2798 ± 146	- -	-	172	51	2	0	26
LB-48	29.1	- -	- -	0.1791 ± 0.0052	- -	- -	2644 ± 48	- -	-	586	146	32	6	51

TABLE 13: Laser ablation U-Pb analyses of zircons from Tanzanian granulite xenoliths (cont.)

Sample	spot	$^{207}Pb/^{235}U$	$^{206}Pb/^{238}U$	$^{207}Pb/^{206}Pb$	Ages (Ma) $^{207}Pb/^{235}U$	Ages (Ma) $^{206}Pb/^{238}U$	Ages (Ma) $^{206}Pb/^{207}Pb$	Conc. age	% disc	cps 202	cps 204	kcps 206	kcps 207	kcps 238
Labait (cont.)														
LB-48	29.2	12.70 ± 0.49	0.520 ± 0.016	0.1771 ± 0.0035	2657 ± 36	2698 ± 66	2626 ± 33	- -	1.5%	385	84	185	32	360
LB-48	29.3	- -	- -	0.1804 ± 0.0046	- -	- -	2657 ± 42	- -	-	330	82	75	13	127
LB-48	31.1	- -	- -	0.1846 ± 0.0113	- -	- -	2695 ± 100	- -	-	422	52	6	1	19
LB-48	31.2	- -	- -	0.1741 ± 0.0097	- -	- -	2597 ± 92	- -	-	495	98	7	1	20
LB-48	34	- -	- -	0.1866 ± 0.0075	- -	- -	2712 ± 66	- -	-	393	117	10	2	26
LB-48	36	12.10 ± 0.59	0.491 ± 0.022	0.1788 ± 0.0029	2612 ± 45	2574 ± 94	2642 ± 27	2638 ± 27	0.9%	1197	298	464	82	889
LB-48	45	- -	- -	0.1836 ± 0.0073	- -	- -	2686 ± 65	- -	-	725	175	11	2	25
LB-48	50.1	- -	- -	0.1804 ± 0.0042	- -	- -	2656 ± 39	- -	-	698	204	100	18	158
LB-48	50.2	- -	- -	0.1840 ± 0.0031	- -	- -	2689 ± 28	- -	-	653	181	339	62	757
									-					
Naibor Soito									-					
NS04-05	1.1	10.94 ± 0.92	0.452 ± 0.024	0.1756 ± 0.0089	2518 ± 76	2403 ± 105	2612 ± 83	- -	5.8%	287	111	848	146	1893
NS04-05	1.2	12.34 ± 1.04	0.480 ± 0.025	0.1864 ± 0.0096	2631 ± 78	2528 ± 110	2710 ± 83	- -	4.2%	250	81	185	34	392
NS04-05	1.3	- -	- -	0.1722 ± 0.0090	- -	- -	2579 ± 86	- -	-	250	29	72	12	160
NS04-05	2	4.39 ± 0.34	0.221 ± 0.009	0.1437 ± 0.0076	1710 ± 64	1289 ± 49	2272 ± 90	- -	46%	381	107	26	4	106
NS04-05	2.1	12.59 ± 1.04	0.494 ± 0.025	0.1847 ± 0.0094	2649 ± 76	2589 ± 108	2696 ± 83	2661 ± 76	0.8%	242	50	457	83	919
NS04-05	2.2	11.7 ± 1.1	0.488 ± 0.046	0.1738 ± 0.0025	2580 ± 87	2560 ± 196	2594 ± 24	2595 ± 24	conc.	283	33	183	32	392
NS04-05	2.3	12.9 ± 1.2	0.524 ± 0.049	0.1779 ± 0.0026	2670 ± 88	2718 ± 207	2633 ± 25	2635 ± 26	conc.	223	49	165	29	330
NS04-05	2.4	12.2 ± 1.2	0.493 ± 0.046	0.1790 ± 0.0023	2617 ± 87	2583 ± 197	2644 ± 21	2644 ± 22	conc.	387	76	483	87	994
NS04-05	3.1	- -	- -	0.1647 ± 0.0020	- -	- -	2504 ± 20	- -	-	148	84	2966	491	9194
NS04-05	3.2	8.86 ± 0.85	0.377 ± 0.035	0.1703 ± 0.0025	2323 ± 86	2062 ± 165	2560 ± 24	- -	19%	197	65	176	30	488
NS04-05	3.3	11.28 ± 0.56	0.460 ± 0.012	0.1779 ± 0.0064	2547 ± 46	2439 ± 54	2633 ± 59	- -	6.7%	371	187	96	17	229
NS04-05	3.4	6.23 ± 0.28	0.285 ± 0.005	0.1586 ± 0.0055	2009 ± 40	1617 ± 27	2440 ± 58	- -	37%	400	72	267	42	1115
NS04-05	3.5	11.70 ± 0.54	0.473 ± 0.010	0.1795 ± 0.0062	2580 ± 43	2495 ± 42	2648 ± 57	- -	4.7%	381	116	260	46	586
NS04-05	3.6	12.03 ± 0.58	0.491 ± 0.012	0.1776 ± 0.0063	2607 ± 45	2576 ± 50	2630 ± 59	2596 ± 44	0.3%	325	70	108	19	247
NS04-05	3.7	8.02 ± 0.32	0.352 ± 0.009	0.1653 ± 0.0042	2233 ± 35	1944 ± 45	2511 ± 43	- -	25%	409	92	139	23	458
NS04-05	4.1	11.50 ± 0.55	0.464 ± 0.011	0.1796 ± 0.0062	2565 ± 44	2459 ± 48	2649 ± 57	- -	6.5%	313	106	642	115	1583

TABLE 13: Laser ablation U-Pb analyses of zircons from Tanzanian granulite xenoliths (cont.)

Sample	spot	$^{207}Pb/^{235}U$	$^{206}Pb/^{238}U$	$^{207}Pb/^{206}Pb$	Ages (Ma) $^{207}Pb/^{235}U$	Ages (Ma) $^{206}Pb/^{238}U$	Ages (Ma) $^{206}Pb/^{207}Pb$	Conc. age	% disc	cps 202	cps 204	kcps 206	kcps 207	kcps 238
Naibor Soito (cont.)														
NS04-05	7.1	12.36 ± 0.45	0.498 ± 0.014	0.1799 ± 0.0036	2632 ± 34	2607 ± 59	2652 ± 33	2642 ± 31	0.2%	188	23	296	52	677
NS04-05	7.2	10.99 ± 0.41	0.463 ± 0.014	0.1722 ± 0.0034	2523 ± 35	2453 ± 60	2579 ± 33	- -	4.2%	222	49	366	62	847
NS04-05	7.3	8.33 ± 0.31	0.365 ± 0.011	0.1656 ± 0.0033	2267 ± 34	2004 ± 51	2513 ± 33	- -	22%	223	67	418	68	1123
NS04-05	7.4	8.68 ± 0.33	0.370 ± 0.011	0.1700 ± 0.0035	2305 ± 35	2031 ± 53	2557 ± 34	- -	22%	76	20	185	31	539
NS04-05	7.5	10.85 ± 0.40	0.443 ± 0.013	0.1775 ± 0.0035	2510 ± 34	2365 ± 57	2629 ± 32	- -	10%	445	120	735	128	1923
NS04-05	7.6	4.41 ± 0.17	0.223 ± 0.007	0.1435 ± 0.0033	1715 ± 32	1298 ± 35	2270 ± 39	- -	46%	73	27	79	11	406
NS04-05	9.1	12.43 ± 0.47	0.499 ± 0.013	0.1806 ± 0.0044	2638 ± 36	2611 ± 55	2658 ± 40	2643 ± 35	0.5%	330	97	318	57	711
NS04-05	9.2	12.57 ± 0.47	0.494 ± 0.012	0.1846 ± 0.0045	2648 ± 35	2587 ± 52	2695 ± 40	- -	3.1%	299	87	483	89	1104
NS04-05	10	12.80 ± 0.92	0.499 ± 0.017	0.1861 ± 0.0094	2665 ± 67	2608 ± 71	2708 ± 82	- -	1.0%	404	106	97	18	196
NS04-05	11.1	12.84 ± 0.41	0.515 ± 0.008	0.1810 ± 0.0041	2668 ± 30	2677 ± 35	2662 ± 37	2670 ± 30	conc.	176	38	511	92	1089
NS04-05	11.2	9.19 ± 0.31	0.404 ± 0.008	0.1651 ± 0.0039	2358 ± 31	2187 ± 35	2508 ± 40	- -	14%	147	23	147	24	392
NS04-05	13.1	- -	- -	0.1806 ± 0.0043	- -	- -	2659 ± 39	- -	-	235	73	6677	1204	16181
NS04-05	13.2	12.33 ± 0.46	0.491 ± 0.012	0.1823 ± 0.0044	2630 ± 35	2573 ± 52	2674 ± 40	- -	2.9%	254	73	490	89	1110
NS04-05	15	8.46 ± 0.33	0.355 ± 0.007	0.1730 ± 0.0045	2281 ± 35	1956 ± 32	2586 ± 43	- -	27%	1864	437	841	146	2391
NS04-05	16.1	14.16 ± 0.46	0.548 ± 0.016	0.1873 ± 0.0026	2760 ± 31	2817 ± 66	2719 ± 23	- -	2.6%	239	73	276	51	566
NS04-05	16.2	13.62 ± 0.44	0.531 ± 0.015	0.1859 ± 0.0025	2724 ± 30	2747 ± 64	2706 ± 22	2711 ± 22	0.4%	309	49	463	85	976
NS04-05	17.1	9.68 ± 0.30	0.415 ± 0.006	0.1693 ± 0.0038	2405 ± 29	2236 ± 29	2551 ± 37	- -	13%	226	52	2134	359	5745
NS04-05	17.2	12.28 ± 0.39	0.500 ± 0.008	0.1781 ± 0.0041	2626 ± 30	2613 ± 35	2635 ± 38	2623 ± 30	conc.	139	53	445	79	964
NS04-05	19.1	12.64 ± 0.42	0.499 ± 0.015	0.1835 ± 0.0025	2653 ± 31	2612 ± 63	2685 ± 23	- -	1.7%	283	85	350	64	748
NS04-05	19.2	12.73 ± 0.42	0.503 ± 0.015	0.1836 ± 0.0025	2660 ± 31	2626 ± 63	2685 ± 23	2679 ± 22	1.2%	268	104	370	67	799
NS04-05	28.1	11.82 ± 0.47	0.475 ± 0.017	0.1803 ± 0.0025	2590 ± 37	2507 ± 76	2656 ± 23	- -	4.8%	205	80	362	65	818
NS04-05	28.2	10.79 ± 0.58	0.443 ± 0.023	0.1766 ± 0.0033	2505 ± 50	2364 ± 101	2621 ± 31	- -	9.2%	196	30	87	15	214
NS04-05	28a.1	10.23 ± 0.39	0.419 ± 0.007	0.1772 ± 0.0048	2456 ± 35	2254 ± 32	2627 ± 44	- -	15%	295	63	238	42	564
NS04-05	28a.2	- -	- -	0.1798 ± 0.0048	- -	- -	2651 ± 44	- -	-	355	111	402	73	573
NS04-05	29	10.47 ± 0.38	0.435 ± 0.006	0.1747 ± 0.0046	2478 ± 34	2327 ± 28	2604 ± 43	- -	11%	329	58	482	85	1175
NS04-05	29.1	12.86 ± 0.58	0.519 ± 0.022	0.1795 ± 0.0027	2669 ± 42	2697 ± 93	2649 ± 25	2653 ± 26	conc.	220	55	95	17	211
NS04-05	29.3	- -	- -	0.1768 ± 0.0023	- -	- -	2623 ± 21	- -	-	165	71	285	50	740
NS04-05	30	- -	- -	0.1790 ± 0.0048	- -	- -	2644 ± 44	- -	-	368	118	328	59	711

TABLE 13: Laser ablation U-Pb analyses of zircons from Tanzanian granulite xenoliths (cont.)

Sample	spot	$^{207}Pb/^{235}U$	$^{206}Pb/^{238}U$	$^{207}Pb/^{206}Pb$	Ages (Ma) $^{207}Pb/^{235}U$	Ages (Ma) $^{206}Pb/^{238}U$	Ages (Ma) $^{206}Pb/^{207}Pb$	Conc. age	% disc	cps 202	cps 204	kcps 206	kcps 207	kcps 238
Naibor Soito (cont.)														
NS04-05	32.1	11.66 ± 0.77	0.485 ± 0.010	0.1745 ± 0.0085	2577 ± 61	2547 ± 42	2601 ± 80	2528 ± 37	conc.	272	57	1263	222	2762
NS04-05	32.2	13.02 ± 0.86	0.528 ± 0.011	0.1789 ± 0.0088	2681 ± 62	2732 ± 45	2642 ± 81	- -	0.7%	261	61	286	52	622
NS04-05	35.1	10.08 ± 0.41	0.432 ± 0.017	0.1692 ± 0.0020	2443 ± 37	2316 ± 75	2550 ± 20	- -	9.1%	203	39	2621	440	6493
NS04-05	35.2	11.39 ± 0.48	0.460 ± 0.018	0.1794 ± 0.0024	2555 ± 39	2441 ± 81	2647 ± 22	- -	7.5%	167	11	253	45	583
NS04-05	35a.1	2.82 ± 0.16	0.159 ± 0.006	0.1287 ± 0.0049	1361 ± 42	951 ± 33	2081 ± 67	- -	57%	435	135	17	2	109
NS04-05	35a.2	11.12 ± 0.71	0.459 ± 0.023	0.1756 ± 0.0059	2533 ± 59	2435 ± 103	2612 ± 55	- -	5.2%	90	-15	31	5	69
NS04-05	36a	- -	- -	0.1700 ± 0.0050	- -	- -	2558 ± 49	- -	-	379	91	100	17	274
NS04-05	36.1	10.93 ± 0.54	0.464 ± 0.022	0.1708 ± 0.0022	2517 ± 45	2457 ± 96	2565 ± 21	- -	2.7%	156	32	2828	479	7067
NS04-05	36.2	13.59 ± 0.65	0.550 ± 0.025	0.1793 ± 0.0030	2722 ± 45	2824 ± 102	2646 ± 28	- -	5.5%	147	58	87	16	190
NS04-91	2.1	12.1 ± 1.1	0.492 ± 0.037	0.1781 ± 0.0067	2612 ± 83	2579 ± 159	2636 ± 62	2632 ± 60	conc.	472	112	226	40	462
NS04-91	2.2	11.7 ± 1.1	0.488 ± 0.037	0.1741 ± 0.0066	2582 ± 82	2560 ± 158	2597 ± 62	2595 ± 61	conc.	336	63	155	27	325
NS04-91	3.1	11.8 ± 1.1	0.477 ± 0.036	0.1791 ± 0.0067	2588 ± 82	2514 ± 155	2645 ± 62	2635 ± 58	1.7%	328	70	265	47	558
NS04-91	3.3	10.66 ± 0.96	0.452 ± 0.034	0.1710 ± 0.0065	2494 ± 82	2403 ± 151	2567 ± 63	- -	3.7%	175	48	197	34	410
NS04-91	3.4	8.65 ± 0.78	0.372 ± 0.028	0.1686 ± 0.0063	2302 ± 80	2039 ± 131	2543 ± 62	- -	20%	81	47	748	126	1927
NS04-91	4.1	11.63 ± 1.04	0.476 ± 0.036	0.1773 ± 0.0066	2575 ± 82	2508 ± 155	2628 ± 61	2619 ± 59	1.4%	341	100	246	44	518
NS04-91	4.2	11.23 ± 0.31	0.455 ± 0.009	0.1791 ± 0.0031	2543 ± 25	2417 ± 38	2644 ± 28	- -	9.1%	87	26	131	24	274
NS04-91	9	12.76 ± 0.34	0.513 ± 0.009	0.1803 ± 0.0031	2662 ± 25	2670 ± 38	2656 ± 28	2661 ± 25	conc.	353	104	121	22	243
NS04-91	10	12.22 ± 0.25	0.497 ± 0.005	0.1783 ± 0.0026	2621 ± 19	2600 ± 20	2637 ± 24	- -	0.8%	296	76	439	79	916
NS04-91	12.1	13.99 ± 0.37	0.531 ± 0.010	0.1910 ± 0.0029	2749 ± 25	2746 ± 42	2751 ± 25	2750 ± 24	conc.	97	47	549	105	1049
NS04-91	12.2	14.41 ± 0.59	0.573 ± 0.020	0.1824 ± 0.0036	2777 ± 38	2919 ± 80	2675 ± 32	- -	9.1%	65	10	64	12	113
NS04-91	12.3	11.95 ± 0.33	0.491 ± 0.010	0.1766 ± 0.0029	2600 ± 26	2573 ± 42	2621 ± 28	- -	0.7%	353	90	122	22	253
NS04-91	13	11.72 ± 0.35	0.491 ± 0.011	0.1732 ± 0.0029	2583 ± 28	2574 ± 49	2588 ± 28	2586 ± 26	conc.	271	41	102	18	219
NS04-91	14.1	- -	- -	0.1742 ± 0.0025	- -	- -	2599 ± 24	- -	-	78	37	308	54	642
NS04-91	14.2	16.02 ± 0.49	0.573 ± 0.014	0.2026 ± 0.0032	2878 ± 29	2921 ± 57	2847 ± 26	- -	1.6%	40	91	107	22	187
NS04-91	14.3	12.89 ± 0.33	0.524 ± 0.010	0.1783 ± 0.0024	2672 ± 24	2718 ± 43	2637 ± 23	- -	2.3%	76	15	527	95	1060
NS04-91	15	8.83 ± 0.22	0.397 ± 0.007	0.1612 ± 0.0025	2320 ± 23	2156 ± 32	2468 ± 26	- -	14%	240	68	141	23	383

TABLE 13: Laser ablation U-Pb analyses of zircons from Tanzanian granulite xenoliths (cont.)

Sample	spot	$^{207}Pb/^{235}U$	$^{206}Pb/^{238}U$	$^{207}Pb/^{206}Pb$	Ages (Ma) $^{207}Pb/^{235}U$	Ages (Ma) $^{206}Pb/^{238}U$	Ages (Ma) $^{206}Pb/^{207}Pb$	Conc. age	% disc	cps 202	cps 204	kcps 206	kcps 207	kcps 238
Naibor Soito (cont.)														
NS04-91	19.1	14.83 ± 0.72	0.542 ± 0.019	0.1983 ± 0.0053	2804 ± 46	2793 ± 78	2812 ± 43	2809 ± 42	conc.	309	32	212	42	405
NS04-91	19.2	10.46 ± 0.50	0.422 ± 0.014	0.1797 ± 0.0048	2477 ± 44	2270 ± 64	2650 ± 44	- -	15%	92	36	331	60	777
NS04-91	21.1	14.08 ± 0.66	0.519 ± 0.017	0.1968 ± 0.0053	2755 ± 44	2694 ± 71	2800 ± 44	- -	2.4%	301	78	219	43	440
NS04-91	21.2	13.45 ± 0.62	0.540 ± 0.017	0.1805 ± 0.0048	2712 ± 43	2784 ± 71	2658 ± 43	- -	3.4%	259	58	468	85	938
NS04-91	22	11.65 ± 0.55	0.475 ± 0.016	0.1778 ± 0.0048	2577 ± 44	2505 ± 68	2632 ± 44	- -	3.6%	255	50	492	88	1005
NS04-91	26.1	11.40 ± 0.54	0.465 ± 0.015	0.1779 ± 0.0048	2557 ± 44	2461 ± 68	2633 ± 45	- -	5.6%	243	63	174	31	381
NS04-91	26.2	15.43 ± 0.94	0.567 ± 0.025	0.1971 ± 0.0067	2842 ± 57	2897 ± 101	2802 ± 55	2820 ± 54	1.0%	118	13	79	16	144
NS04-91	26.3	11.12 ± 0.71	0.472 ± 0.022	0.1706 ± 0.0059	2533 ± 59	2494 ± 97	2564 ± 57	2549 ± 54	0.3%	41	41	79	14	152
NS04-91	28	- -	- -	0.1765 ± 0.0073	- -	- -	2621 ± 68	- -	-	42	11	20	4	49
NS04-91	29.1	11.83 ± 0.68	0.482 ± 0.019	0.1781 ± 0.0059	2591 ± 53	2535 ± 81	2635 ± 55	- -	1.8%	258	89	285	51	679
NS04-91	29.2	12.09 ± 0.72	0.493 ± 0.020	0.1778 ± 0.0060	2611 ± 55	2583 ± 87	2632 ± 56	2621 ± 52	conc.	248	56	111	20	225
NS04-91	32.2	15.09 ± 0.86	0.573 ± 0.022	0.1911 ± 0.0063	2821 ± 54	2918 ± 91	2752 ± 53	- -	4.4%	74	32	440	85	801
W3S-2	11	12.33 ± 0.42	0.500 ± 0.012	0.1786 ± 0.0033	2630 ± 32	2615 ± 53	2640 ± 30	2636 ± 29	conc.	351	93	1235	218	2419
W3S-2	13	12.37 ± 0.58	0.506 ± 0.022	0.1774 ± 0.0022	2633 ± 43	2638 ± 95	2629 ± 21	2629 ± 22	conc.	242	66	1547	274	3126
W3S-2	13	10.13 ± 0.54	0.429 ± 0.022	0.1714 ± 0.0026	2447 ± 49	2300 ± 98	2572 ± 25	- -	10%	237	47	540	93	1197

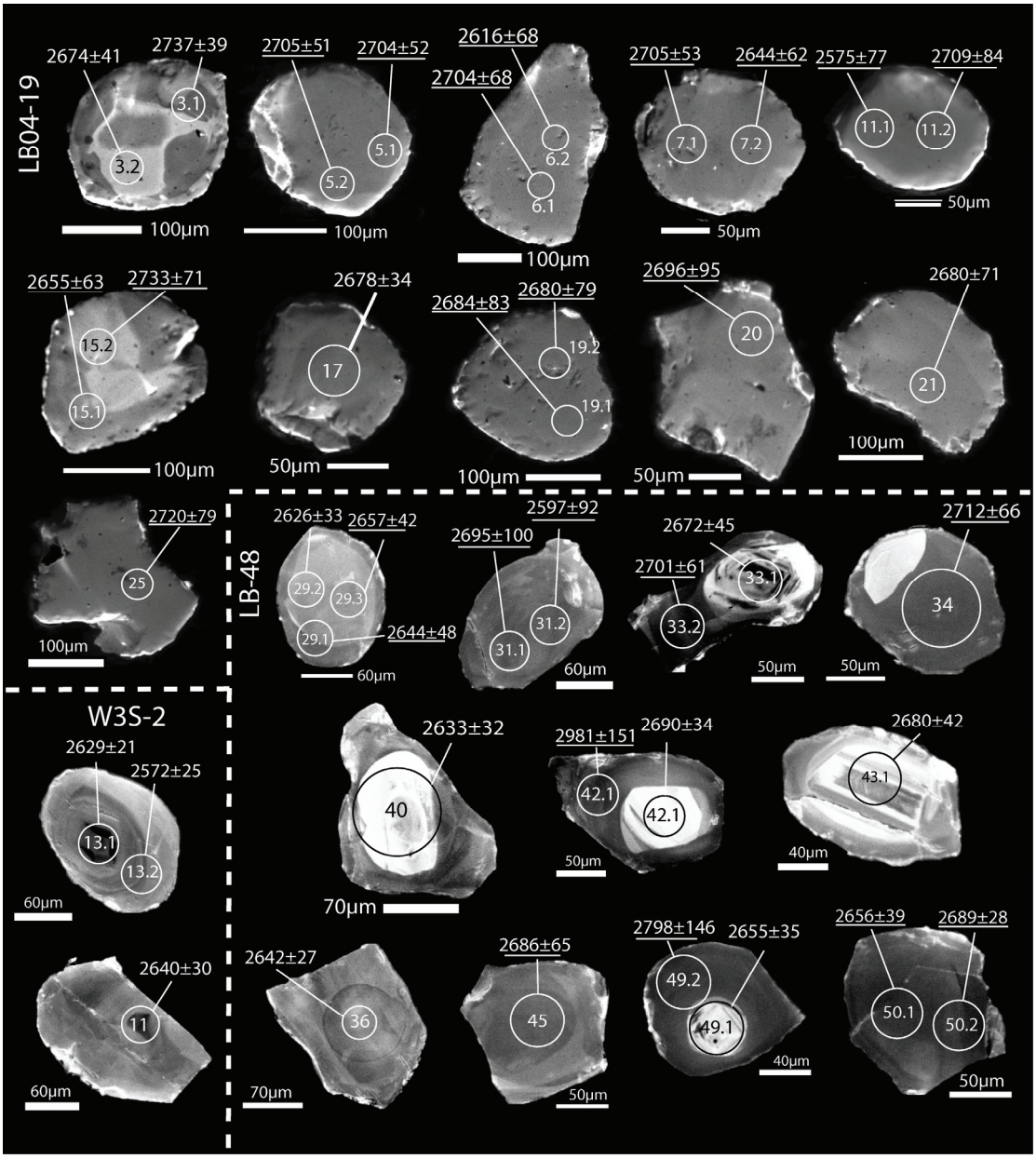

Figure 19. Cathodoluminescence images and $^{207}Pb/^{206}Pb$ ages of zircons from samples LB04-19, LB-48, and W3S-2. Bracketed ages are >2% discordant. Underlined ages indicate analyses for which Pb/U could not be calculated. All ages are in Ma.

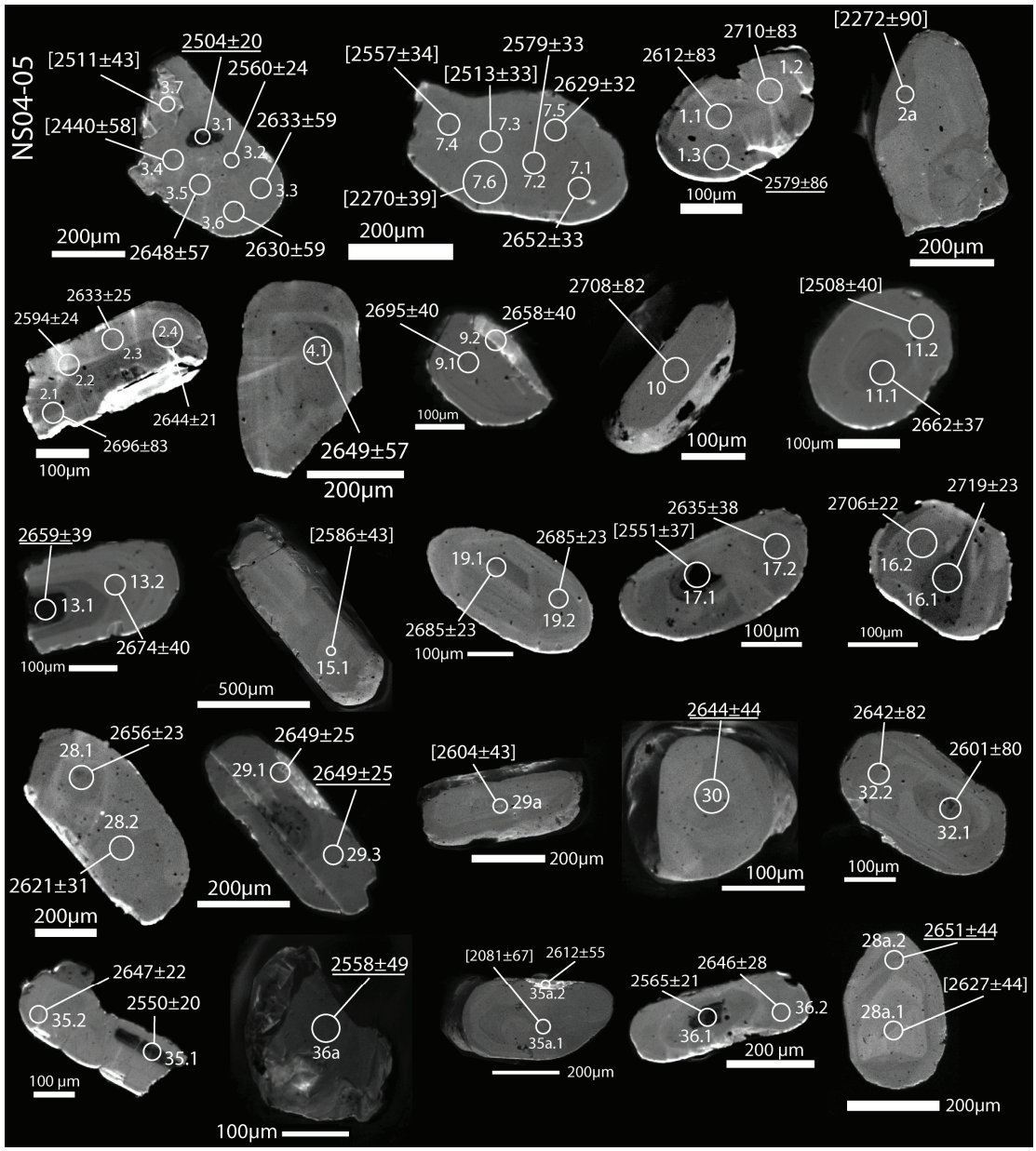

Figure 20. Cathodoluminescence images and $^{207}Pb/^{206}Pb$ ages of zircons from samples NS04-05. Bracketed ages are >2% discordant. Underlined ages indicate analyses for which Pb/U could not be calculated. All ages are in Ma.

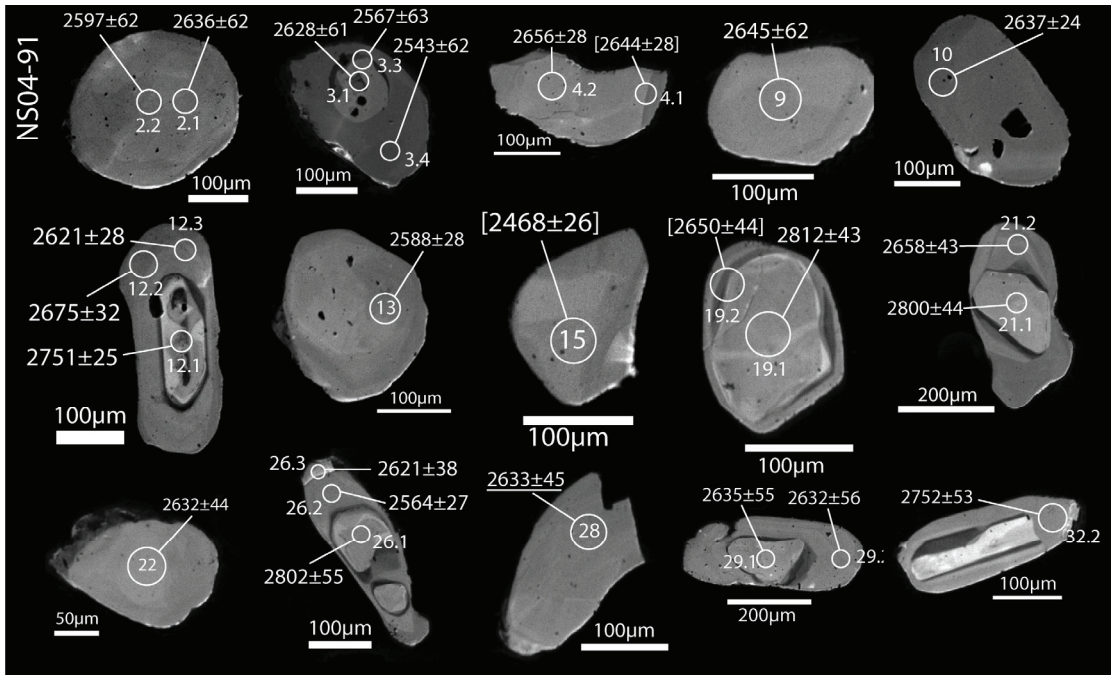

Figure 21. Cathodoluminescence images and $^{207}Pb/^{206}Pb$ ages of zircons from samples NS04-91. Bracketed ages are >2% discordant. Underlined ages indicate analyses for which Pb/U could not be calculated. All ages are in Ma.

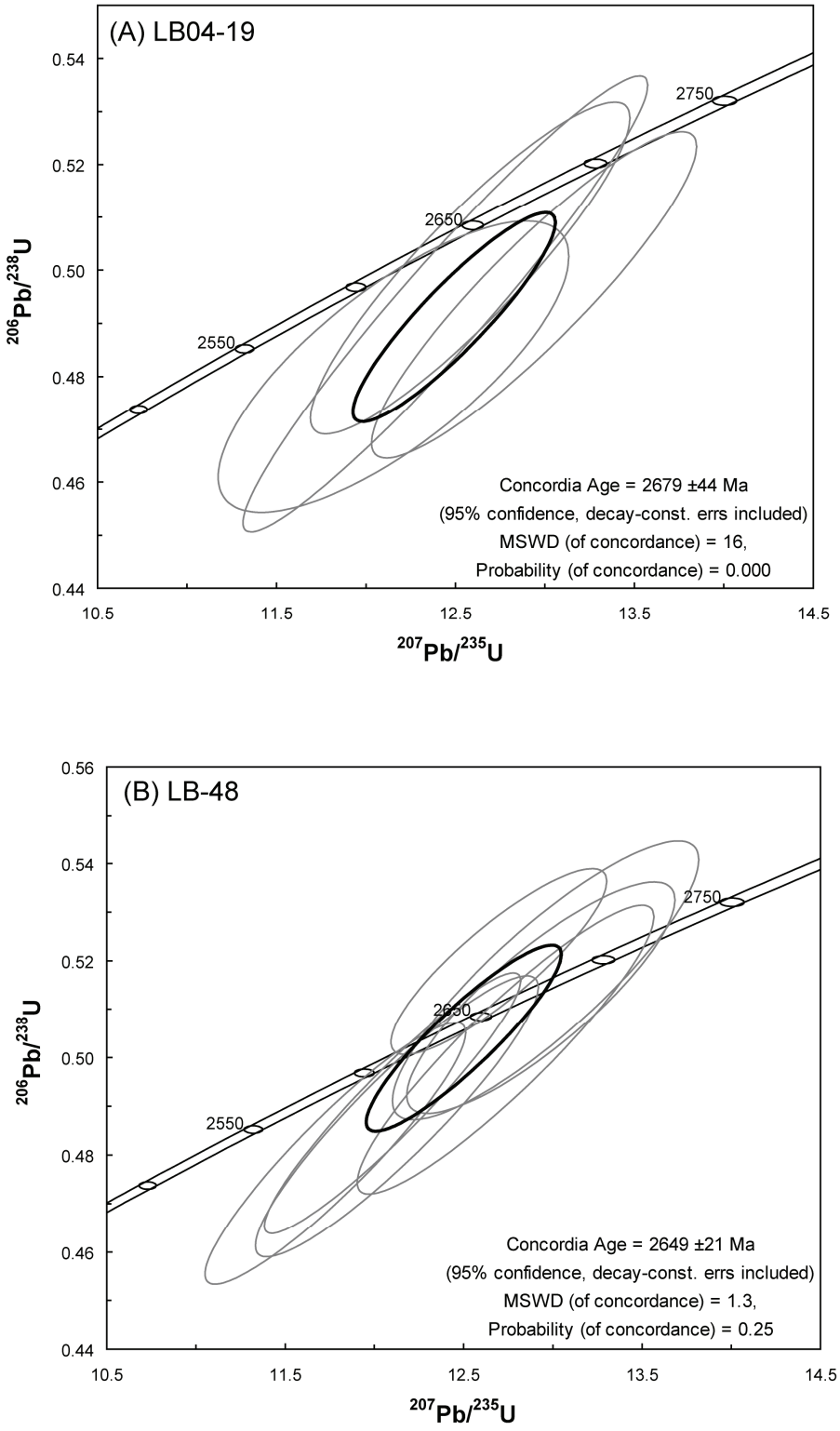

Figure 22. U-Pb concordia diagram for zircons from (a) LB04-19 and (b) LB-48. Calculated using Isoplot/EX v3.00 (Ludwig, 1998).

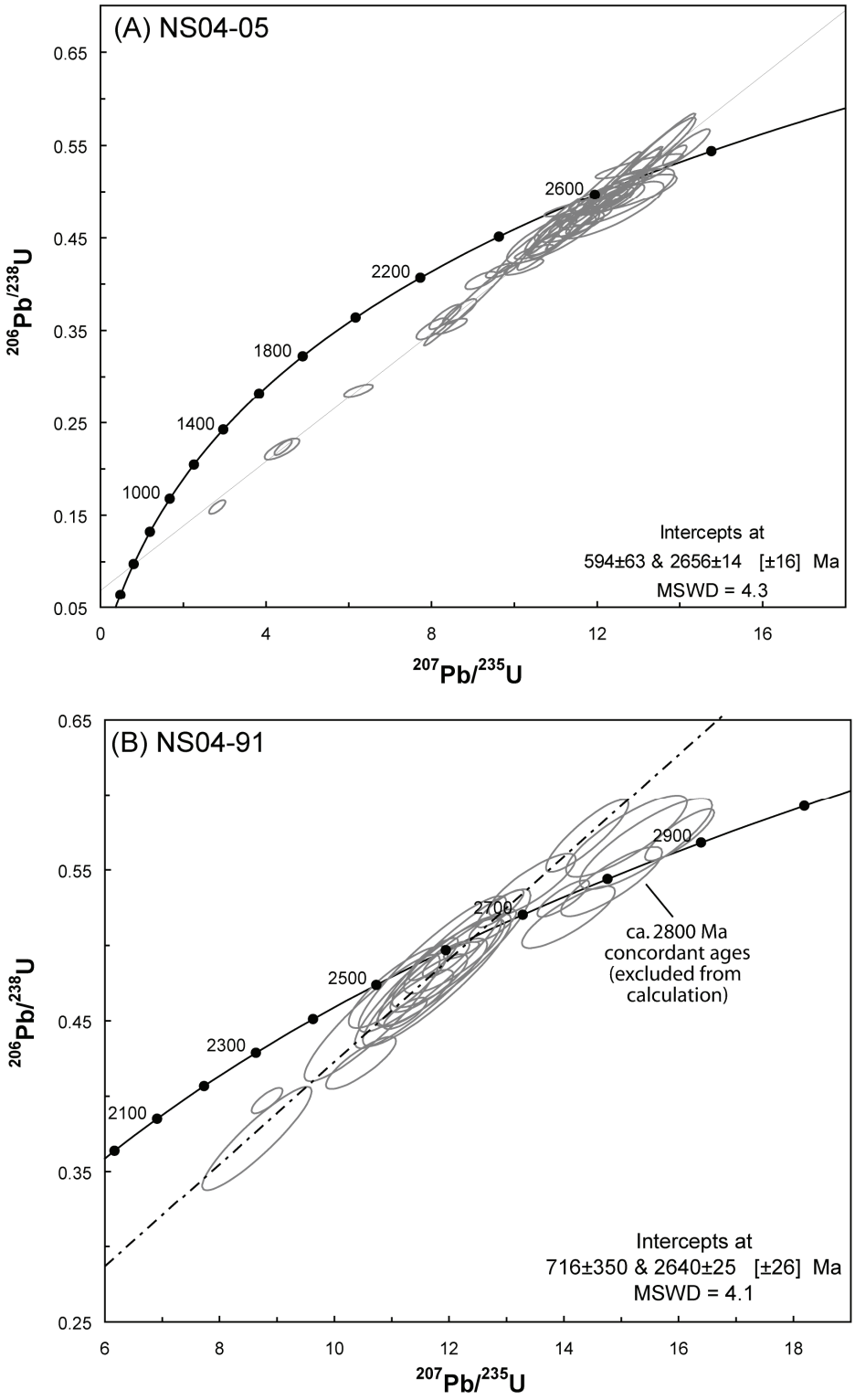

Figure 23. U-Pb concordia diagram for zircons from (a) NS04-05 and (b) NS04-91. Calculated using Isoplot/EX v3.00 (Ludwig, 1998).

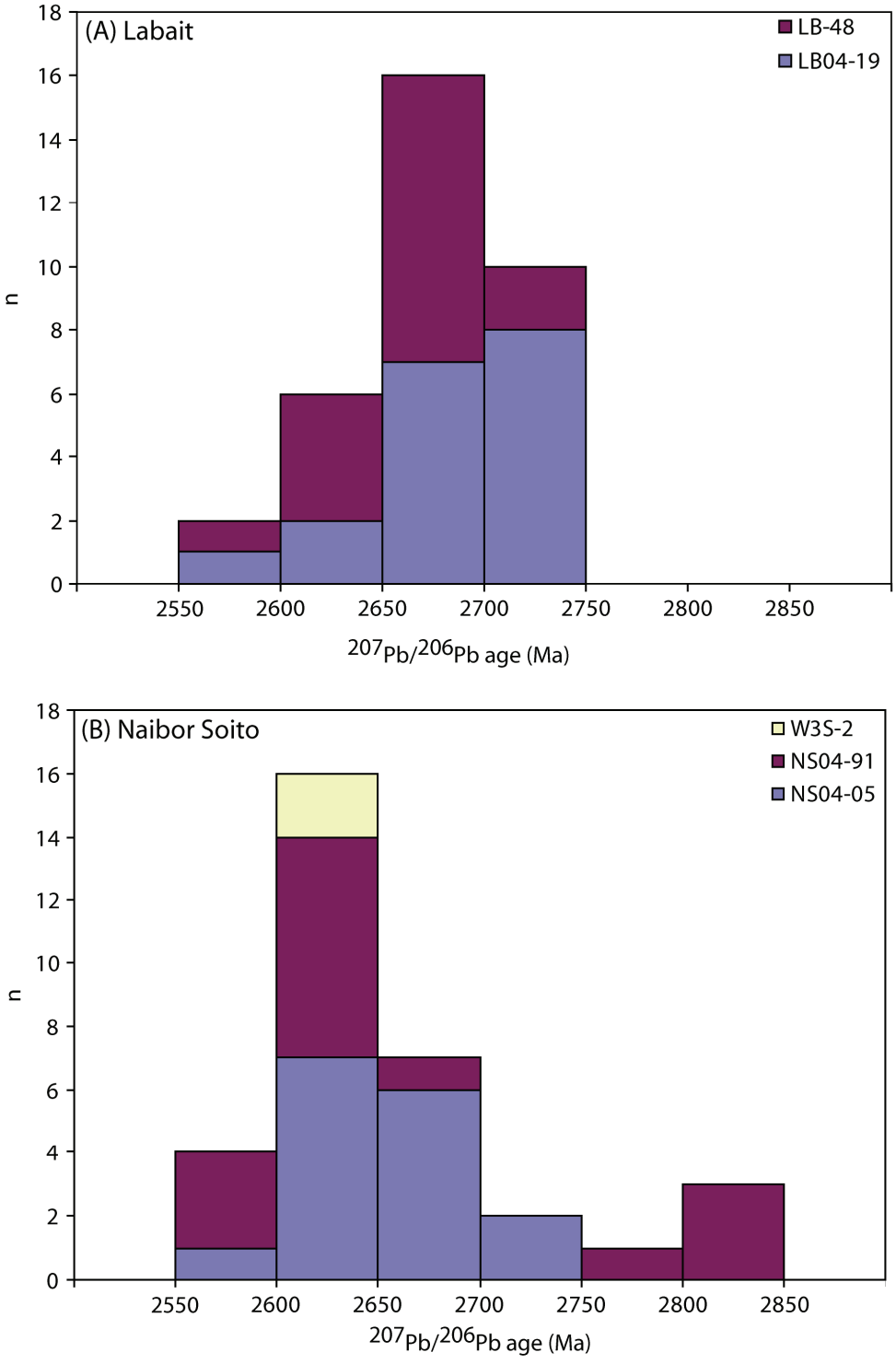

Figure 24. Histogram of $^{207}Pb/^{206}Pb$ zircon ages for granulite xenoliths from (a) Labait and (b) Naibor Soito.

Chapter 5: Discussion

5.1 Influence of alteration and host rock infiltration on whole-rock composition

Secondary addition of incompatible trace elements along grain boundaries in a lower crustal xenolith may obscure primary igneous features (e.g., Condie et al., 2004). It is therefore important to assess how grain boundary alteration in a xenolith suite correlates with sample geochemistry. Alteration in the xenoliths studied here is typically minor but widespread. Most samples exhibit alteration along grain boundaries, particularly between plagioclase or pyroxene crystals, which may represent either fusion or melt intrusion during transport to the surface (cf. Padovani, 1977; Rogers and Hawkesworth, 1982; Leeman et al., 1985) or secondary mineralization formed during post-eruptive weathering. The extent of grain-boundary alteration varies even between lithologically similar granulites, but is generally not reflected in sample chemistry. For example, in the two-pyroxene granulites, where alteration ranges from pervasive (LB04-36, in which grain boundaries are altered and feldspar has a mottled appearance), to moderate (most samples, in which alteration is localized along grain boundaries), to minor (LB04-52 and LB04-53), trace-element patterns are nonetheless similar throughout (Fig. 11a). Low LILE concentrations in most xenoliths seem to preclude significant melt infiltration, as these elements are generally present in much higher concentrations in the East African rift lavas than in the xenoliths considered here (Paslick et al., 1995; Macdonald et al., 2001). A small amount of infiltration, however, cannot be ruled out.

More pervasive alteration is observed in a small number of samples, including LB04-46, which contains mottled plagioclase, abundant oxides (including some that

mantle pyroxene), and extensive grain boundary alteration. High contents of TiO_2 and Ni in this sample, however, are likely a primary feature of the melt that crystallized to form this xenolith and are reflected by the abundant ilmenite in this sample.

5.2 Derivation depths and thermal conditions in the lower crust

Granulite xenoliths from Lashaine and Naibor Soito in the Mozambique belt equilibrated at 720-940°C and 1.3-2.7 GPa (corresponding to depths of 43-90 km). The high pressures are consistent with at least one previous study of the Lashaine xenoliths and suggest equilibration in orogenically thickened crust, most likely during the Neoproterozoic East African orogeny (e.g. Tsujimori et al., 2008). The high pressures calculated for the Lashaine xenoliths appear robust, as both phase equilibria and Na-rich clinopyroxene compositions are broadly consistent with the results given by the Brey and Kohler (1990) barometer. High pressures (>2 GPa) calculated for two of the Naibor Soito xenoliths are somewhat less compelling in the absence of other features typical of high-*P* rocks (e.g., Na-rich clinopyroxene), but are consistent with the high temperatures measured in these samples.

Granulite xenoliths from the craton margin at Labait record lower temperatures. The low temperatures recorded by pyroxene rims in the Labait xenoliths (480 to 670°C for hornblende-free granulites, 640 to 850°C for hornblende-bearing granulites) are unlikely to reflect the highest grade experienced by these samples. Formation of metamorphic pyroxene in a mafic rock at lower crustal pressures typically requires temperatures exceeding ~800ºC, much higher than those preserved by the pyroxene rims, and the presence of antiperthite likewise argues for higher temperatures (e.g., Green and

Usdansky, 1986; Fuhrman and Lindsley, 1988; Stipska and Powell, 2005). Temperatures calculated using pyroxene core compositions may therefore better reflect the peak temperature experienced by these xenoliths, a possibility supported by discoloration along clinopyroxene rims in the Labait two-pyroxene granulites, which may represent low-temperature alteration (Fig. 2c-d). Core temperatures (610-800°C) overlap with, but are generally somewhat lower than, temperatures found in the Lashaine and Naibor Soito xenoliths. The low rim temperatures are interpreted to reflect partial re-equilibration to modern thermal conditions in the cratonic lower crust (400-500°C at 40 km, modeled after the cratonic geothermal gradient in Rudnick et al., 1998).

The absence of coexisting clinopyroxene, orthopyroxene, and garnet from the Labait suite makes it difficult to estimate the pressure at which those xenoliths equilibrated. However, if the temperatures of 610-800ºC recorded by pyroxene core compositions are taken as the temperature at which the garnet-orthopyroxene barometer closed, a pressure can be estimated for the garnet-orthopyroxene xenolith LB04-39. (Though present, clinopyroxene from this sample is rare and is not in textural equilibrium with orthopyroxene.) For temperatures of 610-800ºC, this sample yields a pressure of 0.3-1.0 GPa, corresponding to a depth of 10-33 km (Julià et al., 2005). Equilibration at a relatively shallow depth is consistent with the absence of garnet from most Labait xenoliths, and these samples betray no indication of equilibration at the base of thickened crust.

In summary, both granulite xenolith suites from the Mozambique belt appear to record high pressure and temperatures. Pressure estimates in the Lashaine xenoliths suggest that they may have been metamorphosed near the base of doubly thickened crust

during the East African orogeny (e.g., Tsujimori et al., 2008). Evidence that the Naibor Soito xenoliths equilibrated at similar pressures is less striking, but high temperatures in these xenoliths appear to necessitate equilibration near the base of the crust. The Lashaine and Naibor Soito suites may thus represent the lower crust of the lower plate during continent-continent collision (e.g., Ellis, 1996). By contrast, the Labait xenoliths from the craton margin appear to have formed at conditions typical of unthickened, middle to lower continental crust. This finding is consistent with the lack of post-Archean deformation in the Tanzanian craton. To accommodate pressure estimates from both Labait and Lashaine, crustal thickness during the East African orogeny would have had to increase significantly, from ~40 to ~80 km, within ~150 km of the craton margin. While dramatic, an increase on this order is consistent with that observed in the modern Himalayas (e.g., Jiménez-Munt et al., 2008).

5.3 Age of the Tanzanian lower crust

5.3.1 Zircons

The oldest zircons analyzed in this study were rare 2750-2800 Ma cores from NS04-91. These are typically prismatic in habit and bright in CL, suggesting an igneous origin and the existence of crustal fragments in Tanzania by 2800 Ma. Most zircons record younger Archean ages, with pooled concordant ages for zircons from two Labait xenoliths and concordia upper-intercept ages from two Naibor Soito samples falling between 2640 and 2680 Ma. The ca. 2660 Ma zircons encompass morphologies and zoning patterns consistent with both igneous and metamorphic origins, suggesting that intrusion and metamorphism were broadly synchronous. Zircon ages are comparable to

zircon and Sm-Nd isochron ages measured in greenstone belts in the Tanzanian craton, including the ca. 2660 Ma Musoma-Mara belt (Manya et al., 2006) and the ca. 2820 Ma Sukumuland belt (Manya and Maboko, 2003), and more generally through the Tanzania upper crust (Collins et al., 2004; Johnson et al., 2003; Möller et al., 1998; Muhungo et al., 2001; Sommer et al., 2003). Zircons suitable for analysis using laser-ablation ICP-MS are absent from the Lashaine xenoliths, and it is unclear whether these xenoliths crystallized at the same time as those from the other suites.

No zircons formed during either the Usagaran or East African orogenies were found. However, U-Pb concordia for samples NS04-05 and NS04-91 give ca. 600 Ma lower-intercept ages, consistent with Pb loss during East African metamorphism. Pb loss in the Naibor Soito xenoliths is perplexing. Mezger and Krogstad (1997) argue that Pb loss in zircon in the continental crust occurs only at temperatures below 650°C. At higher temperatures, the zircon lattice anneals efficiently and little Pb can be lost. Neoproterozoic Pb loss in zircons from the Naibor Soito xenoliths may imply that these xenoliths were located in the middle to upper crust during part of the East African orogeny, prior to their emplacement in the lower crust.

5.3.2 Rb-Sr

Little age information can be gleaned from the Rb-Sr whole-rock data reported here, save that the relatively unradiogenic $^{87}Sr/^{86}Sr$ (<0.705) measured in most xenoliths requires that low Rb/Sr ratios have characterized most Tanzanian xenoliths since their formation. Rb/Sr and time-integrated $^{87}Sr/^{86}Sr$ ratios are low relative to igneous rocks in the Tanzanian upper crust (which have $^{87}Sr/^{86}Sr$ up to 0.73178; Maboko, 2000; Möller et

al., 1998; and Maboko and Nakamura, 2003). Low Rb/Sr ratios in xenoliths from Labait and Naibor Soito interpreted to have originated as crystallized melts are unlikely to be primary igneous features, instead implying depletion through metamorphism or partial melting. The timing of Rb-depletion can only be estimated very roughly, as it depends strongly on the initial Rb concentration. If the highest Rb/Sr ratios (0.12-0.20) measured in this study were typical of the melts at the time of crystallization, a 0.3-0.5% difference in $^{87}Sr/^{86}Sr$, comparable to the total range seen in most of the Tanzanian xenoliths at present, would be produced in ca. 500 Ma. Early Rb-depletion may also imply that the other LILE, which are typically present in anomalously low concentrations in the Tanzanian xenoliths, were removed from the lower crust relatively soon after crystallization.

In contrast to the other Tanzanian xenoliths, the biotite granulites have elevated $^{87}Rb/^{86}Sr$ ratios and relatively radiogenic $^{87}Sr/^{86}Sr$ ratios. Whole-rock Nd T_{DM} ages for the biotite granulites are ca. 2.9 Ga, implying that their protoliths formed during the Archean, but their $^{87}Sr/^{86}Sr$ ratios diverged from those of the garnet-clinopyroxene granulites at ca. 1.8 Ga, based on the errorchron presented in Fig. 18. A Sr errorchron age for a similar granulite xenolith from the Kola Peninsula was interpreted to constrain the minimum age of Rb metasomatism (Kempton et al., 2001). However, the smooth trace-element patterns and Archean T_{DM} ages in the biotite granulites would seem to preclude such an interpretation here, as any metasomatic event would have to completely overprint the existing trace-element pattern while leaving the T_{DM} age undisturbed. The errorchron age may instead reflect metamorphism during the Usagaran orogeny, an event that is otherwise not recorded in the xenoliths considered here.

5.3.3 Sm-Nd

Linear trends on a Nd isochron plot like those seen for the Tanzanian xenolith suites can be produced by either radioactive decay of ^{147}Sm (in which case the slope of the trend corresponds to the age of the sample suite) or mixing. The latter possibility is discounted here because of (1) the absence of magma in the Kenyan and Tanzanian rifts with high enough Sm/Nd to account for the trends in Fig. 17a (Cohen et al., 1984; Paslick et al, 1995; Rogers et al., 2000; Macdonald et al., 2001; Aulbach et al., 2008) and (2) the apparent lack of other episodes of post-Archean volcanism in the study area. The linear trends for the Labait and Naibor Soito xenoliths are therefore likely to have resulted from decay of ^{147}Sm.

Sm-Nd data for the Labait and Naibor Soito xenolith suites scatter around a ca. 2660 Ma reference line (corresponding to zircon ages from samples from both localities) on the Nd isochron plot in Fig. 17a. More precise isochrons cannot be calculated because of scatter within the isotopic data. Such scatter is a common feature in granulite xenolith suites and can be attributed to either post-emplacement open-system behavior or heterogeneity in the magma source region. Nd isotope ratios for individual xenoliths were back-calculated to the zircon crystallization age (ca. 2660 Ma) to assess the isotopic characteristics of the lower crust beneath Labait and Naibor Soito at the time of its crystallization.

At Labait, values of ε_{Nd}(2660 Ma) in the metagabbroic xenoliths range from -0.3 to -2.7, consistent with the distribution of the Labait xenoliths below the 2660 Ma reference line in Fig. 17a. At least some of this range may have resulted from open-

system behavior. For example, LB04-39 and LB04-91, while similar geochemically, give very different ε_{Nd}(2660 Ma) values (-2.7 and -0.3, respectively). The similarity of trace-element compositions in these xenoliths is inconsistent with derivation from different mantle sources, suggesting that the low value from LB04-39 resulted from open-system behavior. Nevertheless, all Labait samples yield values of ε_{Nd}(2660 Ma) distinctly lower than the depleted mantle at this time (+2.3, following DePaolo, 1981). The negative ε_{Nd}(2660 Ma) values observed in the xenolith suite are consistent with either assimilation of continental material or derivation from undepleted mantle. The former possibility is difficult to square with high Ni concentrations in the Labait samples, which would seem to argue against significant crustal assimilation.

At Naibor Soito, values of ε_{Nd}(2660 Ma) from the quartz and quartz-free xenoliths range from -0.9 to +7.0. Quartz xenolith NS04-13 gives the highest value (+7.0), but the Nd concentration in this sample is low (2.37 ppm), rendering it vulnerable to overprinting and suggesting that its high ε_{Nd}(2660 Ma) value resulted from open-system behavior. This sample is excluded from the discussion of potential magma source regions. Excepting NS04-13, the Naibor Soito samples range from -0.9 to +3.1, with all but NS04-80 falling below +2.3. Most xenoliths from this locality therefore have ε_{Nd}(2660 Ma) similar to, but slightly lower than, the depleted mantle at 2660 Ma, consistent with a mantle melt that assimilated a small amount of continental crust. Unlike the Labait xenoliths, Ni concentrations at Naibor Soito are variable and do not preclude this interpretation.

In contrast to the Labait and Naibor Soito suites, an episode of recent overprinting is evident in the Sm-Nd data from the garnet-clinopyroxene granulites from Lashaine

reported here and by Cohen et al. (1984). In these samples, correlation between $^{143}Nd/^{144}Nd$ and $^{147}Sm/^{144}Nd$ is poor, implying widespread open-system behavior (Table 12, Fig. 17a).

Overprinting of the original isotopic signature may have resulted from infiltration of comparatively Nd-rich host magma into the Lashaine xenoliths. This possibility was tested using a simple mixing model. Cohen et al. (1984) reported that the Lashaine ankaramite contains 52 ppm Nd with a $^{143}Nd/^{144}Nd$ ratio of 0.51276 and a $^{147}Sm/^{144}Nd$ ratio of 0.100. Using this composition as the magma end-member in the calculation, the Sm-Nd systematics of the garnet-clinopyroxene xenoliths can be modeled as resulting from <10% melt infiltration (Fig. 25). If the Lashaine samples initially fell on an isochron (that is, they did not all have the same isotopic composition, as the model presented in Fig. 25 implies), the amount of infiltration required is much lower. This possibility is modeled in Fig. 26, with the pre-mixing baseline defined by a three-point isochron calculated for samples with ca. 2.9 Ga T_{DM} ages (89-726, 89-733, 89-745). This calculation implies that 2-5% melt infiltration is sufficient to account for the spread in Sm-Nd data observed in the Lashaine xenoliths, with the necessary amount of melt infiltration depending primarily on the initial concentration of Nd in the crust. Further, it shows that the range of $^{143}Nd/^{144}Nd$ ratios likely extended to lower, more unradiogenic values prior to mixing. Such a small amount of mixing would not be expected to have a dramatic effect on the trace-element compositions of the xenoliths, particularly if concentrations were even modestly heterogeneous to begin with. For example, the addition of 5% melt containing 1 ppm Cs into Cs-poor crust would increase the whole-rock concentration by ~0.05 ppm. If the range in Cs concentrations in the xenoliths prior

to overprinting is similar or greater than this value, as appears likely (Table 11), melt infiltration would be difficult to detect in the trace-element data.

Overprinting of the isotopic compositions of the Lashaine granulites makes it difficult to assess the nature of the magma source region, as only a small number of xenoliths (notably, the Nd-rich biotite granulites) preserve apparently undisturbed Nd isotope ratios. The problem is compounded by the lack of zircon ages from this locality, as we cannot be certain that these samples formed at the same time as xenoliths from Labait and Naibor Soito. Indeed, the trace-element compositions of the biotite granulites suggest they formed in a different tectonic setting than the melt-like xenoliths from Labait and Naibor Soito. (This possibility is discussed further below). Nevertheless, the unradiogenic $^{143}Nd/^{144}Nd$ ratios and old T_{DM} ages that are typical of the Lashaine xenoliths are consistent with formation of the lower crust during the Archean. The ca. 2.9 Ga T_{DM} ages in the undisturbed samples were likely typical of the entire suite prior to overprinting. Whether these T_{DM} ages define the true age of these samples is, however, ambiguous, as the melt-like biotite granulites have highly enriched trace-element patterns uncharacteristic of magmas derived from partial melting of the depleted mantle. Values of ε_{Nd} for biotite granulite 89-733 at 2800 Ma and 2660 Ma are +1.7 and +0.7, respectively, similar to but slightly lower than the depleted mantle of DePaolo (1981) at these times.

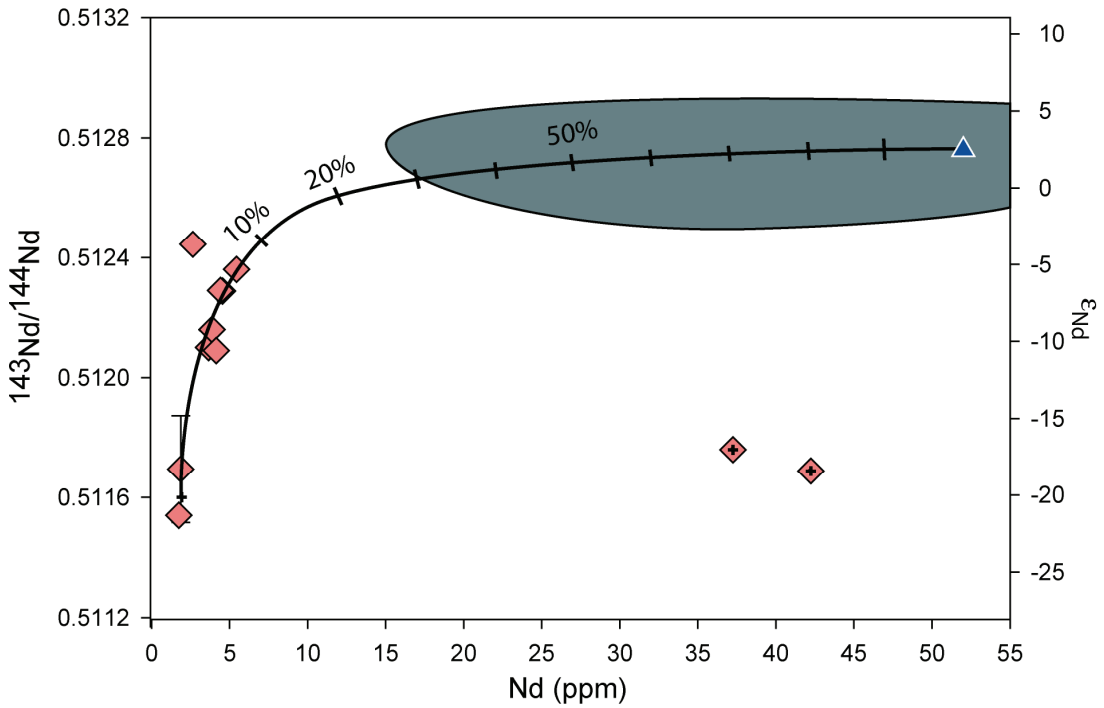

Figure 25. Results of a model describing mixing between the Lashaine xenoliths and host magma (blue triangle). Blue field represents the Nd composition of the Kenyan rift basalts (Macdonald et al., 2001). End-member model compositions: Crustal $^{143}Nd/^{144}Nd = 0.51150$; crustal Nd concentration = 2 ppm; magma $^{143}Nd/^{144}Nd = 0.51276$; and magma Nd concentration = 52 ppm.

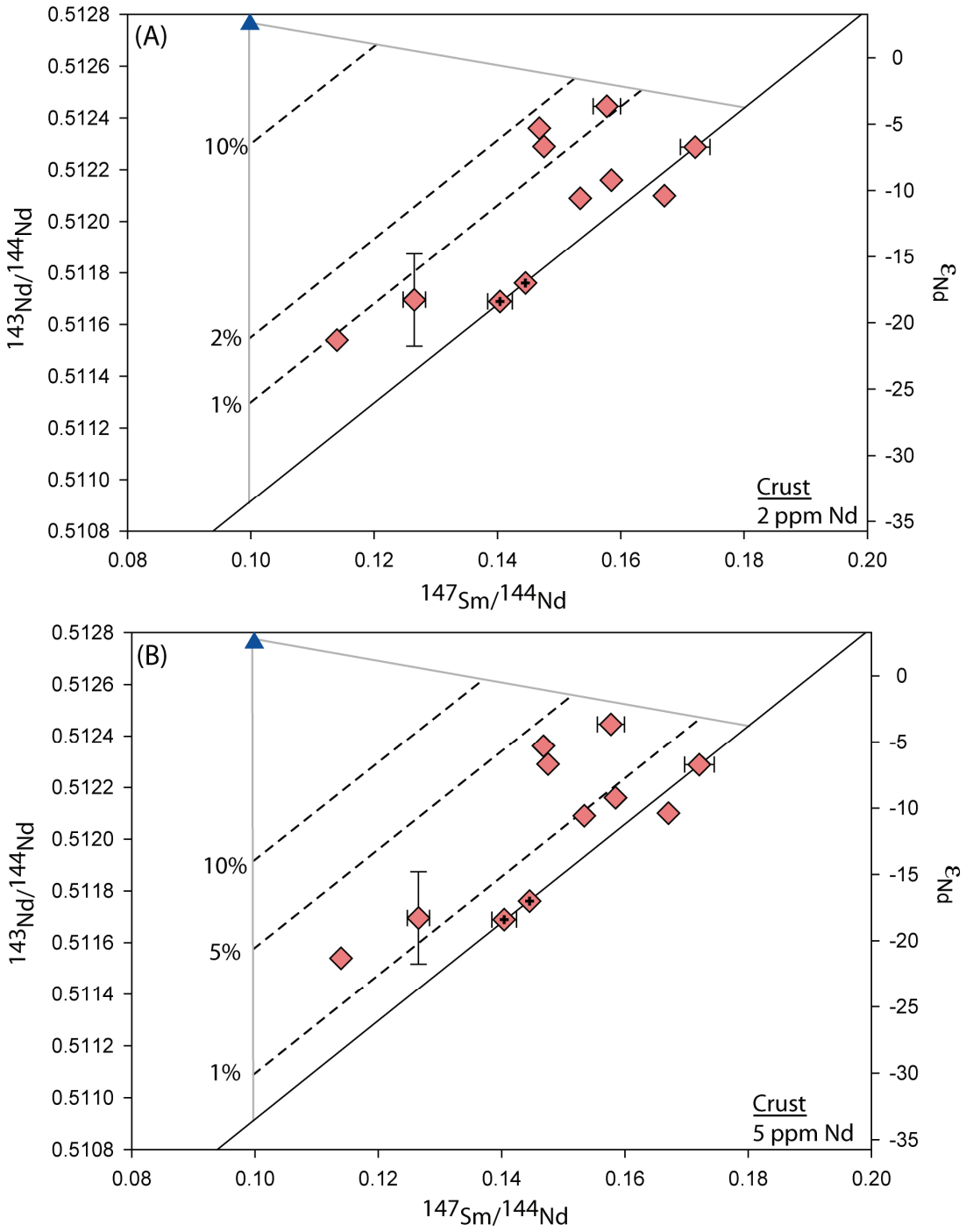

Figure 26. Results of the model presented in Fig. 25 plotted on a Nd isochron diagram for crustal Nd concentrations of (a) 2 ppm and (b) 5 ppm. Other model parameters and symbols are identical to those in Fig. 25. Includes data from Cohen et al. (1984).

5.4 Formation of the Tanzanian lower crust

All granulites xenoliths considered here formed from igneous protoliths, either crystallized melts or cumulates, which recrystallized at high pressure and temperature to form the observed mineral assemblages within a few tens of Ma of intrusion.

5.4.1 Labait

The LREE-enriched trace-element patterns, high Ni contents, and moderate SiO_2/Al_2O_3 ratios in the two-pyroxene granulites suggest that their protoliths were crystallized Archean basaltic melts (Table 11). Unlike the biotite granulites from Lashaine or the quartz-free granulites from Naibor Soito, the Labait xenoliths range to relatively evolved compositions (up to 54 wt% SiO_2) and high La/Nb ratios (1.3-7.1). Negative Nb and Ti anomalies (Fig. 11a) are likely primary features of the magma, suggesting formation in a convergent margin setting. High Ni concentrations suggest that assimilation of pre-existing crust was minor, though negative ε_{Nd} values suggest otherwise. By contrast, low LILE concentrations in the two-pyroxene xenoliths may reflect metamorphic depletion (e.g., Rudnick et al., 1985; Rudnick and Taylor, 1987). Ubiquitously unradiogenic $^{87}Sr/^{86}Sr$ in the Labait samples implies that this depletion occurred early in the xenoliths' history.

Major- and trace-element compositions for the garnet-orthopyroxene and hornblende-bearing xenoliths share several key features with the two-pyroxene granulites, including moderate La/Nb ratios, basalt-like SiO_2/Al_2O_3 ratios, Ti depletions, and low LILE concentrations (Table 11). Positive Sr and Eu anomalies in the garnet-orthopyroxene granulites suggest some degree of plagioclase accumulation in these

samples, while high Al_2O_3 contents, low Th/U, and flat HREE patterns imply either metamorphic concentration of garnet or preferential sampling of garnet porphyroblasts in the sample powder (e.g., Rudnick and Taylor, 1987). Variable trace-element patterns in the hornblende-bearing xenoliths are more difficult to pigeonhole beyond the first-order similarities noted above. The LREE-enriched pattern in LB04-82 is broadly similar to those in the two-pyroxene granulites, while the flat REE pattern and high Th/U ratio for LB04-07 may reflect preferential sampling of hornblende. The anorthosite LB04-27 shares few similarities with the other Labait xenoliths. It likely formed not as a melt but as an anorthite cumulate, as indicated by the abundant calcic plagioclase, extremely high CaO and Al_2O_3, and positive Eu and Sr anomalies in this sample (Figs. 11c and 12c).

Most features of the Labait granulite xenoliths, notably the variable, generally high La/Nb ratios, are consistent with formation in a convergent margin (Condie, 1999). The LREE-enriched trace-element patterns are particularly similar to average compositions for basalts formed in continental arcs like the Andes or evolved island arcs like Japan. High Ni concentrations similar to those seen in the Labait samples (107-410 ppm) are unusual for evolved arc basalts, wherein Ni contents and Mg number decrease rapidly as a result of fractional crystallization. However, Archean basalts have generally higher Ni contents at a given Mg number than younger basalts, consistent with higher temperatures in the Archean mantle (Arndt, 1991; Condie, 1994).

One curious aspect of the geochemistry of the Labait samples are high Ba concentrations (>5000 ppm in the two-pyroxene granulites). Such high Ba concentrations are rare in basaltic rocks, with the principle exception being alkali-rich basalts like lamproites or orangeites representing low-degree partial melting of the mantle. Few

granulite xenoliths have comparable concentrations. Furthermore, even considering the alkali feldspar common in the Labait samples, it is difficult to account for the high Ba abundances based on the modal proportion and chemistry of major minerals in the two-pyroxene granulites. A simple mass-balance calculation bears this out. In a sample containing 60% antiperthite, 10% of which is alkali feldspar containing 1.5 wt% BaO, only ~800 ppm Ba is hosted in feldspar. This is dramatically lower than the measured whole-rock concentrations, suggesting that most of the Ba is hosted along grain boundaries. However, the Labait melilite is Ba-poor (<200 ppm Ba; Dawson, 1999) relative to the xenoliths, and it is unlikely that contamination by the host magma is responsible for the high Ba concentrations in the xenoliths.

One possibility is that the xenoliths inherited their high Ba contents from the mantle underlying Labait. Spinel lherzolites recovered from Labait also show elevated Ba concentrations (200-700 ppm), which have been attributed to multiple episodes of metasomatism in the Tanzanian mantle, including one related to an ancient volcanic arc (Dawson, 1998; 2002). The high Ba concentrations in the lower crust beneath Labait may reflect metasomatism by fluids similar to those that introduced Ba into the lithospheric mantle. If this is the case, it is unclear why concentrations of Ba in the crust are much higher relative to those in the mantle. Alternatively, if the high Ba concentrations in the Labait mantle predate the formation of the lower crust sampled in granulite xenoliths from this locality, melts containing 4000-6000 ppm Ba can be produced by 5-10% equilibrium melting of peridotite containing ~500 ppm Ba and ~1% biotite.

5.4.2 Lashaine

The protoliths of the garnet-clinopyroxene granulites likely originated as plagioclase-rich cumulates in the lower crust, as suggested by Jones et al. (1983). Features of the sample chemistry consistent with a cumulate origin include high Na_2O and Al_2O_3 contents that are similar to those in Proterozoic massif anorthosites and leucogabbros (Ashwal, 1993) and that correlate with the relative proportions of plagioclase and clinopyroxene in each sample; low SiO_2/Al_2O_3 ratios, which Kempton and Harmon (1992) argue can result from plagioclase accumulation (Fig. 9a); and ubiquitous positive anomalies for Sr and Eu, both of which are compatible in plagioclase under reducing conditions (Fig. 13a-b, 14a-b). The small amount of melt infiltration argued for above should have only a minor effect on these aspects of the sample chemistry. A cumulate (as opposed to a restitic) origin is likely because of (a) the narrow range in whole-rock concentrations of SiO_2 and most incompatible trace elements and (b) variable whole-rock concentrations of compatible elements (e.g., Sr and Eu in plagioclase, Ni in clinopyroxene), which correspond to the proportion of these phases in each sample. Similar arguments were made by Rogers and Hawkesworth (1982) for the crustal xenoliths from Lesotho in the Kaapvaal craton and by Dessai et al. (2004) for xenoliths from the Dharwar craton. Certain features of the Lashaine xenoliths, including low concentrations of most incompatible elements and relative depletion in Cs, Rb, Th, U, and Nb, are primary features of plagioclase cumulates and, unlike the Labait xenoliths, cannot be attributed to metamorphic processes.

Pyroxene-rich sample 89-734 has low SiO_2 and Al_2O_3, high Fe_2O_3, Ni and MgO, a moderate SiO_2/Al_2O_3 ratio, relatively low Mg number, and a flat, relatively smooth

trace-element pattern broadly similar to that of the quartz-free granulites from Naibor Soito. This may imply that this xenolith, in contrast to the other garnet-clinopyroxene granulites, originated as a basaltic melt with only a minor contribution from cumulate plagioclase or clinopyroxene.

The biotite granulites have melt-like SiO_2/Al_2O_3 ratios, high concentrations of most incompatible trace elements, and smooth trace-element patterns, suggesting that their protoliths were crystallized melts (albeit ones of somewhat unusual composition). Their negative Sr and Eu anomalies are complementary to the positive anomalies in the garnet-clinopyroxene granulites (Figs. 13c and 14c), suggesting that the protoliths of the garnet-clinopyroxene xenoliths formed via fractionation of plagioclase and pyroxene from magmas similar to the biotite granulites. This possibility is supported by modeling of equilibrium crystallization, which shows that a mixture of plagioclase and clinopyroxene crystallized from magma with a trace element composition similar to the biotite granulites can reproduce the REE patterns of the garnet-clinopyroxene granulites with ~5% equilibrium crystallization. Low Ni concentrations and Mg numbers in the biotite granulites are consistent with removal of a mafic phase like pyroxene.

The biotite granulites have enriched trace-element patterns, relatively low La/Nb (1.3-1.5), and high Ti/V ratios (~75), all of which are similar to mafic melts formed during episodes of intraplate volcanism linked to mantle "plumes" (Figs. 9b and 13c; Condie, 1999; Shervais, 1982). This possibility is supported by Paslick et al. (1995), who argued that high time-integrated U/Pb ratios in the Tanzanian subcontinental lithospheric mantle resulted from underplating of OIB-like magmas at >2 Ga ago. The biotite granulites are therefore distinct from the melt-like granulite xenoliths of arc affinity from

Labait and Naibor Soito, and the apparent difference in the tectonic setting may require multiple episodes of Archean crust formation in the Tanzanian lower crust. One possibility is that the biotite granulites are part of an older crustal fragment like that implied by the ca. 2800 Ma zircons from NS04-91. This idea can be tested by dating zircons from the biotite granulites.

5.4.3 Naibor Soito

Major and trace element concentrations in both the quartz and quartz-free granulites are commonly well-correlated (e.g., Figs. 8 and 10), suggesting the two types are related. Two quartz-free xenoliths (NS04-61 and NS04-80) have major element compositions similar to tholeiitic basalt, with relatively low Mg numbers and Ni concentrations suggesting that their protoliths were relatively evolved basaltic melts. Trace-element patterns (Fig. 15b) are qualitatively similar to basalts from modern island arcs, with La/Nb (1.3-1.5) ratios overlapping the boundary between MORB/OIB and arc basalts (Condie, 1999).

The more common quartz granulites betray a more complex history, but at least three aspects of their geochemistry suggest that their protoliths were also crystallized melts. First, excepting the two most highly evolved samples, their SiO_2/Al_2O_3 ratios fall within the range observed in basalts and andesites (Fig. 9a). Second, correlation between most major elements, the transition metals, and the HREE among both the quartz and quartz-free granulites is commonly very good. Of particular significance is the Ni-MgO correlation, which suggests that this suite is related by olivine fractionation (Fig. 10a). Third, trace-element patterns, while variable, show almost ubiquitous Nb and Ti

depletions similar to those in the Labait xenoliths, suggesting that the protoliths of the quartz granulites also originated in an arc (Fig. 15a). Samples with high trace-element abundances (NS04-01, NS04-05, NS04-98) are particularly similar to the two-pyroxene granulites from Labait. The quartz and quartz-free xenoliths likely originated in the same arc, with the evolved, Nb- and Ti-depleted compositions in the quartz xenoliths reflecting a larger contribution from slab fluids. Moreover, the predominance of ca. 2660 Ma zircons in both the Labait and Naibor Soito granulites suggests that the lower crust sampled from both the craton and the Mozambique belt formed in the same convergent margin. Similarly aged, arc-like volcanic rocks in the Musoma-Mara greenstone belt in the Tanzanian craton may have formed in the same setting (Manya et al., 2006, 2007).

This interpretation in itself does not suffice to explain the unusually wide range in major and trace element concentrations present within the Naibor Soito xenoliths. A possible analogue in this regard is a suite of granulite xenoliths from the Baltic Shield described by Kempton et al. (1995, 2001). These authors classified the felsic portions of two composite xenoliths as migmatites, arguing that silica-rich, felsic leucosomes were produced via partial melting of mafic granulite in the lower crust. A similar interpretation for the Naibor Soito xenoliths is supported by the presence of abundant hydrous phases within the mafic domains in many xenoliths, which would depress the melting temperature of granulite and facilitate partial melting. Like the feldspar-rich domains in the quartz granulites (NS04-13 and NS04-83), the Kola leucosomes have low MgO and Ni contents relative to coexisting mafic bands. However, unlike the Kola xenoliths, NS04-13 and NS04-83 have fractionated Sr/Y (~180), $(La/Yb)_n$ (~25), and Zr/Sm (~90) ratios, broadly similar to trondjhemite-tonalite-granodiorite (TTG) gneisses that are

common in Archean terranes and are thought to form via partial melting of garnet-bearing metabasalts (e.g., Rapp et al., 2003; Moyen and Stevens, 2006).

5.5 Implications for the tectonic evolution of Tanzania

The protoliths of granulite xenoliths from all three localities formed from igneous processes during the Archean. At least two episodes of Archean magmatism are implied by the zircon ages reported here, broadly coinciding with greenstone volcanism at the surface of the craton. However, evidence for post-Archean igneous activity is absent from the zircon and Sr-Nd data. With the exception of modern rift volcanism, which overprinted the Sm-Nd systematics of the garnet-clinopyroxene granulites from Lashaine, no material has been added to the sampled sections of the lower crust since ca. 2660 Ma. This is unusual given the history of deformation and high-grade metamorphism recorded in the upper crust of the Mozambique belt (750-800°C, 1.2-1.3 GPa; Sommer et al., 2003). Lower crustal granulites commonly record basaltic underplating preceding or coeval with high-grade metamorphism, with notable examples including granulites from the Kohistan Arc (Garrido et al., 2006), northern Queensland (Rudnick et al., 1986), and the North China craton (Liu et al., 2004). These syn-metamorphic lower crustal intrusions point to the important role igneous heating plays in regional metamorphism.

If igneous intrusions cannot be invoked as sources of metamorphic heat in the Western Granulites of the East African orogen, an alternative heat source must be available to drive high-grade metamorphism. Two potential sources of orogenic heat are:

(1) Radioactive decay of heat-producing elements K, Th, and U. During orogeny, radioactive heating is more efficient because of double-thickening of K-, Th-, and

U-rich crust and insulation by the mantle.

(2) Incorporation of thin, hot back-arc crust into the orogen (e.g., Hyndman et al., 2005; Johnson and Strachan, 2006).

Neither possibility is appealing as a potential heat source to create the Western Granulites. Radioactive heating, an important heat source in long-lived orogens, seems unlikely to have been important during the Neoproterozoic orogeny because of the low concentrations of heat-producing elements in the crust implied by low surface heat flow in the modern craton (Nyblade et al., 1990). Incorporation of a back-arc crust is likewise improbable based on the pre-collision reconstruction of Tanzania during the Neoproterozoic (Fritz et al., 2005). In this reconstruction, which is based on detailed petrology, zircon U-Pb ages, and T_{DM} ages, ocean crust was subducted under the arc that eventually collided with Tanzania during the East African orogeny. Arc volcanism and back-arc basin formation (represented in the Eastern Granulites exposed in eastern Tanzania) are localized solely in this terrane. The source of metamorphic heat in the Western granulites is therefore enigmatic.

Chapter 6: Conclusions

(1) Mafic granulite xenoliths from the Mozambique belt equilibrated at higher *P-T* conditions than xenoliths from the margin of the Tanzanian craton. High pressures in xenoliths from the metamorphic belt suggest equilibration near the base of orogenically thickened crust, although ca. 600 Ma Pb loss in zircons from the Naibor Soito xenoliths appears inconsistent with this possibility. *P-T* conditions in the Labait xenoliths are consistent with equilibration at the base of crust similar in thickness to that existing today.

(2) U-Pb zircon and Sm-Nd ages indicate that the lower crust beneath both the Tanzanian craton and Mozambique belt stabilized during the Archean. Two igneous events, at ca. 2800 and 2660 Ma, are implied by the analyzed zircon populations. Most zircons formed during the ca. 2660 Ma event, which coincides with a pulse of greenstone volcanism in the upper crust of the Tanzanian craton.

(3) Protoliths of granulite xenoliths from Tanzania were crystallized basaltic melts and plagioclase cumulates. Melt-like xenoliths from Labait and Naibor Soito have negative Nb and Ti anomalies, suggesting that their protoliths formed in a convergent margin. Ca. 2660 Ma zircons from both the two-pyroxene granulites from Labait, the quartz granulites from Naibor Soito, and arc-like volcanic rocks from the Musomba-Mara greenstone belt in the Tanzanian craton (Manya et al., 2006, 2007) all imply the existence of a volcanic arc in Tanzania at this time. By contrast, the biotite granulites from Lashaine have low La/Nb (1.3-1.5) and high Ti/V (~75) more similar to modern intraplate magmas. The biotite granulites and associated garnet-clinopyroxene

granulites from Lashaine may represent a separate episode of magmatism and crustal formation.

(4) No evidence of post-Archean lower crustal growth was found, though ca. 600 Ma concordia lower–intercept ages in zircons from the two Naibor Soito xenoliths suggest Pb loss during the East African orogeny. The absence of basaltic underplating coinciding with high-grade metamorphism is consistent with a lack of Neoproterozoic intrusions in the upper crust of the western Mozambique belt, but leaves open the question of the heat source during East African metamorphism.

Appendix

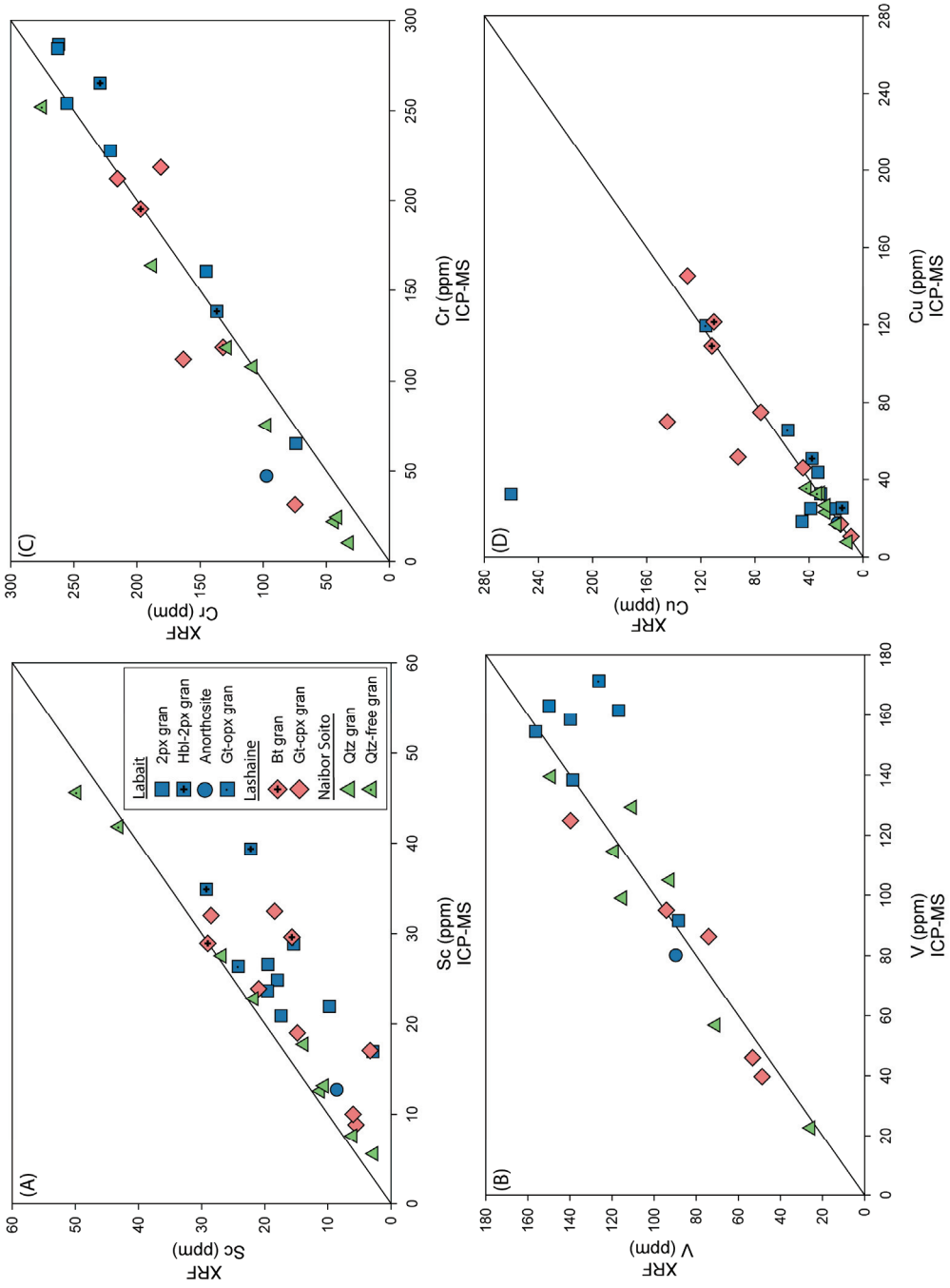

Figure A1. Comparison of trace-element data measured using XRF and ICP-MS, with a 1:1 reference line.

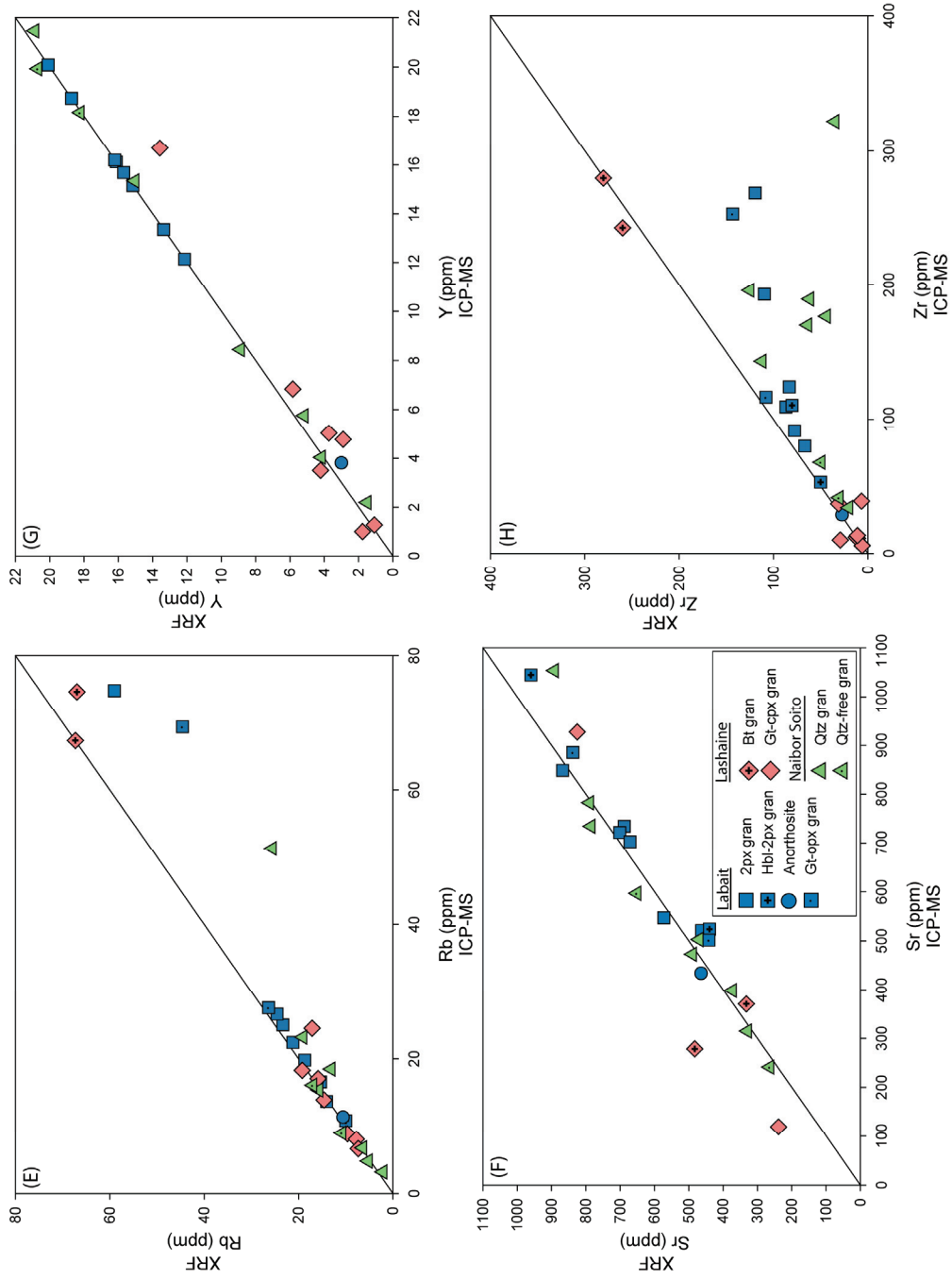

Figure A1 (cont.). Comparison of trace-element data measured using XRF and ICP-MS, with a 1:1 reference line.

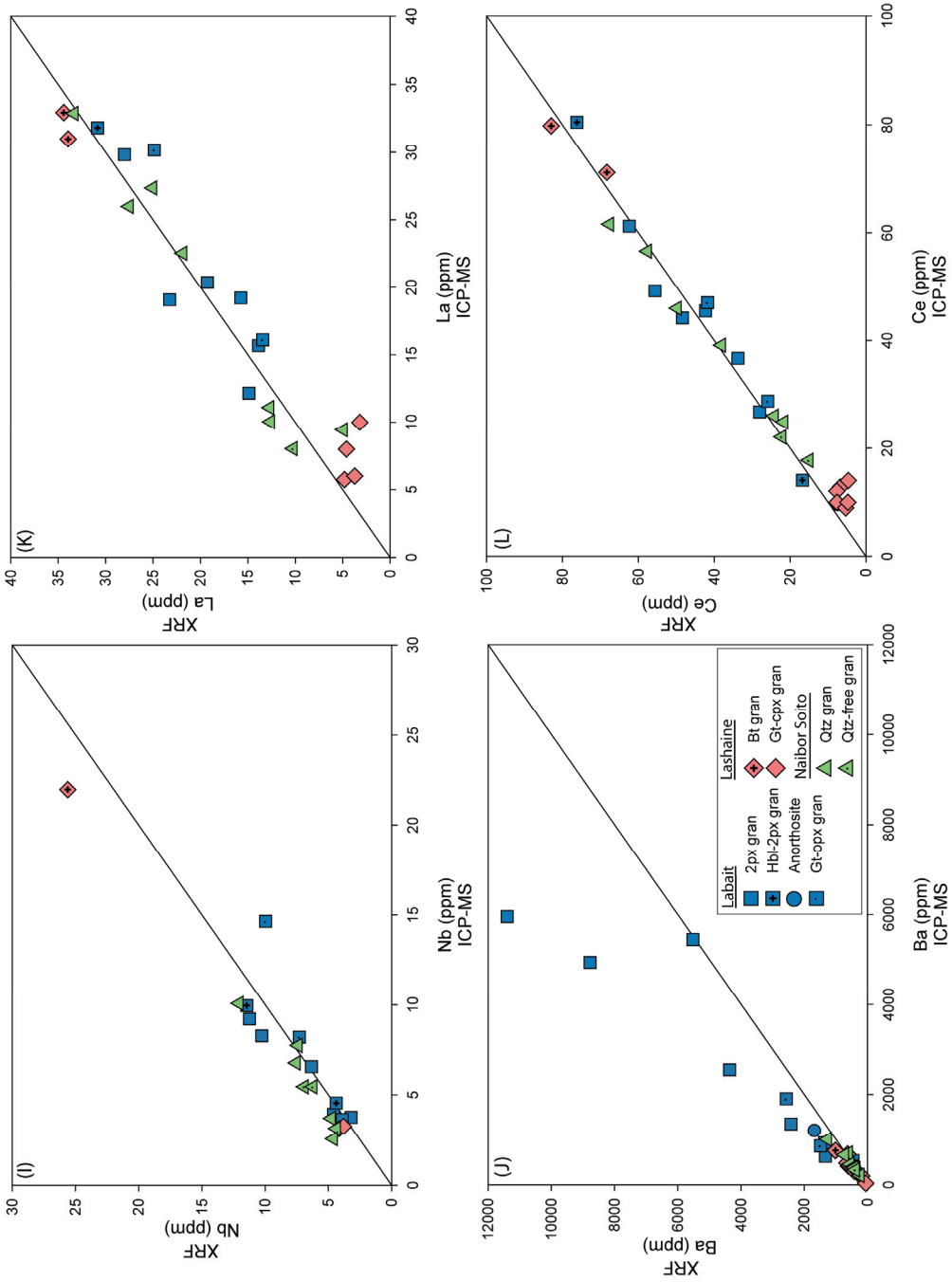

Figure A1 (cont.). Comparison of trace-element data measured using XRF and ICP-MS, with a 1:1 reference line.

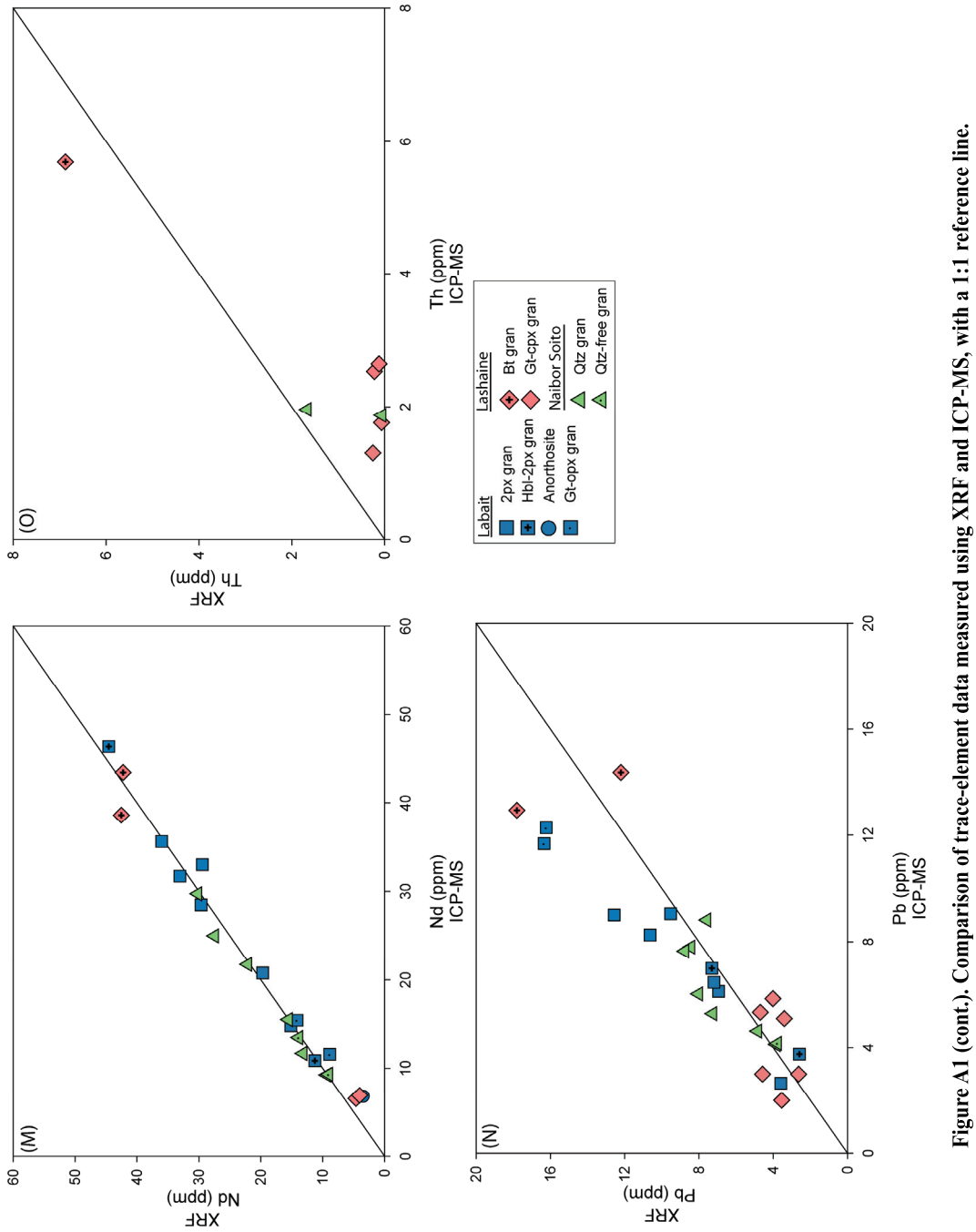

Figure A1 (cont.). Comparison of trace-element data measured using XRF and ICP-MS, with a 1:1 reference line.

References

Arndt N. T. (1991) High Ni in Archean Tholeiites. *Tectonophysics* **187**(4), 411-419.

Ashwal L. D. (1993) *Anorthosites*. Springer-Verlag.

Aulbach S., Rudnick R. L., and McDonough W. F. (2008) Li-Sr-Nd isotope signatures of the plume and cratonic lithospheric mantle beneath the margin of the rifted Tanzanian craton (Labait). *Contributions to Mineralogy and Petrology* **155**(1), 79-92.

Bell K. and Dodson M. H. (1981) The Geochronology of the Tanzanian Shield. *Journal of Geology* **89**(1), 109-128.

Black L. P., Kamo S. L., Allen C. M., Aleinikoff J. N., Davis D. W., Korsch R. J., and Foudoulis C. (2003) TEMORA 1: a new zircon standard for Phanerozoic U-Pb geochronology. *Chemical Geology* **200**(1-2), 155-170.

Brey G. P. and Kohler T. (1990) Geothermobarometry in 4-Phase Lherzolites .2. New Thermobarometers, and Practical Assessment of Existing Thermobarometers. *Journal of Petrology* **31**(6), 1353-1378.

Burton K. W., Schiano P., Birck J. L., Allegre C. J., Rehkamper M., Halliday A. N., and Dawson J. B. (2000) The distribution and behaviour of rhenium and osmium amongst mantle minerals and the age of the lithospheric mantle beneath Tanzania. *Earth and Planetary Science Letters* **183**(1-2), 93-106.

Carson C. J. and Powell R. (1997) Garnet-orthopyroxene geothermometry and geobarometry: error propagation and equilibration effects. *Journal of Metamorphic Geology* **15**(6), 679-686.

Chang Z. S., Vervoort J. D., McClelland W. C., and Knaack C. (2006) U-Pb dating of zircon by LA-ICP-MS. *Geochemistry Geophysics Geosystems* **7**, -.

Chesley J. T., Rudnick R. L., and Lee C. T. (1999) Re-Os systematics of mantle xenoliths from the East African Rift: Age, structure, and history of the Tanzanian craton. *Geochimica Et Cosmochimica Acta* **63**(7-8), 1203-1217.

Cohen R. S., Onions R. K., and Dawson J. B. (1984) Isotope Geochemistry of Xenoliths from East-Africa - Implications for Development of Mantle Reservoirs and Their Interaction. *Earth and Planetary Science Letters* **68**(2), 209-220.

Collins A. S., Reddy S. M., Buchan C., and Mruma A. (2004) Temporal constraints on Palaeoproterozoic eclogite formation and exhumation (Usagaran Orogen, Tanzania). *Earth and Planetary Science Letters* **224**(1-2), 175-192.

Condie K. C. (1994) Greenstones through time. In *Archean Crustal Evolution* (ed. K. C. Condie), pp. 85-120. Elsevier.

Condie K. C. (1999) Mafic crustal xenoliths and the origin of the lower continental crust. *Lithos* **46**(1), 95-101.

Dai B. Z., Jiang S. Y., Jiang Y. H., Zhao K. D., and Liu D. Y. (2008) Geochronology, geochemistry and Hf-Sr-Nd isotopic compositions of Huziyan mafic xenoliths, southern Hunan Province, South China: Petrogenesis and implications for lower crust evolution. *Lithos* **102**(1-2), 65-87.

Dawson J. B. (1977) Sub-cratonic crust and upper mantle models based on xenolith suites in kimberlite and nephelinitic diatremes. *Journal of the Geological Society* **134**(2), 173-184.

Dawson J. B. (1992) Neogene Tectonics and Volcanicity in the North Tanzania Sector of the Gregory Rift-Valley - Contrasts with the Kenya Sector. *Tectonophysics* **204**(1-2), 81-92.

Dawson J. B. (1999) Metasomatism and melting in spinel peridotite xenoliths from Labait, Tanzania. In *Proceedings Volume of 7th International Kimberlite Conference, 1.* (ed. J. J. Gurney, J. L. Gurney, M. D. Pascoe, and S. H. Richardson), pp. 164-173. Red Roof Design.

Dawson J. B. (2002) Metasomatism and partial melting in upper-mantle peridotite xenoliths from the Lashaine volcano, northern Tanzania. *Journal of Petrology* **43**(9), 1749-1777.

Dawson J. B., James D., Paslick C., and Halliday A. (1997) Ultrabasic potassic low-volume magmatism and continental rifting in North central Tanzania: association with enhanced heat flow. In *Proceedings of the Sixth International Kimberlite Conference - Russian Geology and Geophysics, Special Paper*, Vol. 38 (ed. N. L. Dobretsov), pp. 69-81. Alberton Press.

Dawson J. B., Powell D. G., and Reid A. M. (1970) Ultrabasic Xenoliths and Lava from Lashaine-Volcano, Northern Tanzania. *Journal of Petrology* **11**(3), 519-&.

DePaolo D. J. (1981) Neodymium Isotopes in the Colorado Front Range and Crust-Mantle Evolution in the Proterozoic. *Nature* **291**(5812), 193-196.

Dessai A. G., Markwick A., Vaselli O., and Downes H. (2004) Granulite and pyroxenite xenoliths from the Deccan Trap: insight into the nature and composition of the lower lithosphere beneath cratonic India. *Lithos* **78**(3), 263-290.

Downes H., Markwick A. J. W., Kempton P. D., and Thirlwall M. F. (2001) The lower crust beneath cratonic north-east Europe: isotopic constraints from garnet granulite xenoliths. *Terra Nova* **13**(6), 395-400.

Droop G. T. R. (1987) A General Equation for Estimating Fe-3+ Concentrations in Ferromagnesian Silicates and Oxides from Microprobe Analyses, Using Stoichiometric Criteria. *Mineralogical Magazine* **51**(361), 431-435.

Eggins S. M., Kinsley L. P. J., and Shelley J. M. G. (1998) Deposition and element fractionation processes during atmospheric pressure laser sampling for analysis by ICP-MS. *Applied Surface Science* **129**, 278-286.

Fritz H., Tenczer V., Hauzenberger C. A., Wallbrecher E., Hoinkes G., Muhongo S., and Mogessie A. (2005) Central Tanzanian tectonic map: A step forward to decipher Proterozoic structural events in the East African Orogen. *Tectonics* **24**(6), -.

Fuhrman M. L. and Lindsley D. H. (1988) Ternary-Feldspar Modeling and Thermometry. *American Mineralogist* **73**(3-4), 201-215.

Garrido C. J., Bodinier J. L., Burg J. P., Zeilinger G., Hussain S. S., Dawood H., Chaudhry M. N., and Gervilla F. (2006) Petrogenesis of mafic garnet granulite in the lower crust of the Kohistan paleo-arc complex (Northern Pakistan): Implications for intra-crustal differentiation of island arcs and generation of continental crust. *Journal of Petrology* **47**(10), 1873-1914.

Gilbert M. C., Helz R. T., Popp R. K., and Spear F. S. (1982) Experimental studies of amphibole stability. *Reviews in Mineralogy* **9b**, 229-353.

Green N. L. and Usdansky S. I. (1986) Ternary-Feldspar Mixing Relations and Thermobarometry. *American Mineralogist* **71**(9-10), 1100-1108.

Guidotti C. V. (1984) Micas in Metamorphic Rocks. *Reviews in Mineralogy* **13**, 357-467.

Hall A. J. (1941) The relation between colour and chemical composition in the biotites. *American Mineralogist* **26**, 29-33.

Holland T. J. B. (1980) Reaction Albite = Jadeite + Quartz Determined Experimentally in the Range 600-1200-Degrees-C. *American Mineralogist* **65**(1-2), 129-134.

Huang Y. M., Vancalsteren P., and Hawkesworth C. J. (1995) The Evolution of the Lithosphere in Southern Africa - a Perspective on the Basic Granulite Xenoliths from Kimberlites in South-Africa. *Geochimica Et Cosmochimica Acta* **59**(23), 4905-4920.

Jiménez-Munt I., Fernàndez M., Vergés J., and Platt J. P. (2008) Lithosphere structure underneath the Tibetan Plateau inferred from elevation, gravity and geoid anomalies. *Earth and Planetary Science Letters* **267**(1-2), 276-289.

Johnson D. M., Hooper P. R., and Conrey R. M. (1999) XRF Analysis of Rocks and Minerals for Major and Trace Elements on a Single Low Dilution Li-tetraborate Fused Bead. *Advances in X-ray Analysis* **41**, 843-867.

Johnson M. R. W. and Strachan R. A. (2006) A discussion of possible heat sources during nappe stacking: the origin of Barrovian metamorphism within the Caledonian thrust sheets of NW Scotland. *Journal of the Geological Society* **163**, 579-582.

Johnson S. P., Cutten H. N. C., Muhongo S., and De Waele B. (2003) Neoarchaean magmatism and metamorphism of the western granulites in the central domain of the Mozambique belt, Tanzania: U-Pb shrimp geochronology and PT estimates. *Tectonophysics* **375**(1-4), 125-145.

Jones A. P., Smith J. V., Dawson J. B., and Hansen E. C. (1983) Metamorphism, Partial Melting, and K-Metasomatism of Garnet-Scapolite-Kyanite Granulite Xenoliths from Lashaine, Tanzania. *Journal of Geology* **91**(2), 143-165.

Julià J., Ammon C. J., and Nyblade A. A. (2005) Evidence for mafic lower crust in Tanzania, East Africa, from joint inversion of receiver functions and Rayleigh wave dispersion velocities. *Geophysical Journal International* **162**(2), 555-569.

Kempton P. D., Downes H., Neymark L. A., Wartho J. A., Zartman R. E., and Sharkov E. V. (2001) Garnet granulite xenoliths from the Northern Baltic Shield - the underplated lower crust of a palaeoproterozoic large igneous province. *Journal of Petrology* **42**(4), 731-763.

Kempton P. D., Downes H., Sharkov E. V., Vetrin V. R., Ionov D. A., Carswell D. A., and Beard A. (1995) Petrology and geochemistry of xenoliths from the Northern Baltic shield: Evidence for partial melting and metasomatism in the lower crust beneath an Archaean terrane. *Lithos* **36**(3-4), 157-184.

Kempton P. D. and Harmon R. S. (1992) Oxygen Isotope Evidence for Large-Scale Hybridization of the Lower Crust during Magmatic Underplating. *Geochimica Et Cosmochimica Acta* **56**(3), 971-986.

Lee C.-T. and Rudnick R. L. (1999) Compositionally stratified cratonic lithosphere: petrology and geochemistry of peridotite xenoliths from the Labait tuff cone, Tanzania. In *The Nixon Volume, Proceedings of the Seventh International Kimberlite Conference* (ed. J. J. Gurney, J. L. Gurney, M. D. Pascoe, and S. H. Richardson), pp. 503-521.

Leeman W. P., Menzies M. A., Matty D. J., and Embree G. F. (1985) Strontium, Neodymium and Lead Isotopic Compositions of Deep Crustal Xenoliths from the Snake River Plain - Evidence for Archean Basement. *Earth and Planetary Science Letters* **75**(4), 354-368.

Ludwig. (1998) *Isoplot/EX, v. 3.00*. Berekeley Geochronological Center.

Maboko M. A. H. (2000) Nd and Sr isotopic investigation of the Archean-Proterozoic boundary in north eastern Tanzania: constraints on the nature of Neoproterozoic tectonism in the Mozambique Belt. *Precambrian Research* **102**(1-2), 87-98.

Maboko M. A. H. and Nakamura E. (2002) Isotopic dating of Neoproterozoic crustal growth in the Usambara Mountains of Northeastern Tanzania: evidence for coeval crust formation in the Mozambique Belt and the Arabian-Nubian Shield. *Precambrian Research* **113**(3-4), 227-242.

Macdonald R., Rogers N. W., Fitton J. G., Black S., and Smith M. (2001) Plume-lithosphere interactions in the generation of the basalts of the Kenya Rift, East Africa. *Journal of Petrology* **42**(5), 877-900.

Manya S., Kobayashi K., Maboko M. A. H., and Nakamura E. (2006) Ion microprobe zircon U-Pb dating of the late Archaean metavolcanics and associated granites of the Musoma-Mara Greenstone Belt, Northeast Tanzania: Implications for the geological evolution of the Tanzania Craton. *Journal of African Earth Sciences* **45**(3), 355-366.

Manya S. and Maboko M. A. H. (2003) Dating basaltic volcanism in the Neoarchaean Sukumaland Greenstone Belt of the Tanzania Craton using the Sm-Nd method: implications for the geological evolution of the Tanzania Craton. *Precambrian Research* **121**(1-2), 35-45.

Manya S., Maboko M. A. H., and Nakamura E. (2007) The geochemistry of high-Mg andesite and associated adakitic rocks in the Musoma-Mara Greenstone Belt, northern Tanzania: Possible evidence for Neoarchaean ridge subduction? *Precambrian Research* **159**(3-4), 241-259.

McDonough W. F. and Sun S. S. (1995) The Composition of the Earth. *Chemical Geology* **120**(3-4), 223-253.

Meert J. G. (2003) A synopsis of events related to the assembly of eastern Gondwana. *Tectonophysics* **362**(1-4), 1-40.

Mezger K. and Krogstad E. J. (1997) Interpretation of discordant U-Pb zircon ages: An evaluation. *Journal of Metamorphic Geology* **15**(1), 127-140.

Möller A., Appel P., Mezger K., and Schenk V. (1995) Evidence for a 2 Ga Subduction Zone - Eclogites in the Usagaran Belt of Tanzania. *Geology* **23**(12), 1067-1070.

Möller A., Mezger K., and Schenk V. (1998) Crustal age domains and the evolution of the continental crust in the Mozambique Belt of Tanzania: Combined Sm-Nd, Rb-Sr, and Pb-Pb isotopic evidence. *Journal of Petrology* **39**(4), 749-783.

Morimoto N. (1988) Nomenclature of Pyroxenes. *Mineralogy and Petrology* **39**(1), 55-76.

Mottana A. (1986) Crystal-Chemical Evaluation of Garnet and Omphacite Microprobe Analyses - Its Bearing on the Classification of Eclogites. *Lithos* **19**(3-4), 171-186.

Moyen J. F. and Stevens G. (2006) Experimental constraints on TTG petrogenesis: Implications for Archean geodynamics. In *Archean Geodynamics and Environments*, Vol. 164 (ed. K. Benn, J.-C. Mareschal, and K. C. Condie), pp. 149-175. American Geophysocal Union.

Muhongo S., Kroner A., and Nemchin A. A. (2001) Single zircon evaporation and SHRIMP ages for granulite-facies rocks in the Mozambique belt of Tanzania. *Journal of Geology* **109**(2), 171-189.

Neal C. R., Mahoney J. J., Kroenke L. W., Duncan R. A., and Petterson M. G. (1997) The Ontong Java Plateau. In *Large Igneous Provinces: Continental, Oceanic, and Planetary Flood Volcanism*, Vol. 100 (ed. J. J. Mahoney and M. F. Coffin), pp. 183-216. AGU.

Nyblade A. A. (1997) Heat flow across the East African Plateau. *Geophysical Research Letters* **24**(16), 2083-2086.

Nyblade A. A. (2002) Crust and upper mantle structure in East Africa: Implications for the origin of Cenozoic rifting and volcanism and the formation of magmatic rifted margins. In *Volcanic Rifted Margins - Geological Society of America, Special Paper*, Vol. 362 (ed. M. A. Menzies, S. L. Klemperer, C. J. Ebinger, and J. Baker), pp. 15-26. Geological Society of America.

Nyblade A. A. and Brazier R. A. (2002) Precambrian lithospheric controls on the development of the East African rift system. *Geology* **30**(8), 755-758.

Nyblade A. A., Pollack H. N., Jones D. L., Podmore F., and Mushayandebvu M. (1990) Terrestrial Heat-Flow in East and Southern Africa. *Journal of Geophysical Research-Solid Earth and Planets* **95**(B11), 17371-17384.

Padovani E. R. (1977) Granulite facies xenoliths from Kilbourne Hole maar, New Mexico, and their bearing on deep crustal evolution, University of Texas at Dallas.

Padovani E. R. and Carter J. L. (1977) Non-equilibrium partial fusion due to decompression and thermal effects in crustal xenoliths. In *Magma Genesis* (ed. H. B. J. Dick), pp. 43-57.

Paslick C., Halliday A., James D., and Dawson J. B. (1995) Enrichment of the Continental Lithosphere by OIB Melts - Isotopic Evidence from the Volcanic Province of Northern Tanzania. *Earth and Planetary Science Letters* **130**(1-4), 109-126.

Powell R. and Holland T. J. B. (2008) On thermobarometry. *Journal of Metamorphic Geology* **26**(2), 155-179.

Premo W. R. (1991) Isotopic ages and characteristics of the early Proterozoic Green Mountain magmatic arc, SE Wyoming-N. Colorado (abstract). *Geological Society of America - Abstracts with Programs* **20**, A73.

Rapp R. P., Shimizu N., and Norman M. D. (2003) Growth of early continental crust by partial melting of eclogite. *Nature* **425**(6958), 605-609.

Ravna E. K. (2000) Distribution of Fe2+ and Mg between coexisting garnet and hornblende in synthetic and natural systems: an empirical calibration of the garnet-hornblende Fe-Mg geothermometer. *Lithos* **53**(3-4), 265-277.

Ravna E. K. (2000) The garnet-clinopyroxene Fe2+-Mg geothermometer: an updated calibration. *Journal of Metamorphic Geology* **18**(2), 211-219.

Ritsema J., Nyblade A. A., Owens T. J., Langston C. A., and VanDecar J. C. (1998) Upper mantle seismic velocity structure beneath Tanzania, east Africa: Implications for the stability of cratonic lithosphere. *Journal of Geophysical Research-Solid Earth* **103**(B9), 21201-21213.

Rogers N. W. (1977) Granulite Xenoliths from Lesotho Kimberlites and Lower Continental Crust. *Nature* **270**(5639), 681-684.

Rogers N. W. and Hawkesworth C. J. (1982) Proterozoic Age and Cumulate Origin for Granulite Xenoliths, Lesotho. *Nature* **299**(5882), 409-413.

Rogers N., Macdonald R., Fitton J. G., George R., Smith M., and Barreiro B. (2000) Two mantle plumes beneath the east African rift system: Sr, Nd and Pb isotope evidence from Kenya Rift basalts. *Earth and Planetary Science Letters* **176**(3-4), 387-400.

Rudnick R. L. (1992) Xenoliths - samples of the lower continental crust. In *Continental Lower Crust* (ed. D. Fountain, R. Arculus, and R. W. Kay), pp. 269-316. Elsevier.

Rudnick R. L. and Gao S. (2003) The Composition of the Continental Crust. In *In the Crust*, Vol. 3 (ed. R. L. Rudnick), pp. 1-64. Elsevier-Pergamon.

Rudnick R. L., McDonough W. F., and O'Connell R. J. (1998) Thermal structure, thickness and composition of continental lithosphere. *Chemical Geology* **145**(3-4), 395-411.

Rudnick R. L., McDonough W. F., and Orpin A. (1994) Northern Tanzanian peridotite xenoliths: a comparison with Kaapvaal peridoties and inferences on metasomatic interactions. In *Kimberlites, Related Rocks and Mantle Xenoliths - Proceedings of the Fifth International Kimberlite Conference* Vol. 1 (ed. H. O. A. Meyer and O. Leonardos), pp. 336-353. C.P.R.M.

Rudnick R. L., Mclennan S. M., and Taylor S. R. (1985) Large Ion Lithophile Elements in Rocks from High-Pressure Granulite Facies Terrains. *Geochimica Et Cosmochimica Acta* **49**(7), 1645-1655.

Rudnick R. L. and Taylor S. R. (1987) The Composition and Petrogenesis of the Lower Crust - a Xenolith Study. *Journal of Geophysical Research-Solid Earth and Planets* **92**(B13), 13981-14005.

Schluter T. (1997) *Geology of East Africa*. Borntraeger.

Schmitz M. D. and Bowring S. A. (2003) Ultrahigh-temperature metamorphism in the lower crust during Neoarchean Ventersdorp rifting and magmatism, Kaapvaal Craton, southern Africa. *Geological Society of America Bulletin* **115**(5), 533-548.

Shervais J. W. (1982) Ti-V Plots and the Petrogenesis of Modern and Ophiolitic Lavas. *Earth and Planetary Science Letters* **59**(1), 101-118.

Sommer H., Kroner A., Hauzenberger C., Muhongo S., and Wingate M. T. D. (2003) Metamorphic petrology and zircon geochronology of high-grade rocks from the central Mozambique Belt of Tanzania: crustal recycling of Archean and Palaeoproterozoic material during the Pan-African orogeny. *Journal of Metamorphic Geology* **21**(9), 915-934.

Sommer H., Kroner A., Muhongo S., and Hauzenberger C. (2005) SHRIMP zircon ages for post-Usagaran granitoid and rhyolitic rocks from the Palaeoproterozoic terrain of southwestern Tanzania. *South African Journal of Geology* **108**(2), 247-256.

Stern R. J. (1994) Arc Assembly and Continental Collision in the Neoproterozoic East-African Orogen - Implications for the Consolidation of Gondwanaland. *Annual Review of Earth and Planetary Sciences* **22**, 319-351.

Stipska P. and Powell R. (2005) Does ternary feldspar constrain the metamorphic conditions of high-grade meta-igneous rocks? Evidence from orthopyroxene granulites, Bohemian Massif. *Journal of Metamorphic Geology* **23**(8), 627-647.

Tsujimori T., Su B. X., and Nakamura E. (2008) High-pressure granulite xenoliths from northern Tanzania (abstract). In *MISASAIII - 3rd COE International Symposium*.

Weeraratne D. S., Forsyth D. W., Fischer K. M., and Nyblade A. A. (2003) Evidence for an upper mantle plume beneath the Tanzanian craton from Rayleigh wave tomography. *Journal of Geophysical Research-Solid Earth* **108**(B9), -.

Wendlandt E., DePaolo D. J., and Baldridge W. S. (1993) Nd and Sr Isotope Chronostratigraphy of Colorado Plateau Lithosphere - Implications for Magmatic and Tectonic Underplating of the Continental-Crust. *Earth and Planetary Science Letters* **116**(1-4), 23-43.

Wiedenbeck M., Alle P., Corfu F., Griffin W. L., Meier M., Oberli F., Vonquadt A., Roddick J. C., and Speigel W. (1995) 3 Natural Zircon Standards for U-Th-Pb, Lu-Hf, Trace-Element and Ree Analyses. *Geostandards Newsletter* **19**(1), 1-23.

Zheng J. P., Sun M., Lu F. X., and Pearson N. (2003) Mesozoic lower crustal xenoliths and their significance in lithospheric evolution beneath the Sino-Korean Craton. *Tectonophysics* **361**(1-2), 37-60.